Nanoscale Advances

Accepted Manuscript

This article can be cited before page numbers have been issued, to do this please use: K. Q. Nguyen, H. T. Ngo, V. V. Pham and H. H. Tran Hong, *Nanoscale Adv.*, 2026, DOI: 10.1039/D6NA00155F.

ROYAL SOCIETY OF CHEMISTRY

rsc.li/nanoscale-advances

View Article Online
DOI: 10.1039/D6NA00155F

Recent Advances in Nanoalloys for Selective Electrochemical CO_2 Reduction

Khanh Quang Nguyen[1,2], Hong-Huy Tran[1,2], Huan Tan Ngo[1,2], Viet Van Pham[1,2,*]

[1] Advanced Materials and Applications Research Group, HUTECH University, Ho Chi Minh City, 70000, Vietnam

[2]CIRTech Institute, HUTECH University, Ho Chi Minh City, 70000, Vietnam

*Email: pv.viet@hutech.edu.vn (Viet Van Pham)

Abstract

The electrochemical carbon dioxide reduction reaction (CO_2RR) represents a compelling strategy to close the anthropogenic carbon cycle by converting CO_2 into fuels and chemicals using renewable electricity. Despite significant advances, the performance of CO_2RR catalysts remains fundamentally constrained by linear scaling relationships in monometallic systems, which couple the adsorption energetics of key intermediates. This intrinsic limitation restricts independent optimization of reaction steps, leading to poor selectivity, high overpotentials, and persistent competition from the hydrogen evolution reaction (HER). Nanoalloy catalysts have emerged as a powerful platform to overcome these constraints by introducing atomic-scale heterogeneity that is inaccessible to single-metal surfaces. Through controlled integration of multiple elements, nanoalloys enable decoupling of adsorption energetics, generation of distinct active sites, and spatial separation of reaction functions, thereby allowing selective stabilization of intermediates and access to reaction pathways that are thermodynamically or kinetically disfavored on monometallic catalysts. In this review, we move beyond conventional composition-based classifications and present a product-centered framework that directly connects nanoalloy design principles with CO_2RR reaction pathways and target products. We highlight three central synergistic mechanisms that govern nanoalloy behavior: electronic effects arising from d-band center modulation, strain effects induced by lattice mismatch, and ensemble effects enabled by tandem catalysis. We discuss how rational control of these mechanisms, together with microenvironment engineering, provides leverage over local reaction kinetics and selectivity, spanning syngas production, C_1 oxygenate formation, and C–C coupling toward C_{2+} products. Finally, we outline remaining challenges and emerging opportunities in nanoalloy catalyst design, emphasizing strategies to bridge atomic-level mechanistic insight with durable, scalable systems for industrial CO_2 electrolysis.

Keywords

Electrochemical CO_2 reduction; CO_2RR; nanoalloys; product selectivity; linear scaling relationships (LSRs); synergistic effects; tandem catalysis; d-band center engineering.

1. Introduction

View Article Online
DOI: 10.1039/D6NA00155F

Climate change driven by greenhouse gas emissions, particularly CO_2, has become one of today's most urgent global challenges. The escalating frequency of extreme weather events, rising sea level, and widespread ecological disruptions highlight the need for decisive, coordinated international actions to reduce CO_2 emissions. The 2015 Paris Agreement set the goal of limiting global temperature rise to well below 2.0 °C, with efforts to cap warming at 1.5 °C, and called on nations to achieve net-zero emissions by the mid-21st century.[1,2] Most recently, COP30 in Brazil (2025) reinforced this mandate by launching the "Belém Mission to 1.5 °C" and committing to mobilize $1.3 trillion annually by 2035 to accelerate the implementation of low-carbon technologies.[3,4] To realize these ambitious commitments, major economies have solidified "Net Zero 2050" targets, highlighting the urgent demand for clean energy solutions and effective CO_2 mitigation technologies.[5,6]

Within this context, the approaches based on CO_2 reduction reactions have emerged as a highly promising strategy. However, the conversion of CO_2 is fundamentally challenging due to the inherent thermodynamic stability of the molecule, which possesses a linear geometry and a high C=O bond dissociation energy.[7] Traditional CO_2 conversion technologies, such as thermocatalytic hydrogenation, high-temperature reforming, and photochemical reduction, typically require harsh operating conditions (elevated temperatures and pressures or intensive light sources), resulting in high energy consumption and poor overall carbon efficiency.[8] In particular, photochemical CO_2 conversion often suffers from intrinsically low conversion efficiency, which severely limits its practicality even under strong illumination.[9] Moreover, the economic viability of these thermocatalytic process is constrained by two fundamental barriers[10], the high cost of green hydrogen feedstock-currently $6/kg - $8/kg compared to the U.S. DOE's 'Hydrogen Shot' target of $1/kg[11] and the substantial thermodynamic energy input required to drive the reaction, which often challenges the NETL energy efficiency benchmark of 100 kJ/mol CO_2[12].

These constraints hinder the potential large-scale deployment, making the electrochemical CO_2 reduction reaction (CO_2RR) an appealing alternative due to its ability to operate under ambient conditions and couple directly with renewable energy sources to convert CO_2 into value-added fuels and chemicals.[13–15] The product spectrum spans from C_1 compounds such as carbon monoxide (CO)[16–18], formic acid (HCOOH)[19–21], methane (CH_4)[22–24], to C_2 products such as ethylene (C_2H_4)[25–27], ethanol (C_2H_5OH)[27–29], and even C_{3+} products like n-propanol (C_3H_7OH)[30–32]. However, selectivity remains the central challenge in CO_2RR. The reaction involves multiple competing pathways that share similar intermediates, often resulting in complex product mixtures and significant competition from the hydrogen evolution reaction (HER).[33,34] While activity and stability are also important, achieving high selectivity is the most critical bottleneck that limits practical CO_2 electrolysis.

To address these challenges, catalyst design plays a pivotal role. Over the past decades, monometallic catalysts have been extensively investigated; however, their performance is fundamentally constrained by intrinsic barriers, specifically: (1) linear scaling relationships (LSRs) that link the adsorption energies of key intermediates and (2) the consequent inability to selectively stabilize desired intermediates while suppressing competing reactions.[35,36] To overcome these specific limitations, nanoalloys have been proposed as an enabling approach. By strategically combining different elements at atomic and nanoscale levels, alloy catalysts can simultaneously exploit the synergy of the electronic, strain, and ensemble effects to modulate intermediate adsorption energies and create new active sites.[37–40] Furthermore, advanced nanostructural designs, such as core-shell,

Janus, and heterostructures, enable precise spatial control over active site distribution, thereby strongly directing product selectivity.[41–45] Owing to these advantages, nanoalloys provide a versatile platform for tuning intermediate adsorption and directing CO_2RR pathways. However, despite rapid progress over the past decade, several critical challenges remain. Existing studies often investigate individual alloy systems or isolated synergistic effects; thus, a holistic perspective on how electronic, strain, and ensemble effects collectively govern product selectivity remains fragmented.

Moreover, recent perspectives have further crystallized the critical requirements for next-generation catalysts. Moon et al. recently highlighted that for industrial-scale deployment, decoupling catalyst synthesis from electrode fabrication, specifically via the deposition of pre-synthesized nanoparticles, is superior to direct growth methods.[46] This insight places a premium on the precise engineering of robust nanoalloy building blocks that can be scaled up as catalyst inks. Concurrently, Kim et al. emphasized that accessing high-value C_{3+} products requires overcoming significant kinetic barriers involving multi-electron transfers, necessitating not just system-level cascade designs but intrinsic surface sites capable of stabilizing complex intermediates.[47]

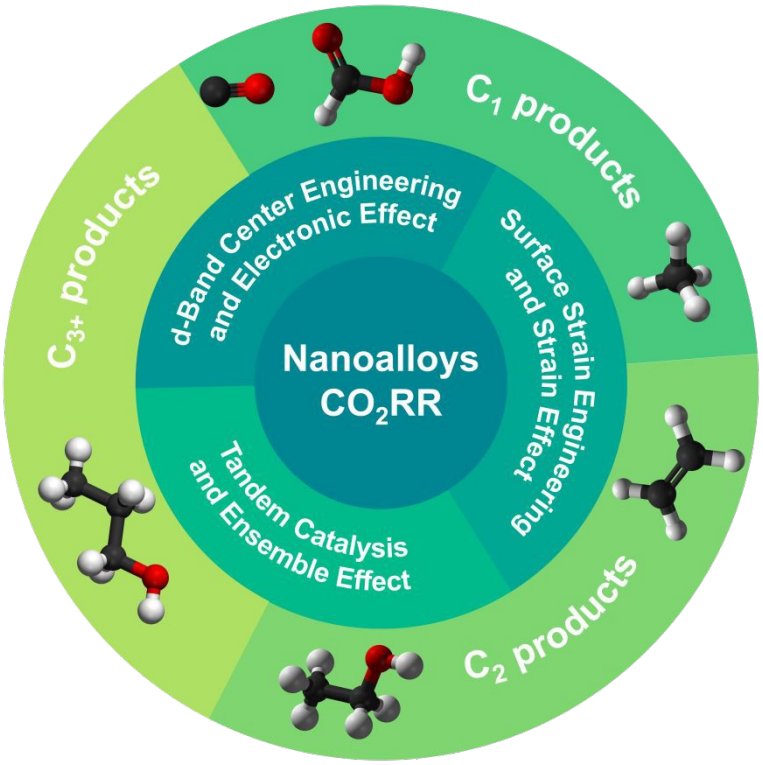

Figure 1. Schematic representation of how nanoalloy synergistic effects govern product selectivity across CO_2RR pathways.

In response to these evolving demands for precise, product-specific active site engineering, this review establishes a comprehensive, product-centered classification of nanoalloy catalysts for CO_2 electroreduction. Rather than solely surveying individual materials or synthesis methods, we organize nanoalloys according to their dominant target products, providing direct comparison of structure-performance relationships across different reaction pathways (Figure 1). We begin by discussing the fundamental limitations of monometallic catalysts under LSRs, followed by an in-depth examination of the key synergistic effects in nanoalloys, including electronic effects, strain engineering, ensemble

View Article Online
DOI: 10.1039/D6NA00155F

effects, tandem catalysis, and strategies for suppressing HER, all of which play crucial roles in governing product selectivity. Building on these principles, the main sections analyze representative alloy systems for each major CO_2RR product, highlighting mechanistic insights, structure-property trends, and design rules. Finally, we outline remaining challenges, knowledge gaps, and future opportunities for rational nanoalloy design to advance next-generation CO_2 electrolysis technologies. Ultimately, by classifying nanoalloys based on target products rather than elemental composition, this review provides a practical roadmap for decoding selectivity. This approach enables researchers to directly compare diverse structural strategies for specific pathways, facilitating the rational design of catalysts tailored for desired CO_2 reduction outcomes.

2. Fundamentals of CO_2RR

CO_2RR-based processes enable the conversion of CO_2 into value-added chemicals through the use of electrical energy, particularly when powered by renewable energy sources.[14,15] Beyond directly reducing CO_2 emissions, this technology provides a pathway for energy storage in the form of chemical bonds within high-value fuels, thereby expanding the potential for sustainable fuel and chemical production and contributing to the global goal of carbon neutrality.[48] The key technological advantage of CO_2RR lies in its feasibility under ambient temperature and atmospheric pressure, in sharp contrast to conventional CO_2 conversion technologies that typically require elevated temperatures and substantial energy input.[49,50]

Thermodynamic Characteristics. CO_2 is an exceptionally stable molecule, with carbon existing at its highest oxidation state. The C=O double bond in CO_2 has a very high bonding energy, approximately 750 kJ/mol.[7] This implies that the reduction of CO_2 is an endothermic reaction, requiring a significant amount of energy input to break these strong bonds and form new products. In electrochemistry, this energy is supplied in the form of an electrode potential. As shown in Table 1, the standard reduction potentials for various CO_2RR pathways in aqueous solution at pH 7 are highly negative; for example, the reduction of CO_2 to CO is −0.53 V versus the standard hydrogen electrode (SHE), while reduction to CH_4 is −0.24 V vs. SHE.[51] However, for the reaction to proceed at an appreciable rate, a much more negative applied potential than the standard reduction potential is required. The difference between the operational potential and the standard reduction potential is referred to as the overpotential. High overpotentials represent one of the major challenges of CO_2RR, as they lower the overall energy efficiency of the process.

Table 1. Electrochemical CO_2 reduction reactions and their corresponding electron/proton transfer numbers.

Reaction	Electron/proton transfers	E° (V vs. SHE, pH 7)
$CO_2 + 2H^+ + 2e^- \rightarrow HCOOH$	2/2	$E^0 = -0.610\ V$
$CO_2 + 2H^+ + 2e^- \rightarrow CO + H_2O$	2/2	$E^0 = -0.530\ V$
$2CO_2 + 2H^+ + 2e^- \rightarrow H_2C_2O_4$	2/2	$E^0 = -0.913\ V$
$CO_2 + 4H^+ + 4e^- \rightarrow HCHO + H_2O$	4/4	$E^0 = -0.480\ V$

View Article Online
DOI: 10.1039/D6NA00155F

$CO_2 + 6H^+ + 6e^- \rightarrow CH_3OH + H_2O$	6/6	$E^0 = -0.380\,V$
$CO_2 + 8H^+ + 8e^- \rightarrow CH_4 + 2H_2O$	8/8	$E^0 = -0.240\,V$
$2CO_2 + 12H^+ + 12e^- \rightarrow C_2H_4 + 4H_2O$	12/12	$E^0 = -0.349\,V$
$2CO_2 + 12H^+ + 12e^- \rightarrow C_2H_5OH + 3H_2O$	12/12	$E^0 = -0.329\,V$
$2CO_2 + 14H^+ + 14e^- \rightarrow C_2H_6 + 4H_2O$	14/14	$E^0 = -0.270\,V$
$3CO_2 + 18H^+ + 18e^- \rightarrow C_3H_7OH + 5H_2O$	18/18	$E^0 = -0.310\,V$
$2H^+ + 2e^- \rightarrow H_2$	2	$E^0 = -0.420\,V$

Reaction Mechanism and Kinetic Challenges. CO_2RR is a complex electrochemical process occurring at the triple-phase interface between the catalytic electrode (solid), the electrolyte (liquid), and the reactant (gas).[52–54] The reaction proceeds through a series of elementary steps: initially, dissolved CO_2 diffuses to the electrode surface, where it is adsorbed and undergoes electron/proton transfers to form intermediates, before finally desorbing as products. A critical kinetic bottleneck in this sequence is the initial activation of the linear CO_2 molecule to form the bent radical anion $*CO_2^{\bullet-}$, which requires a large reorganization energy and a high overpotential.[49,55] Furthermore, the major kinetic challenge in aqueous media is the competition from the HER.[33,34,56] HER generally exhibits more favorable kinetics on many metallic surfaces; therefore, it directly competes with CO_2RR for electrons and active sites on the catalyst surface. Mechanistically, HER is a simple two-electron transfer process, whereas deep CO_2 reduction to high-value products involves complex pathways requiring up to 12 or even 18 electron/proton transfers (Table 1). Moreover, since protons are much smaller and more agile than CO_2 molecules, this competitive advantage is further amplified. Consequently, an effective catalyst must not only exhibit high activity but also high selectivity-defined by the Faradaic efficiency (FE), representing the fraction of current utilized for a specific product relative to the total input current.[57] Strategies to achieve this typically involve destabilizing the *H intermediate to suppress HER while facilitating the multi-step CO_2 reduction pathway.[56]

Performance Metrics. To enable systematic comparison and reporting, studies commonly employ key performance indicators such as overpotential, current density, FE, stability, and selectivity.[58,59] Comprehensive reporting of these parameters is essential for standardized evaluation and to accelerate progress in the field. A summary of these metrics is provided in Table 2.

Table 2. Key performance metrics in CO_2RR.

Metric	Definition	Formula	Unit	Significance
FE	Ratio of charge used to produce a specific product relative to total charge	FE=(nNF/Qtotal)×100	%	Measures product selectivity

Current density (j)	Rate of electrochemical reaction per unit electrode area	jproduct = jtotal × FEproduct	mA cm^{-2}	Reflects production rate; critical for industrial scaling
Overpotential (η)	Difference between applied potential and equilibrium potential	η = Eapplied − E°′	mV	Indicator of energy efficiency; lower η means lower energy consumption
Selectivity	Ability to preferentially form a desired product	Commonly quantified by FE	-	Reduces product separation cost and enhances economic value
Stability	Duration of stable catalyst operation	Operating time (h) with stable FE and j	h	Critical for practical applications and operational cost

3. Intrinsic Limitations of Monometallic Catalysts and the Strategy of Using Nanoalloys in CO_2RR

3.1. Limitations of Monometallic Catalysts under LSRs

In CO_2RR, metals play a central role, not only serving as the surface for adsorption and activation of CO_2 molecules, but also determining the reaction mechanism and the selectivity of the final products.[60] Each metal exhibits distinct adsorption properties toward reaction intermediates, leading to a preference for the formation of specific products. Based on the main products, monometallic catalysts are generally categorized into four main groups, as summarized in the Table 3.

Table 3. Overview of monometallic catalysts for CO_2RR.

Metal group	Main products	Key intermediates	Advantages
Pb, Hg, In, Sn, Cd, Tl, Bi	HCOOH	*OCHO	High selectivity for formate; weak competition from HER
Au, Ag, Zn, Pd, Ga	CO	*COOH, *CO	High CO selectivity
Ni, Fe, Pt, Ti	H_2	*H	Strong HER activity, unfavorable for CO_2RR
Cu	CO, HCOOH, CH_4, C_2H_4, C_2H_5OH, …	*CO, *CHO, *COH, *OCCO, …	Unique ability to reduce CO_2 to multi-carbon products

View Article Online
DOI: 10.1039/D6NA00155F

One of the simplest and most commercially promising pathways is the production of CO, a key C_1 product. The earliest seminal work on monometallic catalysts was reported by Hori et al.[61], who demonstrated that Au and Ag exhibit exceptionally high selectivity toward CO due to their favorable binding of COOH and weak adsorption of CO. Following this foundation, subsequent studies have systematically improved the performance of monometallic Au and Ag through nanostructuring, support engineering, and crystal-phase control. Representative advances include nanostructured Au catalysts achieving FE_{CO} values of ~70% - 77% in neutral media, conductive-core architectures that enhance electron transport[62,63], and the emergence of 4H-phase Au nanomaterials with FE_{CO} exceeding 90% at −0.7 V vs. reversible hydrogen electrode (RHE)[64]. Similarly, Ag-based systems-especially triangular nanoplates, 3D foams, and ultrathin nanowires-have achieved FE_{CO} values approaching 95% - 99% with reduced overpotentials and industrially relevant current densities.[65–67]

View Article Online
DOI: 10.1039/D6NA00155F

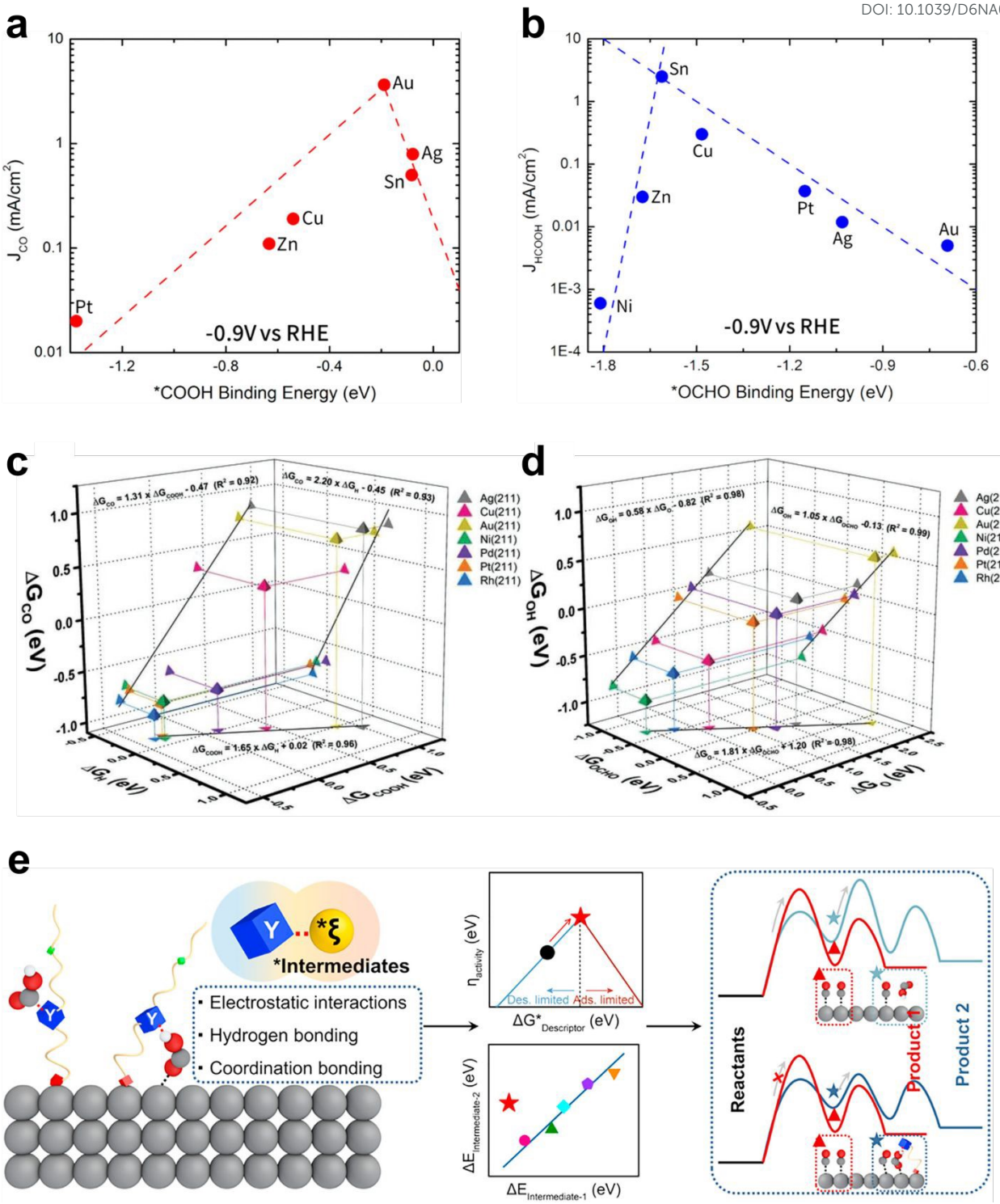

Figure 2. (a, b) Volcano-plot correlations between partial current density and binding energy of *COOH and *OCHO intermediates, reproduced from ref [68] with permission from American Chemical Society, copyright 2017. (c, d) Three-dimensional scaling relations among key pairs of intermediates (*COOH, *CO, *H) and (*OCHO, *OH, *O) on various metal surfaces, showing inherent linear coupling that limits selectivity tuning, reproduced from ref [69] with permission from WILEY-VCH Verlag GmbH & Co. KGaA, Weinheim, copyright 2018. (e) Schematic illustration of material modifications that selectively stabilize intermediates and break the linear scaling limitation of

View Article Online
DOI: 10.1039/D6NA00155F

monometallic catalysts in CO_2RR, reproduced from ref [70] with permission from Elsevier Inc., copyright 2023.

These findings indicate that even with a single metal, the design of unique crystal structures can significantly enhance performance; however, both Au and Ag ultimately remain limited to producing CO and are unable to effectively drive the formation of multi-carbon products. Such observations directly reflect the Sabatier principle: an ideal catalyst must bind reaction intermediates with a moderate strength, not too weak and not too strong.[71] If the binding is too weak, reactants are poorly activated and rapidly desorb; conversely, if the binding is too strong, intermediates are strongly retained on the surface, leading to the poisoning of active sites and hindering subsequent reaction steps.[72] This principle is often illustrated visually by a volcano plot, in which, on the weak-binding branch, activity is limited by the adsorption or activation step, while on the strong-binding branch, it is constrained by product desorption (Figure 2a,b).[68] The most effective catalysts typically reside near the summit of the plot, where an optimal balance is achieved. The challenge for complex reactions such as CO_2RR is that a single metal may lie close to the peak for one product, yet far from the peak for another.[71] In the case of Au and Ag, both possess nearly optimal binding energies for *COOH, placing them close to the volcano peak for CO formation (Figure 2a). However, they fall on the weak-binding branch for *CO, causing this intermediate to desorb readily as CO gas. As a result, these metal surfaces cannot retain *CO long enough to drive C–C coupling toward multi-carbon products. Similarly, for post-transition metals such as Sn (Figure 2b), the stronger affinity for *OCHO intermediates positions Sn near the volcano peak for HCOOH formation, accounting for the high formate selectivity of Sn-based catalysts in CO_2RR. However, from an economic perspective, C_{2+} products possess far greater energy density and market value, making the restriction to CO or formate production a major limitation for practical CO_2 electrolysis applications.[73]

Copper (Cu) is the only metal capable of overcoming this limitation, as it resides at the very summit of the volcano plot for the *CO intermediate.[74] The binding energy between Cu and *CO is sufficiently strong to maintain a substantial surface coverage of *CO, yet not so strong as to hinder subsequent dimerization or hydrogenation steps. This delicate balance endows Cu with a unique ability to catalyze the formation of multi-carbon products.[75] However, Cu faces another critical challenge: poor selectivity. Because of its capacity to stabilize *CO and catalyze multiple reaction pathways simultaneously, the Cu surface typically generates a complex mixture of products. This makes it extremely difficult to selectively obtain a single high-purity product.[76]

Ultimately, all monometallic catalysts are constrained by the intrinsic limitation of the LSRs (Figure 2c,d).[69,77–80] This represents a deeper thermodynamic barrier, explaining why it is fundamentally challenging to simultaneously optimize every step in a complex reaction sequence on a single-metal surface. Fundamentally, LSRs are universal correlations between the adsorption energies of chemically similar reaction intermediates (e.g., *COOH, *CO, and *CHO, all of which bind through the carbon atom) across diverse catalyst surfaces, originating from bond-order conservation principles and the d-band model.[81–83] These relationships are predominantly established through first-principles computational methods, such as density functional theory (DFT)[81,82], and can be further validated experimentally by measuring the heats of adsorption using techniques like single crystal adsorption calorimetry (SCAC)[84]. Because of these strong correlations, if a metal binds *CO strongly, it will also bind *COOH strongly. Consequently, the binding energy of one intermediate cannot be

View Article Online
DOI: 10.1039/D6NA00155F

independently tuned without altering the binding energies of other intermediates in the reaction pathway. The implication of LSRs is a significant reduction in the degrees of freedom available in catalyst design, creating an extended Sabatier barrier that monometallic catalysts cannot overcome. For example, to optimize CH_4 formation, it would ideally be necessary to stabilize the *CHO intermediate relative to *CO. However, due to LSRs, any attempt to strengthen *CHO binding will simultaneously strengthen *CO binding, leaving the energy barrier between them nearly unchanged.[85–87]

3.2. From Limitations to the Strategy of Nanoalloys

The existence of scaling relationships compels researchers to search for materials capable of breaking or deviating from these thermodynamic constraints (Figure 2e). A classic demonstration of this strategy was reported by Lu et al. on Mn–Ni heteronuclear dual-atom catalysts (DACs).[79] In conventional single-metal catalysts, simultaneously achieving strong *COOH binding to lower the activation barrier and weak *CO binding to promote desorption is impossible. In contrast, Mn–Ni DACs exhibit a synergistic "task division": the Ni center, with a reduced valence state due to electron transfer from Mn, preferentially binds to the carbon atom in *COOH and *CO, facilitating intermediate stabilization and CO release. Meanwhile, the Mn center, in a higher valence state, interacts strongly with the oxygen atom in COOH, thereby promoting CO_2 protonation. This cooperative mechanism enables intermediates to shuttle between the two metal centers, breaking the LSRs and achieving a remarkable FE_{CO} of 98.7% at −0.7 V vs. RHE.

Such studies highlight the urgent need to develop new catalytic materials with the ability to tune electronic and geometric structures for more precise control over intermediate interactions. In this context, nanoalloys have emerged as a pivotal strategy. By integrating multiple elements and enabling structural design at the nanoscale, they offer superior flexibility in tailoring electronic properties, providing abundant active sites, and opening reaction pathways that monometallic catalysts remain challenging to achieve.

To fully realize these sophisticated nanoscale designs, selecting an appropriate synthesis strategy is a crucial prerequisite. Currently, various methodologies have been employed to fabricate nanoalloys, each offering distinct advantages, limitations, and applicable scenarios in precisely controlling the composition, morphology, and atomic arrangement of the catalysts, as systematically summarized in 4.

Table 4. Summary of mainstream synthesis methods for nanoalloys.

Synthesis Method	Operating Principle	Advantages	Disadvantages	Applications
Chemical Reduction	Employs reducing agents (e.g., $NaBH_4$, ascorbic acid, hydrazine) to reduce metal	- Facile operation, cost-effective, and easily scalable for mass production. - Allows precise control over	- Often involves toxic chemicals. - Difficult to co-reduce metals with large differences in reduction potentials,	- Colloidal synthesis of well-dispersed alloy nanoparticles.[88–90] - Fabrication of core-shell structures via

	ions into their metallic states.	particle size and elemental composition.	which may lead to phase segregation rather than alloying without proper ligands.	successive reduction.[91]
Magnetron Sputtering	Utilizes plasma (typically Ar) to bombard metal targets, depositing an alloy film onto a substrate.	- Very high product purity. - Precise control over elemental composition. - High uniformity and reproducibility for large-area, self-supporting electrodes.	- Requires expensive vacuum equipment and high energy consumption. - Less morphological diversity and challenging 3D shape control compared to wet-chemical methods.	- Direct deposition of nanoalloy films onto gas diffusion layers (Cu-Sn alloy nanofilm[92]; CuAg electrodes[93]; Cu/Ag and Cu/Al alloys[94]).
Electrochemical Deposition	Simultaneous reduction of metal ions from an electrolyte directly onto the electrode surface driven by an applied potential/current.	- Avoids contamination from chemical reducing agents. - Composition and size can be tuned via current density, applied potential, or pH. - Enhances adhesion between the catalyst layer and the electrode.	- Certain electrolytes may generate byproducts or toxic gases during plating. - Difficult to achieve atomic-level uniformity for complex multicomponent alloys.	- Fabrication of self-supported, porous alloy architectures directly on working electrodes (mesoporous AuCuNi ternary alloy films[95]; porous Cu-Ni alloy[96]; porous Cu-Pd alloy layers[97]; PtCu alloy[98]).
Galvanic Replacement	Uses a metal with a lower reduction potential as a sacrificial template to provide electrons for reducing ions of a more noble metal.	- Extremely powerful technique for fabricating hollow structures to maximize 3D spatial accessibility and surface area.	- Often requires subsequent thermal treatment steps to ensure complete alloying and phase uniformity.	- Fabricating nanoarchitectures (hollow Au-Cu nanorods[99]; Cu-In nanocrystals[100]; AuAg alloy nanoparticles[101]; highly alloyed AuAg aerogel[102]).

Laser Ablation in Liquid (LALT)	A high-energy laser vaporizes a solid metal target and decomposes metal salts in solution, followed by rapid quenching.	- "Green" synthesis with fast reaction times. - Ultra-fast quenching overcomes thermodynamic limits, enabling the alloying of classically immiscible metals.	- Requires expensive, specialized laser equipment. - Challenging to scale up for massive industrial production.	- Fabrication of highly metastable, defect-rich nanoalloys (RuAu SAA[103]; HEAs nanoparticles[104]; AuFe alloy nanoparticles[105]).
Carbothermal Shock (CTS)	An ultrafast process involving instantaneous melting, decomposition, and solidification of precursors (within milliseconds) at extreme temperatures (~2000 K).	- Extremely fast processing time. - Capable of uniformly mixing multiple immiscible elements to form perfect solid solutions.	- Requires extreme peak temperatures and specialized equipment capable of generating massive heating/cooling rates.	- Developing multi-element High-Entropy Alloys (HEAs) uniformly dispersed on carbon supports (PtPdRhRuCe HEAs nanoparticles[106]; FeCoNiPtRu HEAs[107]; RhRuFeCoNiMo HEAs nanoparticles/ WO_3 nanofibers[108]).
Support-Assisted Synthesis	Carbon networks, MOFs, or polymer frameworks act as spatial confinement and stabilizing agents during metal ion reduction.	- Provides spatial confinement that effectively controls particle dispersion and limits agglomeration. - Successfully inhibits the oxidation of highly reactive metals.	- Complex preparation process that is highly dependent on the quality and intrinsic properties of the support materials.	- Ideal for fabricating rare-earth nanoalloys, where rare-earth metals possess extremely negative reduction potentials and are highly prone to oxidation.[109]

Thermal Decomposition	Simultaneous decomposition of organic/inorganic metal precursors at appropriate temperatures without additional reducing agents.	- Produces nanoalloys with high crystallinity at relatively low temperatures.	- Requires precursors with matching decomposition temperatures to ensure homogeneous alloying. - Certain precursors are highly toxic.	- Fabrication of fine-grained, highly crystalline alloy nanoparticles, particularly for noble metal alloys (PdPt alloy nanodendrites[110]).
Sonochemical Synthesis	Utilizes high-intensity ultrasound to induce acoustic cavitation, creating extreme local temperatures and pressures upon bubble collapse.	- Reactions can proceed under normal ambient external conditions. - Facilitates the formation of metastable or amorphous structures.	- Difficult to control cavitation uniformity across large volumes, limiting large-scale mass production.	- Surface modification of catalyst particles to boost activity and the synthesis of bimetallic nanoalloys with narrow size distributions[111].

Ultimately, an optimal synthesis strategy endows nanoalloys with superior catalytic properties, and the foundation of this superiority lies in unique synergistic effects, cooperative interactions between different components or active centers that enhance overall performance beyond what individual components can achieve. These synergistic effects may manifest through: (i) cooperative action, where active centers coordinate via intermediate transfer; (ii) synergistic interaction, in which the coexistence of multiple catalytic sites enables new reaction pathways; and (iii) mutual promotion, where different active centers accelerate charge, proton, or intermediate transfer.[112] These interactions are externally expressed through three principal synergistic effects: the Electronic Effect, the Strain Effect, and the Ensemble Effect. Nanoalloys can overcome the challenges of monometallic catalysts by employing a variety of design strategies:

3.2.1. Electronic Effect and d-Band Center Engineering

The electronic effect arises when the presence of hetero-metal atoms near the active center alters the local electron density. In other words, chemical interactions between dissimilar atoms redistribute the surface electronic structure. This effect is typically described in terms of shifts in the d-band center or modifications of the density of states (DOS) near the Fermi level of the host metal. The origin of this phenomenon lies in unique **metal-metal interactions**, which create **coordination microenvironments** absent on monometallic surfaces. The resulting electronic perturbations and

orbital hybridization between heteroatoms alter the energy of the d-band center while simultaneously restructuring the local geometric and electronic states of the active sites.[113]

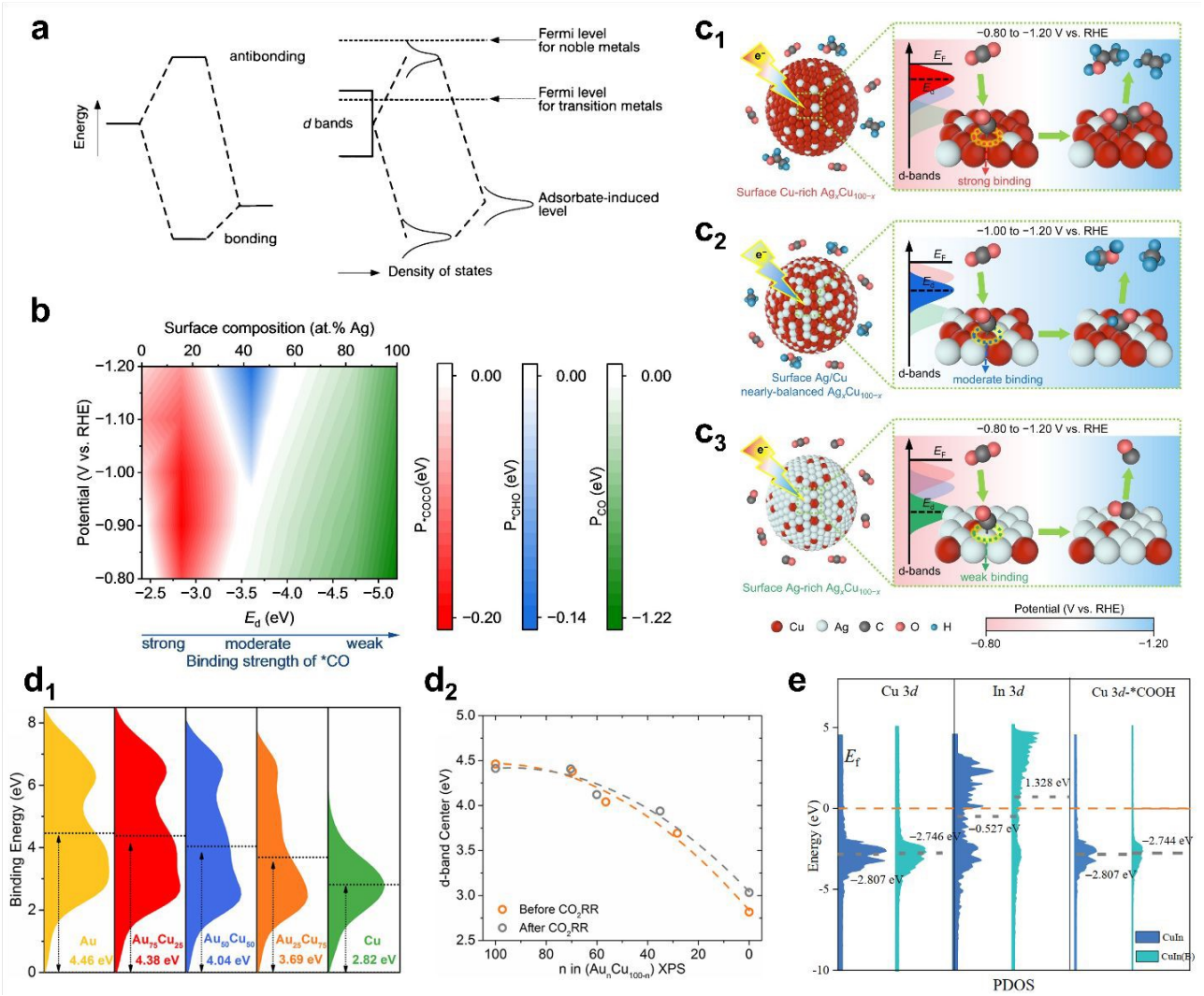

Figure 3. Illustration of d-band center engineering to control product selectivity in CO_2RR. (a) Schematic principle of the d-band center theory, reproduced from ref [114] with permission from Springer Nature Limited, copyright 1995. (b) Product selectivity map as a function of E_d and applied potential, and (c) the corresponding mechanisms on Ag–Cu surface alloys, reproduced from ref [115] with permission from Wiley-VCH GmbH, copyright 2023. (d) Experimental valence band XPS showing the d-band center shift in Au–Cu alloys, reproduced from ref [116] under CC-BY-NC-ND. (e) Calculated PDOS showing the upward d-band center shift in B-doped CuIn alloy, reproduced from ref [117] with permission from Dalian Institute of Chemical Physics, the Chinese Academy of Sciences, copyright 2023.

In CO_2RR, the d-band center acts as a central descriptor governing the adsorption strength of intermediates, thereby dictating both catalytic activity and product selectivity. Figure 3a illustrates the basic principle of this theory: orbitals from an adsorbate interact with the metal's d-band to form bonding and antibonding states. The position of the d-band center (E_d) relative to the Fermi level (E_F) determines the filling of these antibonding states, which in turn dictates the bond strength.[114] Specifically, when the d-band shifts upward toward the Fermi level, the adsorption of intermediates

View Article Online
DOI: 10.1039/D6NA00155F

becomes stronger, favoring deeper hydrogenation steps and the formation of C_{2+} products. Conversely, when the d-band shifts downward, the interaction with *CO weakens, enabling facile CO desorption and enhancing CO selectivity.[118] Both DFT studies and experimental evidence have demonstrated that d-band tuning can be achieved through various strategies, including metal alloying, lattice strain, heterostructure construction, or the incorporation of single-atom catalysts. Among these, nanoalloys offer a versatile platform to finely tune the electronic structure of metals. By systematically varying the atomic composition and coordination environment, the d-band center can be shifted continuously, allowing for the precise optimization of binding energies of key intermediates.[89] Such tuning not only directs desired reaction pathways but also suppresses competing reactions such as HER.

For instance, doping Cu with a more electronegative metal such as Sn withdraws electron density from Cu, shifting its d-band downward and weakening the adsorption of *COOH and *OCHO. Conversely, alloying with a less electronegative element such as In donates electrons to Cu, shifting its d-band upward and enhancing *COOH adsorption.[118] This upward shift effect is also confirmed in Boron-doped CuIn systems, as shown in the calculated projected density of states (PDOS) in Figure 3e, where both Cu 3d and In 3d bands shift closer to the Fermi level.[117] In Au–Cu alloys, increasing Au content shifts the d-band center further from the Fermi level, as clearly demonstrated by the experimental data in Figure 3d, where the d-band center shifts linearly from –2.82 eV (pure Cu) down to –4.46 eV (pure Au).[116] This downward shift weakens adsorption interactions and favors CO production, while the remaining Cu sites still provide sufficient binding to stabilize *COOH.[69,116] Similarly, in Pd–Au systems, the presence of Au lowers the d-band of Pd, thereby reducing *CO binding and promoting efficient CO desorption.[89] In Cu–Ni and Cu–Ag alloys, interactions with oxygenated intermediates are weakened, which enhances selectivity toward liquid carbonyl products while suppressing HER.[119] Furthermore, in Co_xNi_{1-x}/N-CNFs, modulation of the d-band center significantly alters intermediate binding energies, with $Co_{0.75}Ni_{0.25}$/N-CNFs achieving FE as high as 85.0% for CO at moderate overpotentials.[120]

A clear example of how electronic effects govern product selectivity in nanoalloys is demonstrated in the study by Wei et al.[115]. In Ag–Cu surface alloys, adjusting the Ag/Cu ratio tunes the d-band center, directly controlling the *CO binding strength. This relationship allows for systematic control over the final product, as illustrated in the 3D selectivity map in Figure 3b, which maps product FE based on E_d and applied potential. A Cu-rich surface (e.g., $Ag_{16}Cu_{84}$), corresponding to a high E_d and strong *CO binding (Figure 3c_1), facilitates C–C coupling to form *COCO and yields C_2 products with an FE up to ≈60%. At intermediate compositions (e.g., $Ag_{43}Cu_{57}$) with a moderate E_d and moderate *CO binding (Figure 3c_2), C–C coupling is suppressed, but hydrogenation to *CHO is favored, thus shifting selectivity to C_1 products (CH_4 and CH_3OH) with an FE of ≈41%. Finally, at Ag-rich compositions (e.g., $Ag_{83}Cu_{17}$) with a low E_d and weak *CO binding (Figure 3c_3), leading to facile desorption before further reaction, resulting in high selectivity for CO (≈74% FE).

Advanced alloy designs have also demonstrated combined electronic and geometric effects. For example, B-doped CuIn catalysts, as seen in Figure 3e where the Cu 3d E_d shifts from –2.807 eV to –2.746 eV, exhibit optimized electronic structures that provide abundant active sites and improved charge transfer kinetics, enhancing CO_2-to-CO selectivity over a wide potential range.[117] Similarly, Zeng et al. demonstrated that Pd-Ag alloy electrocatalysts could surpass the constraints of LSRs for

efficient CO production.[121] By fine-tuning the alloy composition, optimizing at $Pd_{0.75}Ag_{0.25}$, they modulated the surface electronic structure to weaken the overly strong binding of *CO on Pd sites. This balanced interaction facilitated the desorption of products while maintaining high activity for CO_2 activation, resulting in a superior FE_{CO} of 95.3%. In another approach, a thermally induced "atomic replacement" strategy was utilized to transform PtNi encapsulated in Zn-ZIF-8 into PtZn intermetallics coupled with isolated Ni single atoms.[122] DFT calculations revealed a pronounced synergistic effect between adjacent PtZn and Ni_1 sites. PtZn stabilized the COOH intermediate via Pt–O interactions, thereby significantly lowering the protonation barrier on nearby Ni single-atom sites, while the cooperative PtZn–Ni_1 configuration simultaneously facilitated CO desorption.

3.2.2. Strain Effect and Surface Strain Engineering

The strain effect, more specifically lattice strain, arises from atomic size mismatch or lattice incompatibility between different components of a catalytic material. Strain can be categorized into two main types: **tensile strain**, when the interatomic distance increases, and **compressive strain**, when this distance decreases.[123] Beyond inherent atomic size differences, lattice strain can also be deliberately introduced through advanced nanoscale structural design, which is now recognized as one of the key principles governing the overall performance of catalytic systems. One of the most effective strategies for intentionally inducing strain is the core-shell architecture. A representative study by Sun et al. designed a charge-asymmetry "armor" catalyst (Pd_1Fe SAA@PC), in which a Pd_1Fe single-atom alloy (SAA) core is encapsulated by a phosphorus-doped carbon (P-doped C) shell.[124] Both experimental characterizations and theoretical calculations confirmed that this P-doped carbon layer imposed a tensile lattice strain of approximately +1.2% on the metallic core. DFT results further demonstrated that this optimal strain substantially increased the energy barrier for over-hydrogenation, thereby underscoring the critical role of lattice strain in governing product selectivity. Another approach is to introduce surface vacancies. Guo et al. convincingly demonstrated this principle in nanoporous PtCu alloys.[125] Using electrochemical etching, they selectively removed Cu atoms from the surface, generating a high density of Cu vacancies. Structural analyses revealed that these vacancies induced compressive lattice strain in the neighboring Pt lattice. DFT further revealed that Cu vacancies modified the adsorption properties of Pt sites, strengthening binding to desired intermediates (HO*) while weakening binding to undesired intermediates (O*), thereby enhancing catalytic activity.

View Article Online
DOI: 10.1039/D6NA00155F

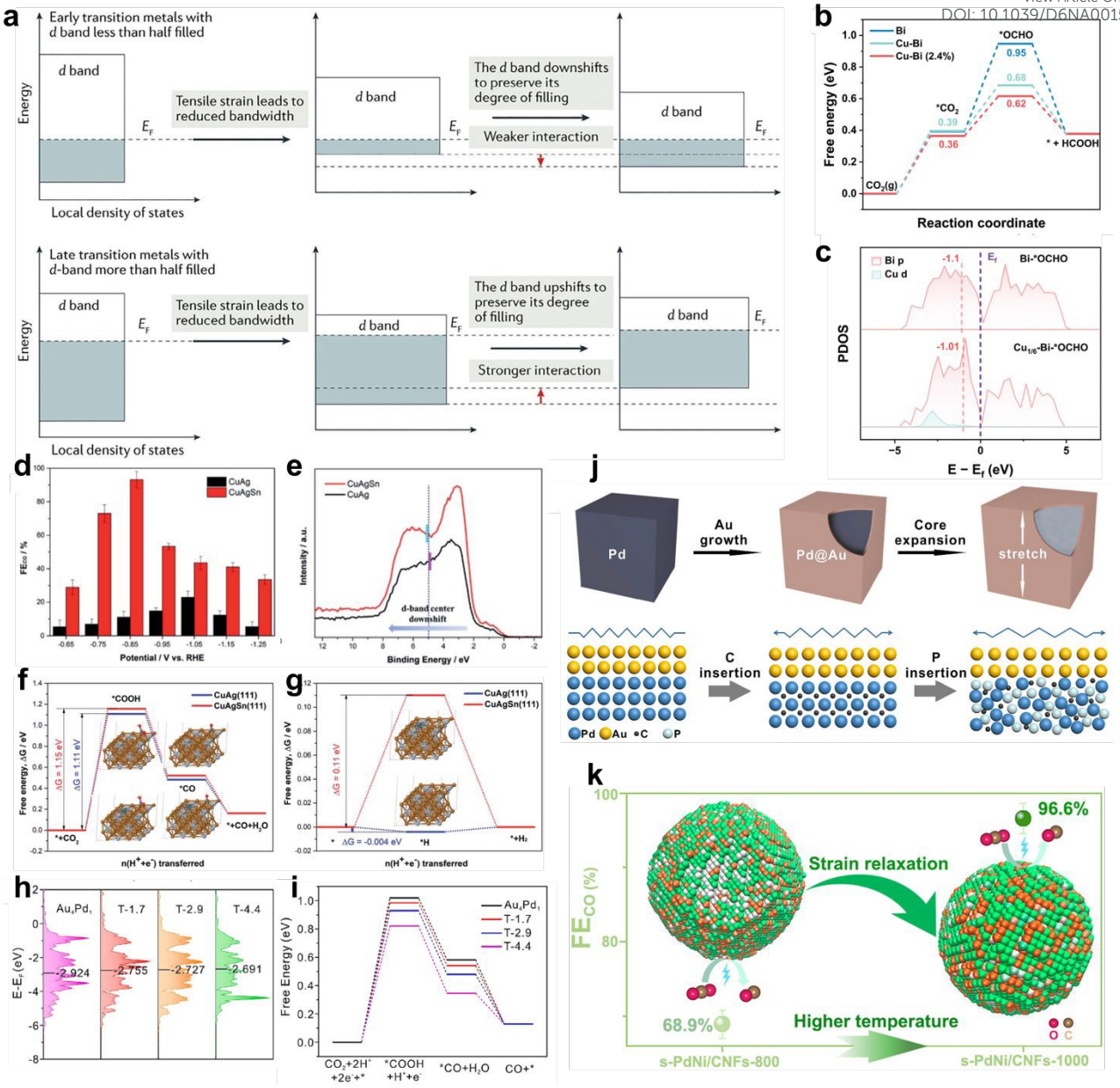

Figure 4. Strain-induced modulation of electronic structure and catalytic selectivity across representative CO_2RR nanoalloys. (a) Schematic illustration of how tensile strain shifts the d-band center of early and late transition metals, reproduced from ref [126] with permission from Macmillan Publishers Limited, copyright 2017. (b-c) Theoretical evidence in Cu-Bi system showing that tensile strain facilitates CO_2 activation and stabilizes OCHO intermediates, reproduced from ref [127] with permission from Wiley-VCH GmbH, copyright 2024. (d-g) Potential-dependent CO selectivity, valence band XPS spectra, and Gibbs free energy profiles for the CuAgSn alloy revealing that lattice distortion and d-band downshift increase *H adsorption energy, suppressing the competing HER and enhancing CO formation, reproduced from ref [128] with permission from Royal Society of Chemistry, copyright 2022. (h-j) AuPd alloy: controlled phosphorization expands the Pd core to generate tunable tensile strain, enhancing FE_{CO} through d-band upshift and lowered COOH formation barrier, reproduced from ref [129] with permission from Elsevier B.V., copyright 2025. (k) Illustration of strain-relaxation-driven optimization, where moderate lattice relaxation balances COOH formation and CO

desorption, reproduced from ref [130] with permission from American Chemical Society, copyright 2022.

These structural distortions directly influence the electronic structure of active sites, primarily through modulation of the d-band center. For late transition metals (d-band more than half filled, such as Cu, Ag, Au), tensile strain reduces orbital overlap, narrows the d-band, and shifts its center upward toward the Fermi level, strengthening interactions with intermediates. In contrast, compressive strain shifts the d-band downward, weakening adsorption.[131] For early transition metals (d-band less than half filled), the trend is reversed.[123] This fundamental mechanism is illustrated in Figure 4a, which shows that tensile strain causes an upward d-band shift for late transition metals (strengthening adsorption) but a downward shift for early transition metals (weakening adsorption).[126] By deliberately tuning the type and magnitude of strain in nanoalloys, the adsorption energies of key intermediates can be modulated, enabling simultaneous control over both activity and selectivity in CO_2RR.[132–134] For example, on bismuth-based catalysts, tensile strain on pristine Bi sites strengthened *OHCO adsorption and lowered the reaction barrier, achieving FE above 90% for HCOOH.[132] Similarly, Bi@Sn core–shell structures with compressive strain were shown to promote CO_2-to-formic acid conversion.[135] In copper-based systems, strain plays a crucial role in regulating CO_2RR[133], while rare-earth dopants can induce tensile strain in CuO_x catalysts, enhancing efficiency toward C_{2+} products[136].

A notable example of doping-induced strain effects is demonstrated by Yu et al., who incorporated Cu into the Bi lattice to introduce tensile strain, enabling the optimized $Cu_{1/6}$-Bi catalyst to achieve a formate FE efficiency exceeding 95%, an industrially relevant current density (−317 mA cm^{-2}), and excellent operational stability beyond 120 hours.[127] As shown in Figure 4b,c, theoretical analyses demonstrate how Cu incorporation modifies the Bi lattice and the reaction energetics. Figure 4b depicts DFT-calculated free-energy profiles for the $*CO_2 \rightarrow *OCHO \rightarrow *HCOOH$ pathway, showing that the $Cu_{1/6}$-Bi (2.4% tensile strain) surface significantly lowers the activation barrier compared to pristine Bi. Figure 4c shows the corresponding PDOS, where hybridization between Bi p and Cu d orbitals stabilizes OCHO intermediates near the Fermi level. Collectively, these results demonstrate that tensile strain not only facilitates CO_2 adsorption but also stabilizes key intermediates, leading to superior selectivity.

Strain engineering can also be applied to suppress competing HER. Du et al. fabricated CuAgSn alloy electrodes via magnetron co-sputtering.[128] Incorporation of Sn into the CuAg lattice induced significant lattice distortion and compressive strain, which downshifted the d-band center and substantially increased the Gibbs free energy for *H adsorption. As a result, HER was strongly suppressed, and CO selectivity improved markedly, with FE reaching 93% at –0.85 V. Figure 4d-g provide comprehensive experimental and theoretical evidence supporting this mechanism. Figure 4d presents FE_{CO} values across potentials, confirming the superior CO selectivity of CuAgSn over CuAg. The XPS spectra in Figure 4e reveal a clear downshift of the d-band center after Sn incorporation, consistent with DOS calculations, which further confirm that the d-band center of CuAgSn (–2.42 eV) lies lower than that of CuAg (–2.28 eV). The free-energy diagram in Figure 4f,g shows that COOH formation remains energetically favorable, while *H adsorption becomes less favorable, explaining the strong HER suppression and high FE_{CO}.

In another study, Jia et al. developed a continuously tunable tensile strain strategy (1.7%-4.4%) on AuPd alloys by synthesizing $Pd@Au_4Pd_1$ core-shell structures and expanding the Pd core via

View Article Online
DOI: 10.1039/D0NA00155F

phosphorization.[129] Electrochemical measurements showed that at 4.4% tensile strain, FE_{CO} increased to 94.1% (at −0.55 V vs. RHE), compared to only 75.9% for the strain-free sample, illustrating a near-linear increase in CO selectivity with strain. The theoretical origins of this performance enhancement are elucidated in Figure 4h-j. Figure 4h summarizes the DFT-calculated d-band centers, showing a progressive upshift with greater lattice expansion. Figure 4i presents the corresponding free-energy diagrams for $*CO_2 \rightarrow *COOH \rightarrow *CO$ pathway, indicating that tensile strain lowers the *COOH formation barrier while facilitating *CO desorption. Finally, Figure 4j illustrates the physical mechanism by which phosphorization expands the Pd core, generating controlled tensile strain that optimizes the binding energies of intermediates. Together, these results demonstrate that tensile strain tuning enables simultaneous enhancement of CO_2RR activity and HER suppression.

However, recent studies have shown that the relationship between strain and catalytic activity is not strictly linear. Rather than simply maximizing strain, a more nuanced approach is to identify an **optimal strain** level. In line with the Sabatier principle, excessive strain may over-stabilize intermediates, hindering CO desorption and reducing overall activity. To address this, Hao et al. proposed a thermodynamically driven **strain relaxation** strategy.[130] They synthesized PdNi alloy nanoparticles within electrospun carbon nanofiber nanoreactors, where controlled annealing temperatures induced atomic rearrangements that relaxed lattice strain from 3.2% to an optimal 2.3%. Figure 4k vividly illustrates this concept. As the synthesis temperature increases, the PdNi lattice relaxes, enabling improved atomic mixing and strain equilibration. The relaxed s-PdNi/CNFs-1000 catalyst exhibits a FE_{CO} of 96.6% at −0.88 V vs. RHE, compared with only 68.9% for the more strained s-PdNi/CNFs-800 sample. DFT calculations confirm that moderate strain relaxation optimizes *COOH formation and *CO desorption, leading to the best balance between activity and selectivity. This work highlights strain relaxation as a powerful design principle for simultaneously optimizing *COOH formation and *CO desorption, thereby enhancing both activity and selectivity in CO_2 reduction.

3.2.3. Ensemble Effect and Tandem Catalysis

The ensemble effect is a fundamental concept in heterogeneous catalysis, describing the change in activity when the geometric configuration of atomic ensembles varies with chemical composition. DFT calculations have shown that this phenomenon can be described using a linear interpolation model: the adsorption energies of intermediates on alloy surfaces are approximately the weighted average of the constituent atoms. This means that by combining two metals, the adsorption energies of intermediates can be tuned according to an "average scaling," thereby breaking the inherent limitations of monometallic catalysts.[137] A classic experimental demonstration of this effect is the in situ STM and electrochemical study of PdAu(111) surface alloys by Maroun et al., where the concept of a "**critical ensemble**" was introduced-defined as the smallest atomic ensemble required for a specific reaction step.[138] The study showed that CO adsorption only required a single Pd atom (monomer), whereas *H adsorption required at least a pair of adjacent Pd atoms (dimer). This finding highlighted that even a simple change from *CO to *H adsorption could completely alter the geometric requirements of the active site at the atomic level. This principle later became the foundation for later developments in tandem catalysis concepts.

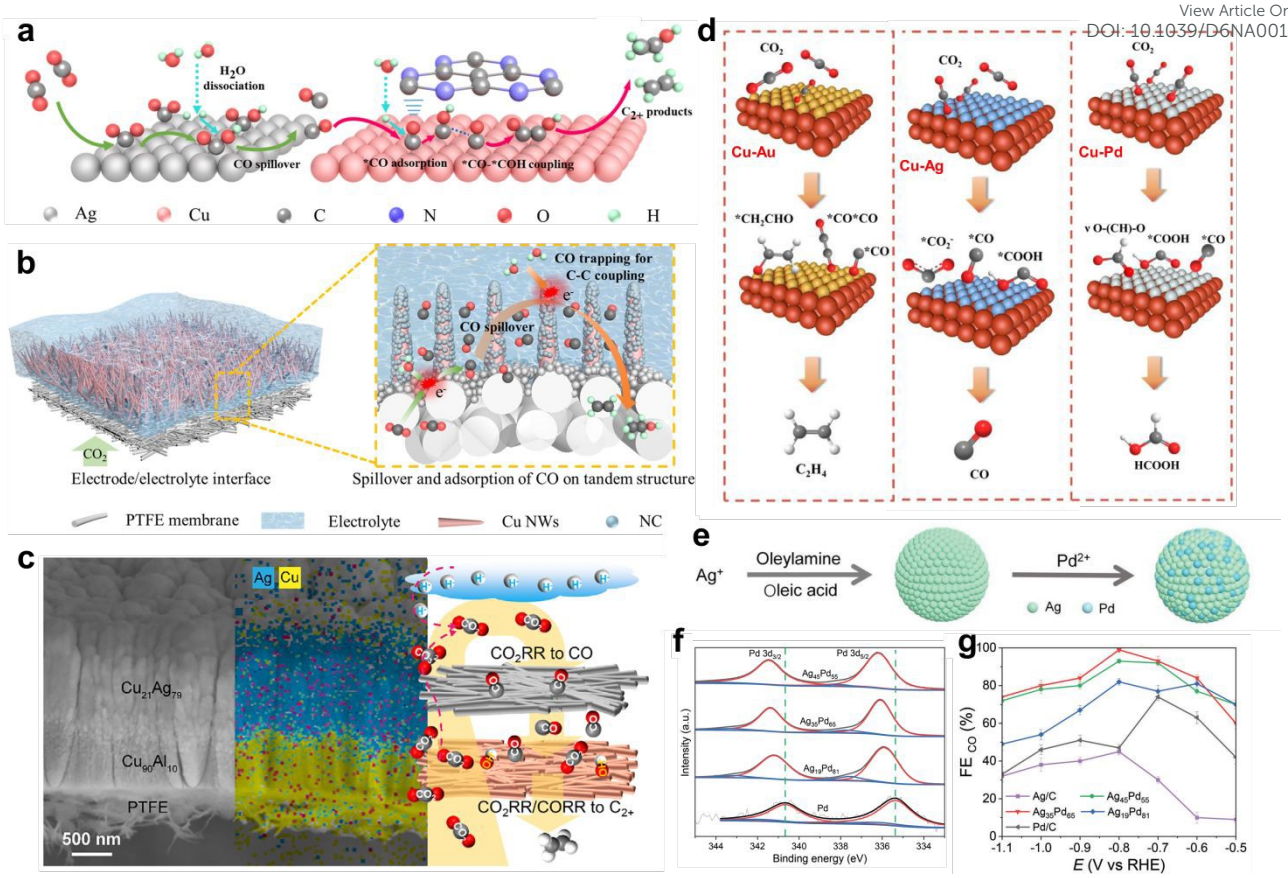

Figure 5. Ensemble and tandem catalysis mechanisms in CO_2RR. (a) Conceptual schematic of the general tandem mechanism showing sequential CO_2-to-CO and CO-to-C_{2+} conversion through CO spillover and C–C coupling between complementary active centers; (b) hierarchical Cu-Ag-NC tandem electrode enhancing CO retention and C–C coupling, reproduced from ref [139] with permission from American Chemical Society, copyright 2025. (c) Multilayer $Cu_{90}Al_{10}/Cu_{29}Ag_{71}$ architecture achieving stable C_{2+} selectivity in acidic media, reproduced from ref [94] with permission from Wiley-VCH GmbH, copyright 2025. (d) Cu–M (M = Au, Ag, Pd) interfaces modulating product distribution through differential intermediate binding, reproduced from ref [140] under the Creative Commons CC BY license. (e) Schematic synthesis of Ag–Pd nanoalloys, (f) XPS spectra showing Pd 3d downshift with Ag incorporation, and (g) composition-dependent FE_{CO} identifying optimal $Ag_{35}Pd_{65}$ performance, reproduced from ref [141] with permission from Wiley-VCH GmbH, copyright 2023.

In tandem catalysis, instead of considering only a single reaction step, different atomic ensembles are "assigned functions": one active site is optimized for the initial step, while another nearby site is designed for the subsequent step.[142] As illustrated schematically in Figure 5a, this cooperative architecture enables sequential CO_2-to-CO and CO-to-C_{2+} conversion on spatially adjacent yet electronically distinct sites. The first site (e.g., Ag) efficiently activates and reduces CO_2 to CO, while the second site (typically Cu) binds the CO intermediate more strongly, facilitating C–C coupling to form multicarbon products. Such functional differentiation between weak CO-binding and strong CO-binding centers ensures efficient intermediate transfer, and balances adsorption energies. A prominent example is the PTF(Ni)/Cu catalyst, in which isolated Ni–N sites efficiently reduce CO_2 to CO. The CO then migrates to adjacent Cu nanoparticles, which serve as secondary active sites for

View Article Online
DOI: 10.1039/D6NA00155F

C–C coupling, producing ethylene with high selectivity (FE of C_2H_4 = 57.3%).[143] Following this principle, various bimetallic tandem strategies have proven effective in tuning activity and product selectivity. Kang et al. controlled selectivity between HCOOH and CO by varying the Ni/Co ratio in Ni–Co alloys.[144] In situ infrared spectroscopy and theoretical analysis revealed that Ni sites favored *OCHO formation (leading to HCOOH), while Co sites favored *COOH (leading to CO). A Ni-rich surface (Ni_7Co_3) achieved HCOOH selectivity of 98.5%, while a Co-rich surface (Ni_3Co_7) shifted selectivity to CO with 85.4%.

Similarly, deposition of Au, Ag, and Pd on Cu(200) surfaces, normally inert, created Cu–M interfaces that enriched Cu^+ centers and modulated intermediate adsorption.[140] As illustrated in Figure 5d, Cu–Au stabilized *COOH and *CO intermediates, generating high local *CO coverage that promoted C–C coupling, yielding C_2H_4 with FE ≈ 43.2%. In contrast, Cu–Ag interfaces bound much weaker to *CO, favoring facile desorption and resulting in high CO selectivity (FE ≈ 48.0%). Meanwhile, Cu–Pd interfaces lowered the barrier for *OCHO formation, steering the reaction toward HCOOH with FE up to ≈ 50.7%. These results highlight that designing multifunctional active sites in a single nanoalloy is an effective strategy for directing reaction pathways.

For a systematic view, tandem catalysis strategies can be classified in two ways. First, based on the physical structure of active sites, they include: (1) atom-atom dual-site tandem catalysis, typical of alloys where two metals interact directly at the atomic level; (2) atom-particle dual-site tandem catalysis, combining isolated single atoms with nanoparticles to exploit interface effects; (3) particle-particle dual-site tandem catalysis, usually physical mixtures of two types of metal nanoparticles; and (4) heterogeneous interface dual-site tandem catalysis, where unique effects arise at the junction between two distinct phases.[145] Second, based on the spatial relationship between catalytic components, they can be categorized as: (i) heterogeneous interfaces, where one component is directly anchored to the host metal surface, facilitating spillover of intermediates due to minimal distance; (ii) mixed catalysts, where two types of particles are blended, with performance depending mainly on geometry and diffusion distance of intermediates rather than electronic effects; and (iii) core-shell structures, where one phase encapsulates another, enabling control of intermediate transport.[146] For tandem catalysis to operate efficiently, spatial design that ensures effective transfer of intermediates from one site to another is crucial. A systematic study by Van Der Veer et al. clarified the importance of nanoscale proximity in Cu–Ag catalysts prepared by sputtering.[93] Direct comparison of different configurations showed that layered structures (Cu-on-Ag or Ag-on-Cu), though tandem in principle, exhibited poor C_{2+} production due to restricted CO spillover between layers. In contrast, co-deposited alloys, where Cu and Ag atoms were in direct contact, delivered superior C_{2+} efficiency (up to 75%), demonstrating that nanoscale intimacy between sites is critical for successful tandem catalysis.

One of the most sophisticated applications of tandem catalysis is overcoming stability and selectivity challenges in strongly acidic media. Zhang et al. developed a multilayer tandem electrode to promote C_{2+} formation under such harsh conditions.[94] They found that individual Cu–Ag and Cu–Al alloys were unstable due to dealloying. However, during operation, $Cu_{29}Ag_{71}$ spontaneously restructured into a stable Ag(111)/Cu(100) interface, achieving very high FE_{CO} (93.1%). Leveraging this, they designed a tandem electrode with a $Cu_{90}Al_{10}$ underlayer (highly active for C–C coupling but unstable) coated with the self-restructured $Cu_{29}Ag_{71}$ layer, as depicted in Figure 5c. In this configuration, the

$Cu_{29}Ag_{71}$ layer served as both an efficient CO "factory" and a protective shield against acid corrosion, while Al atoms in $Cu_{90}Al_{10}$ strongly adsorbed OH^-, creating a locally alkaline environment that stabilized the alloy and lowered the barrier for C–C coupling. This synergistic mechanism enabled the tandem electrode to reach C_{2+} FE of 81.2% at a current density of 648 mA cm^{-2}, with a single-pass carbon efficiency (SPCE) of 70.4% and stable operation for 30 hours in acidic conditions.

Although tandem catalysis effectively increases local CO concentration, an inherent challenge remains: CO intermediates can desorb prematurely before participating in C–C coupling, reducing C_{2+} efficiency. To address this, Bian et al. developed hierarchical tandem catalysis to "trap and stabilize" CO.[139] As shown in Figure 5b, they fabricated an electrode consisting of a bottom Ag layer (for CO_2-to-CO conversion) beneath a top layer of nitrogen-doped carbon (NC)-modified Cu nanowire arrays. Geometrically, the nanowire array extended the CO diffusion path, increasing residence time. Simultaneously, Cu/NC interfaces enhanced CO trapping and stabilization through linear adsorption, confirmed by in situ spectroscopy. This strategy yielded C_{2+} FE up to 87.5% at high current density, with a C_{2+}/C_1 ratio of 10.42 and remarkable stability for 50 hours, highlighting how geometrical and interfacial confinement strengthen tandem synergy.

To further enhance tandem catalysis, recent strategies have focused on controlling the microenvironment surrounding active sites. A representative example is the a-Ni/Cu-NP@CMK catalyst reported by Chen et al.[147]. In this system, Cu nanoparticles (~3.2 nm) were confined within hydrophobic mesoporous carbon (CMK-8), pre-doped with atomically dispersed Ni–N_4 sites. This design provided dual synergy: (i) tandem catalysis, where Ni–N_4 efficiently produced CO from CO_2, which was then supplied to adjacent Cu nanoparticles for C–C coupling into ethylene; and (ii) microenvironment engineering, where the hydrophobic CMK-8 restricted water access, strongly suppressing HER and enhancing CO_2RR selectivity. As a result, a-Ni/Cu-NP@CMK achieved ethylene FE of 72.3% at a high current density of 406.1 mA cm^{-2} in neutral electrolyte. Another unique approach is the use of polymer coatings to create tandem effects by controlling the microenvironment. Instead of directly participating in reactions, the polymer regulates the local chemical environment at the catalyst/electrolyte interface. For instance, hydrophobic polymer layers on Cu surfaces enrich CO_2 while excluding H_2O near active sites, effectively suppressing HER and enhancing adsorption of intermediates critical for C–C coupling. Additionally, functional groups in polymers can hydrogen-bond with oxygenated intermediates, stabilizing them and steering selectivity toward products such as ethanol.[148] This strategy opens a new paradigm in which tandem effects arise not only from cooperation between catalytic centers but also from subtle interactions between catalysts and tailored polymer overlayers.

Palladium alloying is also an effective strategy for optimizing CO production. While Pd readily activates CO_2, it suffers from overly strong *CO binding that hinders desorption. To address this, Zeng et al. alloyed Pd with Ag, a weaker CO-binding metal (Figure 5e-g).[141] Figure 5e shows the synthesis route of ultrasmall Ag–Pd nanoparticles (~3.58 nm) via oleylamine/oleic acid reduction, forming mixed-ensemble surfaces. The resulting ensemble sites containing both Ag and Pd effectively reduced the energy difference between *COOH and *CO. This mechanism either weakened *CO adsorption or strengthened *COOH adsorption relative to pure Pd, facilitating the catalytic cycle. Electronically, alloying with Ag shifted the Pd d-band downward, stabilizing d-electrons and weakening *CO binding (Figure 5f). Owing to the combined ensemble, electronic, and

View Article Online
DOI: 10.1039/D6NA00155F

size effects of ultrasmall nanoparticles (~3.58 nm), the optimized $Ag_{35}Pd_{65}$ alloy catalyst achieved FE_{CO} of 98.9% at −0.8 V vs. RHE (Figure 5g).

Nevertheless, a persistent challenge in studying the ensemble effect is that alloying often simultaneously alters both electronic structure and geometry, making it difficult to decouple their roles. Gong et al. proposed an alternative approach: comparing different polymorphs of the same Pd_3Bi alloy with identical composition.[149] This allowed geometric effects to be isolated from electronic ones. The study found that ordered Pd_3Bi intermetallics formed small Pd ensembles (1-5 atoms) and were nearly inactive for methanol oxidation reaction (MOR), whereas disordered solid-solution Pd_3Bi created larger ensembles (average ~5.25 atoms, maximum 6) and exhibited high activity (~0.5 mA cm_{Pd}^{-2}). Partially ordered structures gave intermediate performance (~0.1 mA cm_{Pd}^{-2}). XPS and XANES analyses showed nearly identical electronic structures across samples, confirming that activity differences originated purely from ensemble size. This provides compelling evidence that the geometry of active sites can switch catalytic activity "on/off" independently of electronic structure, opening new pathways for designing catalysts with tunable active site ensembles while preserving electronic character.

3.2.4. Inhibition of HER

One of the main challenges of CO_2RR is suppressing the competing HER. Nanoalloy designs can tailor catalyst surfaces to minimize H_2 formation.[150]

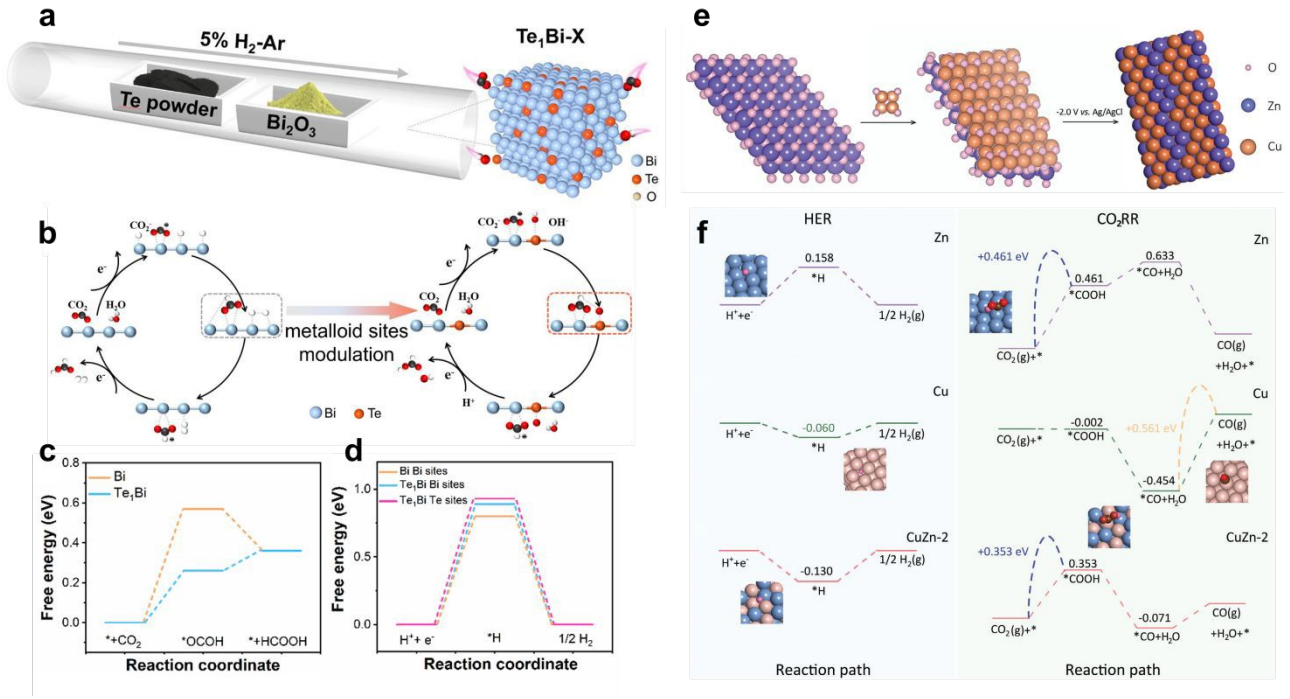

Figure 6. Alloying strategies for suppressing HER during CO_2 electroreduction. (a) Synthesis of Te_1Bi single-atom alloy via reduction and alloying; (b) reaction mechanism of Te_1Bi showing Bi–Te antagonistic sites that hinder *H coupling and promote *OCHO formation; and (c, d) DFT energy diagrams showing higher *H adsorption barriers and stabilized *OCHO intermediates on Te_1Bi, reproduced from ref [151] with permission from Elsevier Ltd, copyright 2024. (e) Formation of Cu–Zn nanorods by electroreduction of Cu_2O/ZnO precursors on carbon cloth; and (f) Free-energy profiles

for HER and CO_2RR on Zn, Cu, and Cu–Zn, reproduced from ref [152] with permission from Wiley-VCH GmbH, copyright 2024.

A representative demonstration of alloying to suppress HER in acidic media is the "metalloid-metal single-atom alloy" Te_1Bi.[151] Introducing the nonmetallic Te atom into a Bi host created antagonism sites with dual effects: (i) geometric hindrance preventing *H coupling and thus suppressing H_2 formation; and (ii) OH^- adsorption as a proton source, spatially separating proton and electron supply, thereby favoring *OCHO formation at Bi sites and steering selectivity toward HCOOH instead of HER. As illustrated in Figure 6a, the Te_1Bi single-atom alloy was synthesized via the reduction and alloying of Bi_2O_3 and Te under a 5% H_2-Ar atmosphere, generating an atomically dispersed Te within the Bi lattice. This atomic arrangement introduces alternating Bi and Te sites that modulate surface charge distribution and proton accessibility (Figure 6b). The Te sites act as electronically negative centers that repel protons and block *H coupling, while neighboring Bi atoms serve as active sites for $*CO_2$ activation and *OCHO stabilization. The synergistic Bi–Te interaction therefore reconstructs the catalytic microenvironment-suppressing HER and enhancing CO_2 reduction toward formate. Operando Raman, SR-FTIR, and NAP-XPS measurements, combined with theoretical calculations, revealed significantly higher *H adsorption barriers on both Bi sites and Te sites relative to pure Bi (Figure 6d), while the energy pathway for *OCHO formation was lowered (Figure 6c). As a result, Te_1Bi achieved FE_{HCOOH} of 94.5%, SPCE of 40%, and $j_{HCOOH} \approx 0.2$ A cm^{-2} in strong acidic electrolyte, far surpassing pure Bi, which mainly produced H_2. This study highlighted that atomic-level alloying can deliberately control the microenvironment and proton pathways to simultaneously suppress HER and enhance CO_2RR selectivity.

To further elucidate the synergy, Liu et al. combined experiments and DFT to demonstrate that Cu–Zn alloys balance CO_2RR and HER by assigning specialized roles to each metal.[152] As shown in Figure 6e, the Cu–Zn alloy was synthesized by electrodepositing Cu_2O beneath ZnO nanotube arrays on carbon cloth, followed by electroreduction that converted Cu_2O/ZnO precursors into metallic Cu–Zn alloys. This in situ alloying places Cu and Zn in direct contact, enabling the two metals to assume complementary catalytic roles on the same interface. Cu lowered the energy barrier for the initial CO_2 activation to *COOH, a step difficult on pure Zn. In contrast, Zn weakened CO binding relative to pure Cu, facilitating CO desorption instead of deep reduction or surface poisoning. Meanwhile, Cu–Zn alloys exhibited moderate *H adsorption, preventing excessive HER and maintaining CO_2RR dominance. This behavior is quantified in Figure 6f. On pure Cu, the adsorption free energy of *H ($\Delta G_{*H} \approx -0.060$ eV) is favorable, enabling rapid H_2 evolution, while CO desorption remains energetically demanding. On Zn, *H adsorption is too unfavorable ($\Delta G_{*H} \approx +0.158$ eV) and *COOH formation is difficult, limiting both HER and CO_2 activation. In contrast, the Cu–Zn alloy exhibits an intermediate *H adsorption energy ($\Delta G_{*H} \approx -0.130$ eV), high enough to slow HER, alongside a moderated barrier for CO_2 to *COOH and a lower barrier for *COOH to *CO. This "task division" at the atomic scale allowed flexible tuning of H_2/CO ratios in syngas (0.8 - 5.8) simply by adjusting the applied potential.

Beyond alloy composition, other approaches include electrode architecture to control HER. Zhang et al. reported a hollow-fiber Cu–Bi alloy electrode.[153] In this system, CO_2 was delivered "inside-out" through hollow fibers, creating a gas barrier that restricted electrolyte infiltration into pores. This limited local proton availability, strongly suppressing HER while maintaining high CO_2 concentration

View Article Online
DOI: 10.1039/D6NA00155F

at the triple-phase boundary. Surface modification via alkaline oxidation and hydrothermal sulfuration yielded Cu_7S_4–CuBi nanoflowers with large electrochemical surface area and superior wettability. At −0.9 V vs. RHE, the electrode achieved $FE_{formate}$ of 91.27% with a partial current density of 80.12 mA cm^{-2}, outperforming other Cu@Bi systems. The mechanism involved a rate-determining electron transfer forming CO_2*−, followed by protonation to HCOO*. The synergy of stable Cu^+, sulfur incorporation, and hollow-fiber architecture promoted formate selectivity and maintained stability for 12 h of continuous electrolysis. This work demonstrated a self-supported electrode strategy that combined high performance, industrial-level current density, and effective HER suppression.

3.2.5. Enhancing Stability

Long-term durability remains one of the major barriers to the commercialization of CO_2RR catalysts. As comprehensively analyzed in a recent review by Lai et al., the degradation of stability is a multi-scale challenge involving thermodynamic, kinetic, and structural factors that span from the atomic level to the entire electrolysis system.[154] Thus, alloying strategies not only enhance activity and selectivity but also play a vital role in extending catalyst lifetimes.

At the catalyst level, nanoalloys are particularly susceptible to atomic-scale reconstruction, phase segregation, and elemental leaching. For instance, as previously discussed in the work by Zhang et al.[94], Cu-Ag and Cu-Al systems are prone to dealloying and instability under harsh conditions. Furthermore, Lai et al. highlighted that the dissolution-re-deposition process (Ostwald ripening) under cathodic potentials can cause particle agglomeration, significantly reducing the electrochemical active surface area.[154] These atomic-scale instabilities, particularly severe in Cu-based systems under reducing conditions, lead to rapid performance loss and increased HER.

To counteract these degradation mechanisms, intermetallic alloy design, with ordered atomic arrangements, mitigates phase segregation, preserves electronic interactions, and stabilizes intermediate oxidation states (Cu^+/Cu^0) critical for C–C coupling. Moreover, the secondary alloy atoms can act as "anchors" that limit Cu atom mobility, directly addressing the issues of Ostwald ripening and agglomeration mentioned above.[155] Thus, Cu–M intermetallics provide both electronic synergy (tuning adsorption energies of intermediates) and structural robustness against long-term degradation. A prime example is the work by Kuang et al. recently synthesized ordered CuAu intermetallics (o-CuAu) at low temperature (~250 °C).[156] Results showed atomic ordering was key to stability: o-CuAu maintained FE_{CO} ~60% for 160 h in a membrane electrode assembly (MEA) cell at 100 mA cm^{-2}, while disordered CuAu (d-CuAu) quickly lost selectivity due to restructuring into unstable Cu-rich phases. The superior stability of o-CuAu was attributed to high mixing enthalpy and strong Cu–Au interactions, which suppressed phase segregation. Furthermore, highly valent Au atoms in the intermetallic structure facilitated CO_2 activation and stabilized $*CO_2^{\bullet-}$ intermediates.

Another effective solution to address structural instability during prolonged electrolysis is to introduce a small fraction of a third element to enhance durability. For example, Jia et al.[157] incorporated ~3 at.% Zn into the shell of Cu@CuAu core-shell catalysts. While Cu@CuAu rapidly lost activity, Cu@CuAuZn maintained high CO selectivity (FE 82%) and stable current for 10 h. Detailed analysis showed Zn atoms acted as "locks" in the alloy lattice. Based on solid solution strengthening, Zn increased the energy barrier for Cu and Au atom migration, preventing their

View Article Online
DOI: 10.1039/D6NA00155F

dissolution. Post-reaction electron microscopy confirmed that Zn-containing catalysts experienced less corrosion and retained their core-shell structure.

Another demonstration of structural protection is the CoNi nanoalloy encapsulated in N-doped carbon nanotubes (CoNi@N-CNTs).[158] This design combined electronic synergy between Co and Ni with protective N-CNT shells, preventing corrosion, reconstruction, and deactivation under harsh conditions. CoNi@N-CNTs maintained FE_{CO} above 90% across acidic, neutral, and alkaline media, with current densities up to 732 mA cm^{-2}, while remaining stable for more than 36 h in acidic conditions. Mechanistic analysis revealed electron transfer from Co to Ni modified the electronic distribution, optimizing adsorption-desorption of intermediates, thereby enhancing CO_2RR selectivity and extending catalyst lifetime.

However, it is important to note that highly ordered intermetallics or heavily protected structures may also eliminate necessary atomic ensembles for catalysis. As demonstrated in Pd_3Bi, ordered phases were completely inactive compared to disordered solid solutions, despite identical composition and electronic structure.[149] This highlights a critical trade-off in catalyst design: stability must be balanced with the presence of active ensembles.

Beyond the catalyst itself, Lai et al. pointed out that stability is also heavily governed by micro- and macro-scale system failures, notably electrode flooding and salt precipitation.[154] In gas-diffusion electrodes (GDEs), the accumulation of liquid products or electrolytes within the pores obstructs CO_2 transport, while the local pH increase facilitates the formation of carbonate/bicarbonate salts that physically block the triple-phase boundary. To address these systemic challenges, operational regulation strategies must be deployed alongside material design. An excellent example of this synergy is the work by Van Der Veer et al., who applied pulsed electrolysis, alternating steady-state CO_2 reduction with brief oxidative pulses.[93] These pulses temporarily re-oxidized the surface, forming a stable Cu_2O layer, which not only slowed surface reconstruction but also actively mitigated electrode flooding. This extended catalyst lifetime from ~1 h to 6 h, underscoring the potential of operational control to sustain performance. Therefore, achieving industrial-scale durability requires a holistic strategy that bridges robust nanoalloy engineering with optimized system integration and advanced operational protocols.

4. Tuning Target Products via Nanoalloy Design

One of the most prominent advantages of nanoalloys is their ability to tune product selectivity through careful design of catalyst composition and structure. Depending on the metal constituents, mixing ratios, nanostructure morphology, and electrochemical environment, nanoalloy systems can be directed to preferentially produce specific products.

View Article Online
DOI: 10.1039/D6NA00155F

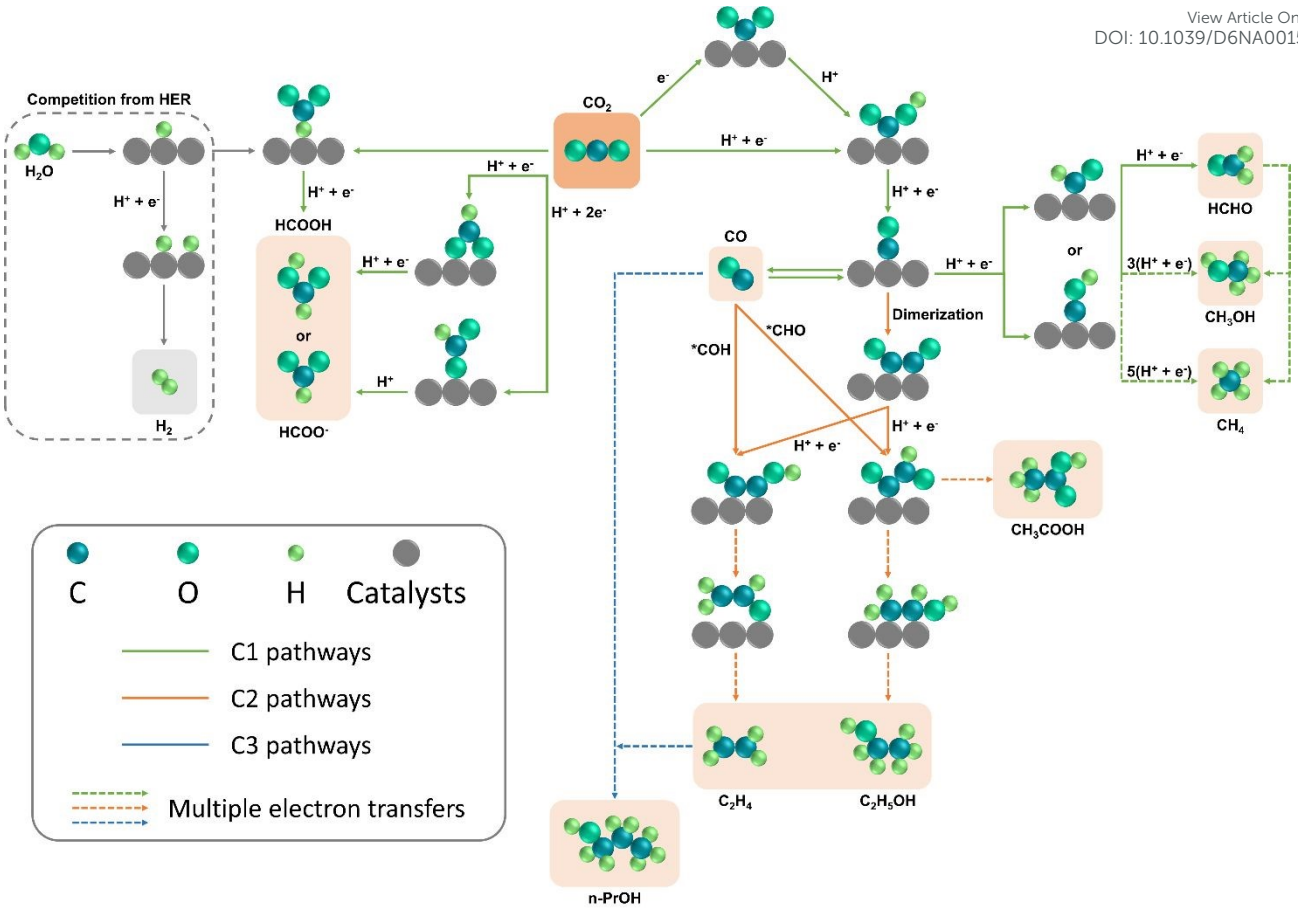

Figure 7. Reaction network of CO_2RR showing key intermediates and coupling pathways leading to C_1, C_2, and C_3 products.

4.1. C_1 Products

In CO_2RR, C_1 products encompass a diverse spectrum, ranging from simple two-electron transfer species like CO and HCOOH to more deeply reduced and complex compounds such as HCHO, CH_3OH, and CH_4. Selectivity within this group is fundamentally governed by the initial competition between two key intermediates: the stabilization of *OCHO favors HCOOH formation, whereas the stabilization of *COOH directs the pathway toward *CO. Beyond initial CO desorption, driving the reaction toward deeper hydrogenation (HCHO, CH_3OH, or CH_4) significantly elevates the kinetic complexity. The selectivity among these challenging targets depends heavily on the catalyst's ability to precisely tune the binding strength of *CO and subsequent downstream intermediates, which ultimately determines whether the C–O bond is preserved or entirely cleaved. While the simpler C_1 products can often achieve very high FE due to their lower kinetic barriers, selectively synthesizing highly reduced C_1 oxygenates and hydrocarbons remains a formidable yet highly rewarding objective to maximize the energy density and commercial value of the outputs.

4.1.1. Carbon monoxide

CO is one of the simplest products of CO_2 reduction, requiring only a two-electron transfer. The widely accepted pathway for CO formation proceeds via the *COOH intermediate. The process begins with CO_2 adsorption and activation on the catalyst surface, followed by a coupled proton-electron transfer to form *COOH, where CO_2 binds through the carbon atom. The next step involves

View Article Online
DOI: 10.1039/D6NA00155F

heterolytic C–OH bond cleavage in *COOH, yielding the *CO intermediate and releasing a water molecule. Finally, because of its relatively weak binding to many metals, *CO desorbs easily to form CO (Figure 7).[70,72,159,160] Thus, an effective CO-selective catalyst must stabilize *COOH while binding *CO weakly enough to prevent further hydrogenation.

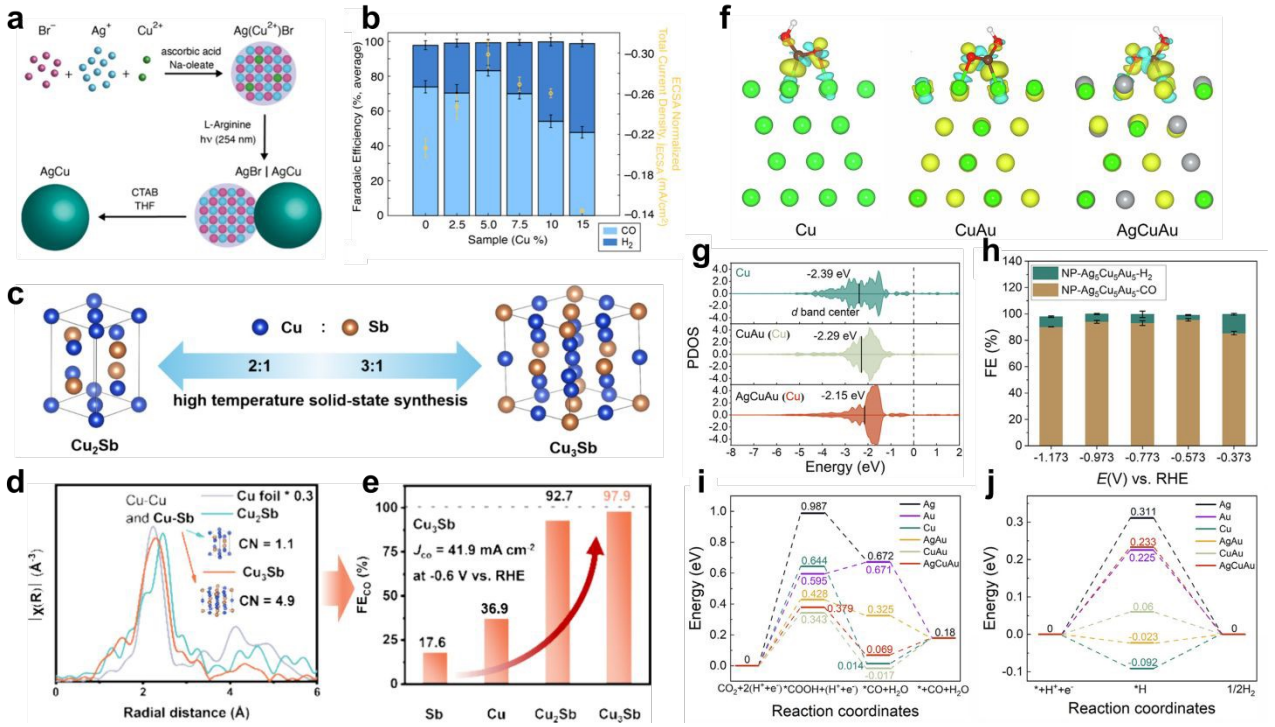

Figure 8. (a) Host-guest synthesis method for AgCu nanoalloys, (b) dependence of FE_{CO} and total current on Cu composition, reproduced from ref [90] with permission from American Chemical Society, copyright 2024. (c) Cu–Sb intermetallic formation via high temperature solid-state synthesis, (d) EXAFS spectra showing Cu–Sb coordination in Cu_2Sb and Cu_3Sb, (e) CO formation efficiency of Cu–Sb intermetallics, reproduced from ref [161] with permission from American Chemical Society, copyright 2024. (f) Structure of AgCuAu ternary alloy, (g) PDOS of Cu d-band upshift upon alloying, (h) FE_{CO} of nanoporous $Ag_5Cu_5Au_5$ over various potentials, (i) free-energy diagram for *COOH formation, and (j) *H adsorption on AgCuAu, reproduced from ref [162] with permission from Science Press and Dalian Institute of Chemical Physics, Chinese Academy of Sciences, copyright 2024.

Śliwa et al. employed a "host-guest" approach to synthesize AgCu nanoalloys with Cu content precisely controlled from 0% to 15%.[90] As illustrated in Figure 8a, the synthesis involved the sequential formation of $Ag(Cu^{x+})Br$ host particles, co-reduction of interstitial Ag^+ and Cu^{x+} cations to generate metallic AgCu domains, and subsequent removal of the AgBr phase, yielding phase-pure "Cu-in-Ag" alloy nanoparticles with precisely tunable Cu composition. Experimental results revealed that CO selectivity correlated with alloy composition, peaking at 83.2% FE with 5% nominal Cu at −0.5 V vs. RHE (Figure 8b). Increasing Cu content to 15% sharply decreased CO efficiency to 50%, while HER became dominant. This decline was attributed to the formation of Cu-rich phases beyond solubility limits, which are highly active for HER.

An effective strategy to enhance CO selectivity is to form intermetallic compounds with p-block elements such as Sb. As shown in Figure 8c, Huang et al. synthesized highly ordered Cu–Sb intermetallics, Cu_2Sb and Cu_3Sb, via high-temperature solid-state synthesis methods, enabling

View Article Online
DOI: 10.1039/D6NA00155F

precise tuning of Cu coordination.[161] They demonstrated that adjusting the coordination environment of Cu atoms by alloying with Sb effectively suppressed HER and C–C coupling, thereby significantly improving CO selectivity. Extended X-ray absorption fine structure analysis (EXAFS, Figure 8d) revealed an increased Cu–Sb coordination numbers in Cu_3Sb (CN = 4.9) relative to Cu_2Sb (CN = 1.1), producing a distinct electronic environment around Cu active sites. Consequently, Cu_3Sb exhibited outstanding CO_2RR performance, achieving FE_{CO} up to 97.9% at −0.6 V vs. RHE, with an impressive CO partial current density of ~42.8 mA cm^{-2} (Figure 8e). This catalyst also showed high stability in both flow cells and MEAs. In situ Raman spectroscopy further confirmed *COOH as the key intermediate, verifying a selective CO pathway without detectable HCOOH or C_{2+} products.

Moving beyond binary systems, multi-component alloys offer greater flexibility in fine-tuning electronic and geometric effects. Wang et al. combined DFT and experiments to design a ternary AgCuAu alloy (Figure 8f) with superior CO selectivity.[162] DFT analysis revealed that Cu atoms served as the primary active sites, while adjacent Ag and Au atoms modulated the local electronic structure, shifting the Cu d-band center closer to the Fermi level (Figure 8g). This shift lowered the barrier for *COOH formation (Figure 8i) and raised the barrier for *H adsorption (Figure 8j), thereby enhancing CO selectivity while suppressing HER. To validate these predictions, the team synthesized nanoporous NP-$Ag_5Cu_5Au_5$ by dealloying. Experiments confirmed the predictions: the ternary alloy delivered FE_{CO} above 90% across a wide potential window of 0.6 V, peaking at ~96% at −0.573 V vs. RHE (Figure 8h). This far outperformed both monometallic and bimetallic counterparts. This work compellingly demonstrated the power of multi-component alloy design, where synergistic electronic effects can simultaneously optimize multiple steps, yielding catalysts with high activity, excellent selectivity, and wide potential stability.

An important industrial application of CO_2RR is controlled production of syngas (CO + H_2), a key feedstock for many chemical processes. The challenge lies in deliberately balancing CO_2RR to CO with HER to H_2. Nanoalloys of non-precious metals have proven to be an effective and economical strategy to address this. For instance, Song et al. investigated Cu–Fe alloys supported on N-doped carbon (CuFe/NC).[163] They demonstrated tunable H_2/CO ratios from 0 to 1.94 by adjusting the Cu:Fe ratio and applied potential. The optimal Cu_1Fe_2/NC catalyst achieved excellent performance, with FE_{CO} up to 98.91% at −0.7 V vs. RHE, while maintaining stability for 24 h. XPS analysis revealed the underlying mechanism: because Cu is more electronegative than Fe, electron transfer occurred from Fe to Cu, redistributing electronic density, shifting the Cu d-band, and optimizing intermediate binding energies to balance CO_2RR and HER.

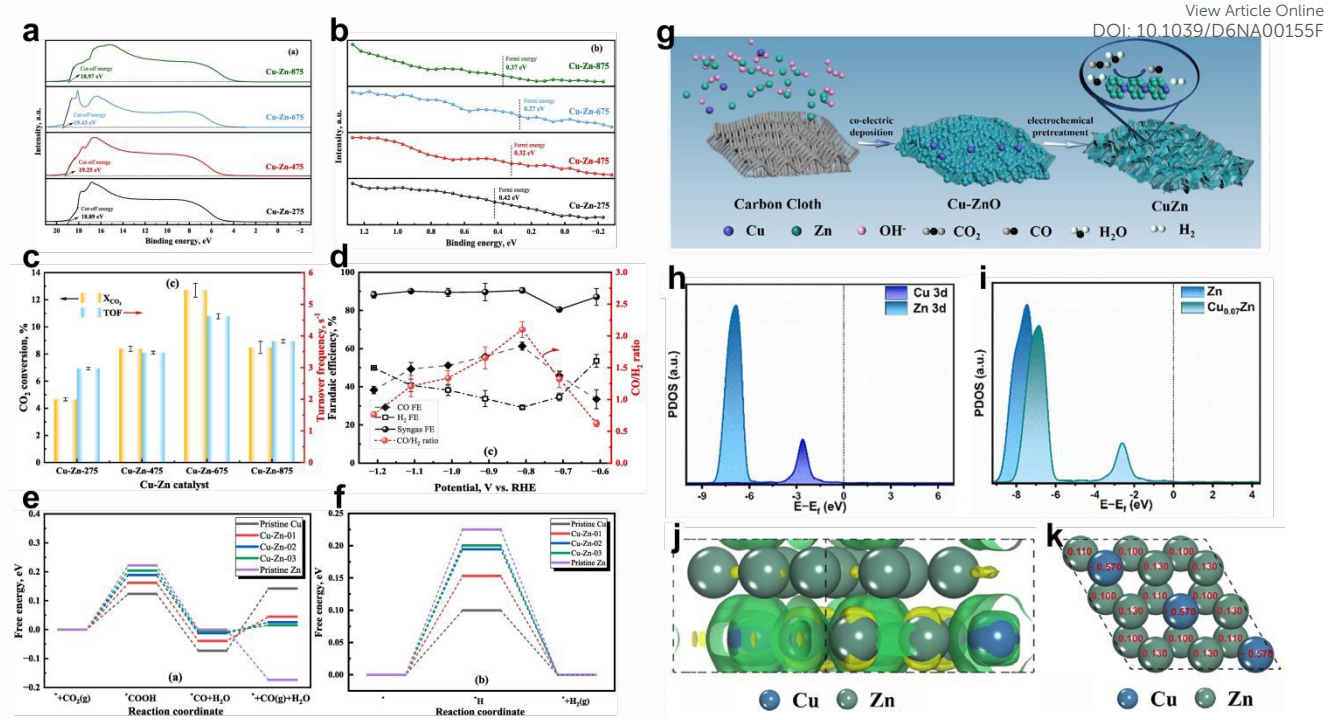

Figure 9. (a) UPS spectra showing secondary electron cut-off edge, (b) Fermi edge, (c) CO_2 conversion and turnover frequency of Cu–Zn catalysts; (d) FEs and CO/H_2 ratios of Cu-Zn-675 at different potentials; (e) free-energy diagram for CO_2RR, (f) for HER on Cu, Zn, and Cu–Zn alloy surfaces, reproduced from ref [164] with permission from Elsevier Ltd, copyright 2025. (g) Schematic illustration of Cu–Zn nanosheet synthesis via electrodeposition; (h) PDOS of Cu 3d and Zn 3d states in $Cu_{0.07}Zn$; (i) comparison of PDOS for Zn and $Cu_{0.07}Zn$; (j) charge density difference map of Cu–Zn alloy surface; and (k) Bader charge analysis of Cu–Zn alloy showing charge distribution between Cu and Zn atoms, reproduced from ref [165] with permission from Wiley-VCH GmbH, copyright 2025.

Similarly, Cu–Zn alloys have emerged as promising candidates for syngas production. Guo et al. investigated Cu–Zn alloys with precisely controlled Zn loadings prepared by electrodeposition.[164] Systematic characterization revealed a strong composition-dependent electronic interaction between Cu and Zn. Ultraviolet photoelectron spectroscopy (UPS, Figure 9a,b) showed that the cut-off and Fermi energies varied non-monotonically with Zn content, reaching optimal values for the Cu-Zn-675 sample. This composition exhibited the lowest work function (2.06 eV), indicating facile electron transfer across the Cu–Zn interface. Experimental results further show that the Cu-Zn-675 catalyst exhibited the highest CO_2 conversion (12.7%) and turnover frequency (TOF) (4.62 s^{-1}) (Figure 9c), along with nearly 90% FE for syngas and a tunable CO/H_2 ratio up to 2.1 at −0.81 V vs. RHE (Figure 9d). DFT analysis (Figure 9e,f) revealed that the introduction of Zn tuned the adsorption energetics of key intermediates: the Cu–Zn surface exhibited moderate *COOH and *H binding, lowering the *CO desorption barrier and weakening *H adsorption relative to pure Cu. This balance between CO_2 reduction and H_2 evolution explains the experimentally observed CO/H_2 tunability. Overall, Cu–Zn alloys integrate the favorable CO_2 activation of Cu with the weak CO binding of Zn, creating a bifunctional interface that enables efficient and controllable syngas production with suppressed HER.

Along the same lines, Zou et al. synthesized Cu–Zn nanosheet alloys via electrodeposition (Figure 9g).[165] Their work demonstrated CO/H_2 ratio tunability from 1.1 to 4.3 by adjusting Cu:Zn ratio and

View Article Online
DOI: 10.1039/D6NA00155F

applied potential, achieving nearly 100% FE for syngas with excellent durability. XPS and DFT analyses revealed electron transfer from Zn to Cu, which increased the density of Cu 3d states near the Fermi level. As shown in Figure 9h, the PDOS analysis reveals that the Cu 3d states are positioned closer to the Fermi level than the Zn 3d states, reflecting an increased electron density surrounding Cu atoms. Moreover, in Figure 9i, compared with pure Zn, the overall d-band of the $Cu_{0.07}Zn$ nanosheets shifts toward the Fermi level, confirming that Cu incorporation enhances the electronic density near the active Cu sites and strengthens their capacity for CO_2 activation. The differential charge density map (Figure 9j) reveals charge redistribution at the Cu–Zn interface, where electrons migrate from Zn to Cu, leading to electron-enriched Cu sites. Bader charge analysis (Figure 9k) quantitatively supports these findings, showing approximately 1.71 |e| transferred from Zn to Cu in the active $CuZn_5$ phase. This substantial charge migration modulates the surface electronic environment, resulting in an optimal balance between CO_2 activation and H adsorption.

4.1.2. Formic acid / Formate

HCOOH or its salts ($HCOO^-$) is a valuable two-electron CO_2 reduction product, widely used in industry and considered a promising hydrogen carrier. Mechanistically, the pathway for formate formation diverges clearly from the CO pathway at the very first steps. While CO formation proceeds through the *COOH intermediate, in which CO_2 binds to the catalyst surface via the carbon atom (C-bound), high selectivity toward formate relies on the catalyst's ability to preferentially form and stabilize the *OCHO intermediate, where CO_2 is adsorbed through oxygen-metal coordination (O-bound). Several pathways have been proposed for *OCHO formation. In the first (pathway 1), CO_2 accepts one electron to form an adsorbed radical anion ($*CO_2^{\bullet-}$), which is then directly protonated to generate *OCHO. Alternatively, in pathway 2, CO_2 can interact with surface-adsorbed hydrogen in the form of a metal–hydride (M–H) bond, where CO_2 inserts directly into the M–H linkage to yield *OCHO. The *OCHO intermediate is subsequently hydrogenated and desorbed to produce HCOOH in acidic media or $HCOO^-$ in alkaline conditions (Figure 7).[51,70,72,160,166] Therefore, an effective catalyst for the production of formate must not only stabilize *OCHO but also suppress competing pathways, particularly HER and *COOH formation.[167] p-block metals such as Sn, In, and Bi typically exhibit these properties, and alloying them with other metals can further enhance *OCHO stabilization at bimetallic interfaces.

View Article Online
DOI: 10.1039/D6NA00155F

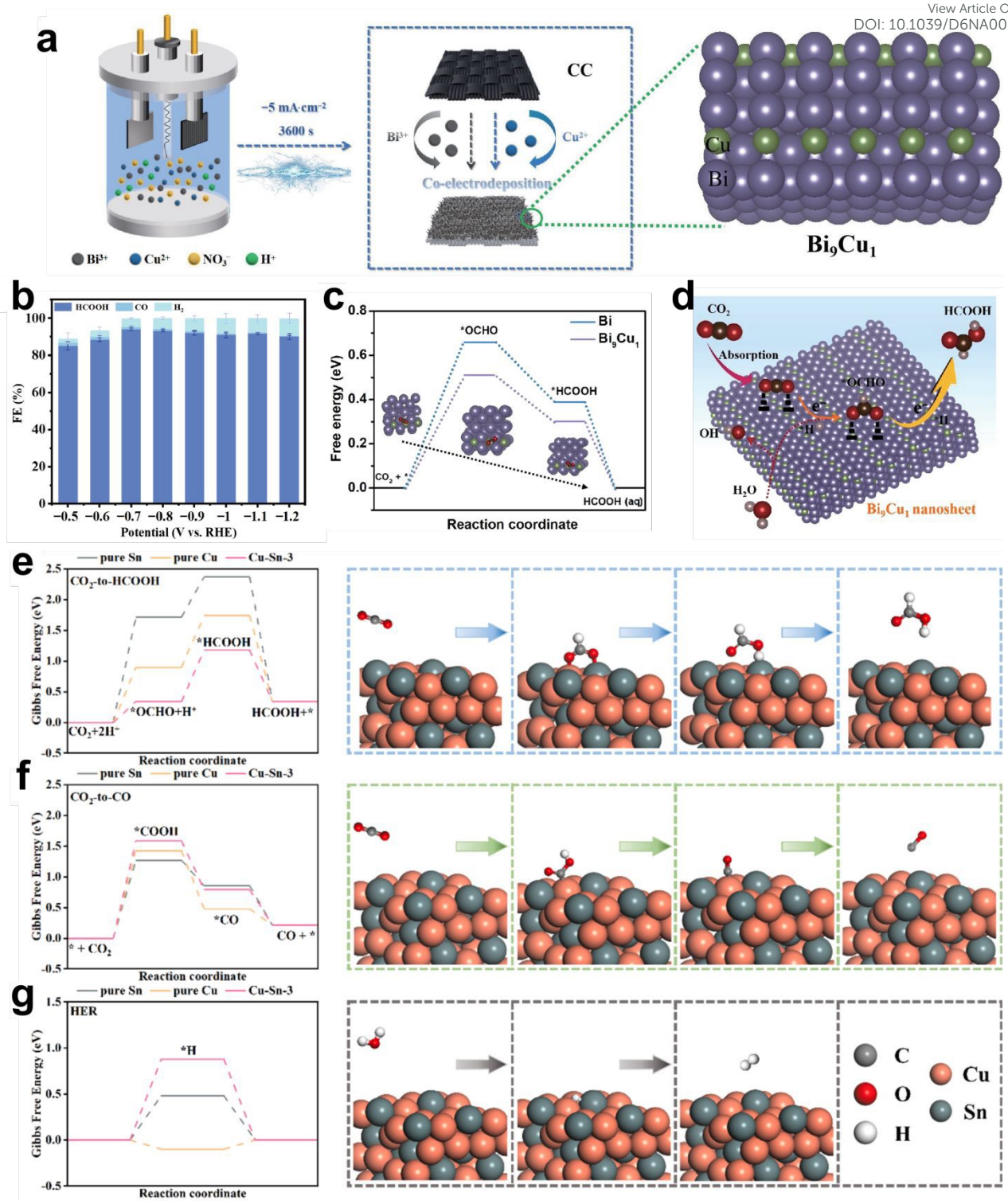

Figure 10. (a) Schematic illustration of the electrodeposition process for fabricating Bi–Cu alloys; (b) FE of formate for Bi_9Cu_1 sample at different potentials; (c) DFT-calculated free-energy diagram; and (d) schematic representation of *OCHO adsorption and hydrogenation on Bi–Cu interfacial sites, reproduced from ref [168] with permission from Tsinghua University Press, copyright 2023. Gibbs free energy profiles on Cu–Sn alloy surfaces for (e) CO_2-to-HCOOH; (f) CO_2-to-CO, and (g) HER pathways, reproduced from ref [92] with permission from Elsevier B.V., copyright 2024.

View Article Online
DOI: 10.1039/D6NA00155F

Accordingly, a common strategy to enhance formate production is alloying p-block metals (e.g., Bi, Sn, In) with other metals to optimize electronic structure and reaction kinetics. Wu et al. reported a representative study on Bi–Cu alloys, synthesizing Bi_9Cu_1 nanosheet catalysts supported on carbon cloth (Bi_9Cu_1/CC) via electrodeposition (Figure 10a).[168] The Bi_9Cu_1/CC catalyst demonstrated outstanding performance, achieving FE for formate above 90% across a wide potential range (−0.7 to −1.2 V vs. RHE) in a flow cell (Figure 10b). In situ ATR-IR spectroscopy confirmed that the fundamental pathway remained via the *OCHO intermediate. However, DFT calculations revealed the electronic effect of Cu incorporation: introducing a small amount of Cu into Bi increased the density of states near the Fermi level, improving conductivity, optimizing *OCHO adsorption energy, and lowering the barrier for conversion to HCOOH at Bi–Cu interfacial sites (Figure 10c,d).

In addition to Bi, Sn is also distinguished by its high selectivity toward formate, and alloying Sn with other metals has been extensively explored to enhance the efficiency and durability of CO_2RR. However, one of the major challenges for Sn-based catalysts is the instability of the active oxide phase. Although high-valence Sn centers are considered to play a crucial role in formate formation, they are readily reduced to metallic tin (Sn^0) under negative potentials, leading to activity loss and enhanced HER. To address this issue, an effective approach is interface engineering to stabilize the oxidation state of the active centers. In a recent study by Fan et al., the incorporation of Cu into tin oxide catalysts induced in-situ reconstruction under electrolysis conditions, forming a core-shell structure with a Cu_6Sn_5 alloy core and an amorphous SnO_x shell.[169] In-situ analyses combined with DFT calculations revealed that the Cu_6Sn_5/SnO_x interface plays a crucial role in stabilizing high-valence Sn species on the surface, preventing their reduction to Sn^0 even under negative potentials and high current densities. The Sn^{4+}-rich surface strongly promotes the formation and stabilization of the OCHO intermediate, the direct precursor of formate, whereas Sn^0 sites preferentially catalyze HER or the CO pathway via COOH. Owing to this stabilization mechanism, the R-$CuSnO_3$ catalyst exhibited efficient activity across the entire pH range, achieving a maximum FE for $HCOO^-$ of 93.4% at –0.9 V in H-cell (0.5 M $KHCO_3$). In a flow cell, the catalyst maintained 88.4% FE at a current density of 800 mA cm^{-2} (corresponding to $j_{formate}$ = 707 mA cm^{-2}, with a formate formation rate of 13.2 mmol h^{-1} cm^{-2} in 1 M KOH) and 87.8% FE at 300 mA cm^{-2} in a strongly acidic medium (0.1 M H_2SO_4 + 1 M K^+). Furthermore, operational stability was demonstrated with ~90% FE maintained over 90 h at –100 mA cm^{-2}. In a complementary approach, Li et al. exploited dynamic reconstruction in heterogeneous catalysis, where the structure and surface composition of the catalyst evolve under reaction conditions to form the real active phase.[170] Although the initial material was SnO_2 doped with a small amount of Cu, in-situ and ex-situ analyses revealed that under the reductive potentials of CO_2RR, the catalyst spontaneously reconstructed to form Cu–Sn nanophases, specifically the Cu_6Sn_5 phase. In-situ ATR-FTIR measurements recorded a distinct OCHO signal at 1390 cm^{-1}, while the CO signal was nearly absent, confirming that Cu_6Sn_5 is the catalytically active phase favoring formate. DFT calculations indicated that the formation of Cu_6Sn_5 optimizes the electronic structure of Sn, rendering Sn more positively charged ($Sn^{\delta+}$), thereby lowering the Gibbs free energy barrier for OCHO formation, while simultaneously increasing the barrier for COOH and weakening H binding. As a result, the Cu-doped SnO_2 catalyst after reconstruction achieved $FE_{formate}$ ~92% at –0.9 V (H-cell), maintaining >80% in the range –0.8 to –1.1 V with >90% FE stability for 12 h. In the flow-cell (1 M KOH), the catalyst delivered a high current density of 220 mA cm^{-2} at –1.2 V, sustaining $FE_{formate}$ >92% across –0.6 to –1.0 V, and achieved an energy conversion efficiency (ECE)

View Article Online
DOI: 10.1039/D6NA00155F

>50% at 150 mA cm^{-2}. This indicates that more than half of the input electrical energy was converted into chemical energy stored in formate, a critical threshold for practical application. Moreover, the catalyst maintained stable operation for 14 h at –0.9 V. Overall, whether through stabilizing $Sn^{\delta+}$ on the oxide layer via interface engineering or regenerating $Sn^{\delta+}$ within the alloy lattice through dynamic reconstruction, both studies confirm that the persistent presence of $Sn^{\delta+}$ is the key factor in promoting OCHO formation and enhancing the selectivity toward formate.

In addition to these strategies, another proactive design approach to enhance formate selectivity is the direct tuning of the electronic structure of the Cu–Sn system through alloying. Shan et al. fabricated Cu–Sn thin films with precisely controlled compositions via magnetron sputtering, successfully depositing uniform alloy thin films directly onto carbon paper.[92] Among the compositions, $Cu_{41}Sn_{11}$ (Cu-Sn-3 sample, 20.6 at.% Sn) exhibited the highest FE for HCOOH (74%) at −1.3 V vs. RHE. Experimental characterization and DFT calculations elucidated the mechanism: alloying with Sn downshifted the Cu d-band center, optimizing the adsorption energy of *OCHO while simultaneously destabilizing *H and *COOH intermediates. More importantly, the Gibbs free energy calculations for CO_2-to-HCOOH, CO_2-to-CO, and HER pathways, as shown in Figure 10e-g, reveal a dual effect of the Cu–Sn alloy surface. On the Cu-Sn-3 surface, the energy barrier for *OCHO formation was significantly reduced (0.34 eV) compared with pure Cu (0.9 eV) and pure Sn (1.7 eV), whereas *H and *COOH formation became thermodynamically less favorable. This dual effect efficiently suppressed HER and CO evolution, enhancing the selectivity toward formate.

View Article Online
DOI: 10.1039/D6NA00155F

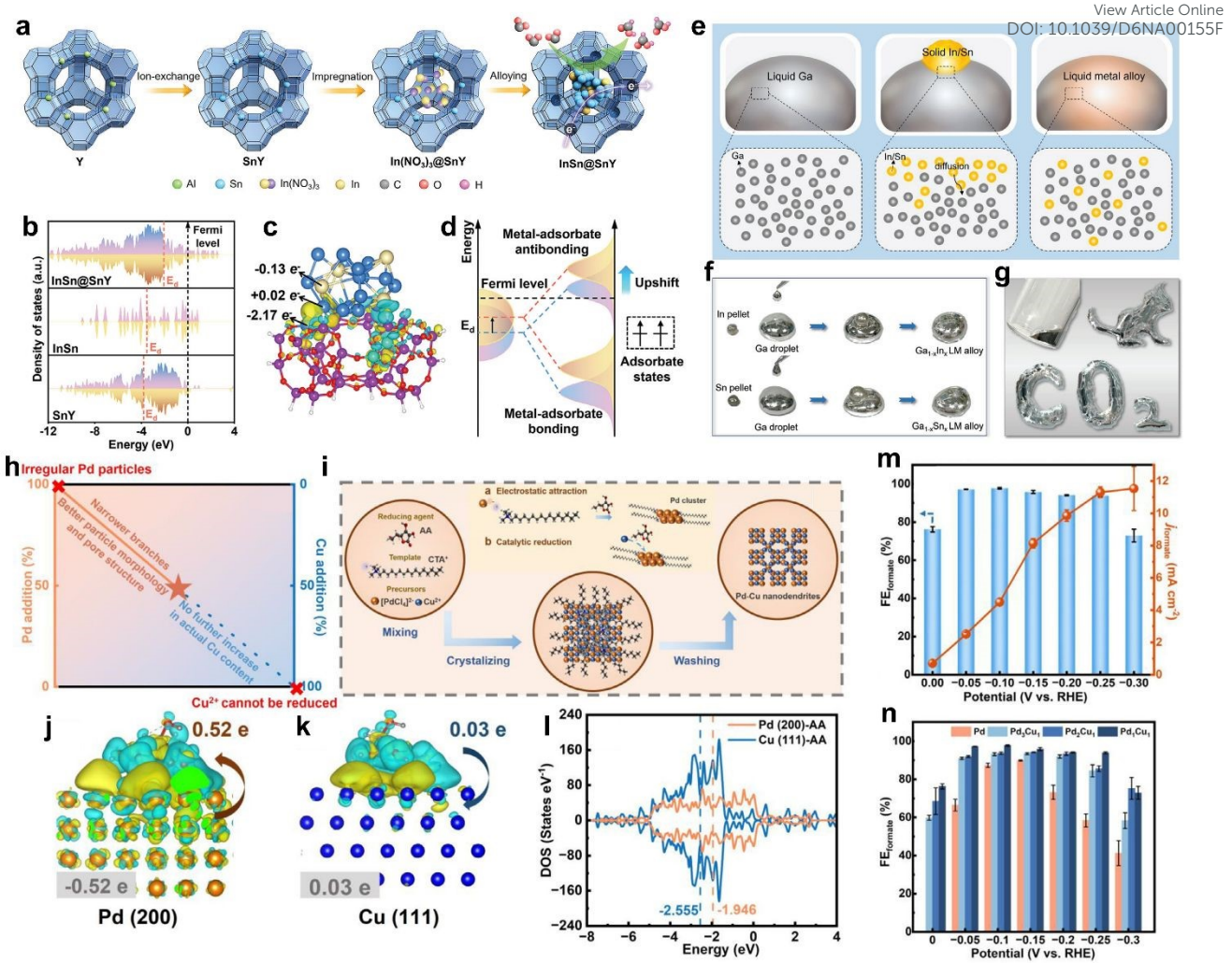

Figure 11. (a-d) Formation and electronic structure of In–Sn nanoclusters confined in conductive SnY zeolite: (a) synthesis steps; (b) DOS; (c) charge redistribution; and (d) schematic of d-band upshift, reproduced from ref [171] with permission from Wiley-VCH GmbH, copyright 2024. (e-g) Structure and preparation of Ga-based liquid metal alloys: (e) liquid-phase alloying process; (f,g) morphology of Ga–In and Ga–Sn droplets, reproduced from ref [172] with permission from Wiley-VCH GmbH, copyright 2024. (h-n) Structure and mechanism of Pd–Cu nanodendrites: (h) morphology evolution with Pd/Cu ratio; (i) schematic of microfluidic synthesis; (j,k) charge distribution; (l) DOS analysis; and (m,n) performance comparison, reproduced from ref [173] under the Creative Commons CC BY 4.0 license.

Indium is also a representative p-block metal with an inherent tendency toward formate production in CO_2RR. When designed as alloys, particularly in combination with Sn, the activity and selectivity of In can be significantly enhanced. However, conventional In–Sn catalysts still suffer from the low conductivity of the support and strong competition from HER. To address this limitation, Zhang et al. developed a novel support-engineering strategy by introducing a conductive zeolite framework to host ultrasmall In–Sn nanoclusters.[171] As illustrated in Figure 11a, Sn atoms were first substituted for Al in the Y zeolite framework through ion exchange, converting the insulating AlY structure into a conductive SnY matrix. Subsequent impregnation of $In(NO_3)_3$ and in-situ alloying within the supercages yielded $In_{0.2}Sn_{0.8}$ nanoclusters (~1.3 nm) uniformly confined inside the zeolite pores. This

View Article Online
DOI: 10.1039/D6NA00155F

confinement effectively prevented particle aggregation and maintained excellent structural stability during electrolysis. Figure 11b presents the calculated DOS, showing that the d-band center of In in InSn@SnY upshift toward the Fermi level relative to pristine InSn, indicating an enhanced electronic coupling between the alloy clusters and the SnY framework. Figure 11c presents the calculated charge density difference map, revealing significant charge redistribution across the In–Sn/SnY interface. Specifically, the adjacent In atom and interfacial Sn atom in the SnY support exhibit electron depletion of –0.13 e^- and –2.17 e^-, respectively. These electrons are donated to the adjacent Sn atom within the alloy, which shows an accumulation of +0.02 e^-. This electron transfer triggers an electronic reconfiguration that upshifts the d-band center, strengthening the metal-adsorbate bonding and facilitating *OCHO intermediate stabilization (as illustrated in Figure 11d). As a result of these synergistic structural and electronic effects, InSn@SnY achieved 98.2% FE for formate, an industrial-level partial current density of 322 mA cm^{-2}, and stable operation for over 102 h-demonstrating that In, when integrated with advanced support design, can serve as an efficient active center for large-scale formate production.

A further step in exploiting the potential of In is the development of SAAs, where individual atoms of a secondary metal are dispersed on the host to maximize atom utilization and precisely tune the electronic structure. Fang et al. reported an Ag_1In system stabilized by an oxygen-pinning (Op) mechanism for formate production.[174] In this system, isolated Ag atoms are anchored by O on the In host, forming covalent bonds that prevent aggregation and maintain structural stability. Mechanistically, Ag atoms act as electronic modulators, altering the local electronic structure of In. In-situ ATR-SEIRAS, EIS, and DFT calculations demonstrated that this adjustment enables Op-Ag_1In to simultaneously (i) enhance CO_2 adsorption/activation and (ii) accelerate water dissociation to provide H, thereby facilitating OCHO formation. Consequently, the catalyst achieved ~92% FE with a partial current density of 13 mA cm^{-2} at −0.95 V, 2.23 times higher than pure In. In the flow-cell, Op-Ag_1In delivered 93.5% FE with a stable current density of 70-93 mA cm^{-2} over 24 h. Notably, the oxygen-pinning mechanism not only promoted CO_2RR kinetics but also made HER energetically unfavorable by modulating H adsorption. These studies provide compelling evidence that alloying is a powerful tool for tailoring the electronic structures of p-block metals, thereby enhancing intrinsic activity and selectivity toward formate.

Beyond p-block metals, Pd is also an attractive candidate due to its activity at nearly zero overpotential. However, an intrinsic limitation of Pd is its poor durability, as its surface is easily poisoned by trace amounts of CO generated during the reaction. In a recent study, Huang et al. addressed this challenge by developing Pd–Cu nanodendrites with channel-rich structures.[173] As shown in Figure 11h,i, the formation mechanism involves electrostatic attraction between $[PdCl_4]^{2-}$ and CTAC to generate Pd-CTA^+ complexes, which act as nucleation templates for anisotropic growth under mild ascorbic acid (AA) reduction, leading to the formation of channel-rich Pd–Cu alloy nanodendrites (~25 nm) with high electrochemical surface area (~97.4 m^2 g^{-1}, about 10 times that of pure Pd) and a K^+-rich microenvironment that stabilizes *OCHO intermediates and accelerates CO_2 reduction kinetics. Charge-density difference mapping Figure 11j,k demonstrates substantial electron transfer from the Pd(200) plane to the adsorbed AA molecule. In contrast, Cu(111) surfaces exhibit only minor charge redistribution. This transfer activates the AA reductant, promoting the reduction of Cu^{2+} and driving alloy formation. Corresponding DOS plots Figure 11l reveal that the d-band center of Pd(200) (–1.946 eV) is closer to the Fermi level than that of Cu(111) (–2.555 eV), implying

View Article Online
DOI: 10.1039/D6NA00155F

higher surface reactivity. This electronic modulation also stabilizes *OCHO intermediates, favoring the formate pathway over the competing *COOH and H_2 evolution routes. As a result, the optimized Pd_1Cu_1 nanodendrites exhibit an outstanding FE for formate of 97.7% at −0.1 V vs. RHE, maintaining FE above 90% across a wide potential window (−0.05 to −0.25 V) and reaching a partial current density exceeding 11 mA cm^{-2} (Figure 11m). The comparison in Figure 11n further confirms that the Pd_1Cu_1 composition provides the best balance between formate selectivity and suppression of HER or CO pathways, outperforming Pd, Pd_2Cu_1, and Pd_3Cu_1 variants. The synergistic combination of morphology, electronic d-band tuning, and ion-enriched nanoconfinement creates a robust catalytic environment that maximizes CO_2 reduction efficiency. Consequently, the Pd_1Cu_1 nanodendrites maintain >90% formate selectivity for over 15 h at −0.2 V.

In addition to conventional solid-state nanoalloys, a promising direction is the exploration of liquid metal alloys for catalytic applications. These materials, typically based on gallium (Ga), combine metallic properties with fluidic flexibility and can be synthesized simply at room temperature in an energy-efficient manner. In a study by Huang et al., Ga–In and Ga–Sn liquid metal alloy nanoparticles were successfully prepared by dissolving solid In or Sn into liquid Ga, followed by ultrasonication to form stable nanodroplets (Figure 11e-g).[172] The results showed that these alloys exhibited much higher activity and selectivity for formate compared to the constituent metals. Specifically, $Ga_{0.75}In_{0.25}$ achieved a maximum FE of 82% for formate at –1.05 V, with a partial current density of 55 mA cm^{-2} at –1.17 V, 4 - 6 times higher than Ga nanoparticles or In powder, and maintained ~72% FE over 12 h at –1.05 V. Similarly, the Ga–Sn system demonstrated impressive performance, with $Ga_{0.90}Sn_{0.10}$ reaching 89% FE and 64 mA cm^{-2} at –1.09 V, while sustaining ~80% FE at an industrial-level current density of 300 mA cm^{-2} in a flow cell. Density functional theory calculations revealed that surrounding Ga atoms create a unique electronic and ensemble effect around In or Sn sites, weakening *H and *COOH adsorption (thus suppressing HER and CO pathways), while optimizing OCHO binding, the direct precursor of formate. Consequently, the reaction pathway is strongly directed toward formate production.

In summary, the key to enhancing $HCOOH/HCOO^-$ production lies in stabilizing the OCHO intermediate and suppressing HER/CO through various strategies such as alloying, interface engineering, dynamic reconstruction, SAAs, and liquid metal alloys. This confirms that alloying, particularly with p-block metals, is a powerful tool to tune the electronic structure and opens up industrial prospects for formate production from CO_2.

4.1.3. Methane

CH_4 formation, a deeply reduced product requiring eight electrons, originates from the key *CO intermediate. From *CO, subsequent hydrogenation (addition of a proton-electron pair) can yield two major intermediates: *CHO (C–H bond formation) or *COH (O–H bond formation). This branching point critically determines the downstream reaction pathway. Once *CHO or *COH forms, a sequence of further hydrogenation steps leads to the cleavage of the C–O bond and progressively saturates the carbon with hydrogen, ultimately releasing CH_4 (Figure 7).[70,72,160]

To promote deep hydrogenation toward CH_4, an effective strategy is combining Cu with a metal capable of strong *CO adsorption such as Ni. A representative study by Li et al. fabricated Ni–Cu alloys supported on N-doped carbon nanotubes (NCNTs).[22] The optimized Ni_1Cu_1-NCNT catalyst exhibited a breakthrough performance in CO_2-to-CH_4 conversion, achieving FE of 99.7% at −1.2 V

View Article Online
DOI: 10.1039/D6NA00155F

vs. RHE, among the highest reported for Cu-based alloys. The underlying mechanism was elucidated by both experimental and theoretical approaches. XPS analysis and DFT calculations jointly revealed electron transfer from Cu to Ni within the alloy, shifting the d-band center closer to the Fermi level relative to monometallic Ni-NCNT and Cu-NCNT catalysts. According to d-band theory, this enhanced the binding energies of reaction intermediates on the surface. In situ EC-ATR spectroscopy further confirmed the presence of *COOH and *CHO intermediates, validating that the Ni–Cu alloy created a favorable electronic environment to stabilize key precursors for CH_4 formation.

From a materials design perspective, directing C_1 selectivity (CO, HCOOH, CH_4) in CO_2RR largely depends on the competition between *COOH and *OCHO intermediates. If *COOH is preferentially stabilized, the pathway proceeds via *CO → *CHO, favoring CO production or further deep hydrogenation to CH_4. Conversely, if *OCHO is stabilized, the pathway is directed toward formate.[175] Thus, nanoalloy design strategies focus on tuning electronic and geometric/strain effects to selectively stabilize one of these intermediates, thereby "activating" or "suppressing" the corresponding branch. To demonstrate this principle, a breakthrough study by Go et al. introduced a thermodynamics-based methodology for deliberately controlling and synthesizing distinct phases of Cu–Sn alloys.[176] By adjusting the partial pressure of oxygen (pO_2) during annealing of electrospun polymer nanofibers containing Cu and Sn precursors, they produced a series of catalysts spanning mixed oxides (CuO–SnO_2), oxide-metal composites (Cu–SnO_2), and ordered intermetallic compounds on carbon nanofibers (CNFs), including $Cu_{41}Sn_{11}$/CNFs, Cu_3Sn/CNFs, and Cu_6Sn_5/CNFs. This study demonstrated that phase control effectively dictates product selectivity in CO_2RR. Specifically, CuO–SnO_2 favored formate, while Cu–SnO_2 exhibited high CO selectivity. Remarkably, intermetallic phases showed distinct product branching: Cu-rich alloys such as $Cu_{41}Sn_{11}$ and Cu_3Sn significantly enhanced CH_4 formation, with $Cu_{41}Sn_{11}$ achieving a maximum FE of 39.1%. In contrast, Sn-rich Cu_6Sn_5 preferentially produced formate with FE of 58.6%. DFT calculations clarified the mechanism, showing that the Cu-rich surface of $Cu_{41}Sn_{11}$ favored the *CO pathway, while Cu_6Sn_5 surfaces stabilized the *HCOOH intermediate.

View Article Online
DOI: 10.1039/D6NA00155F

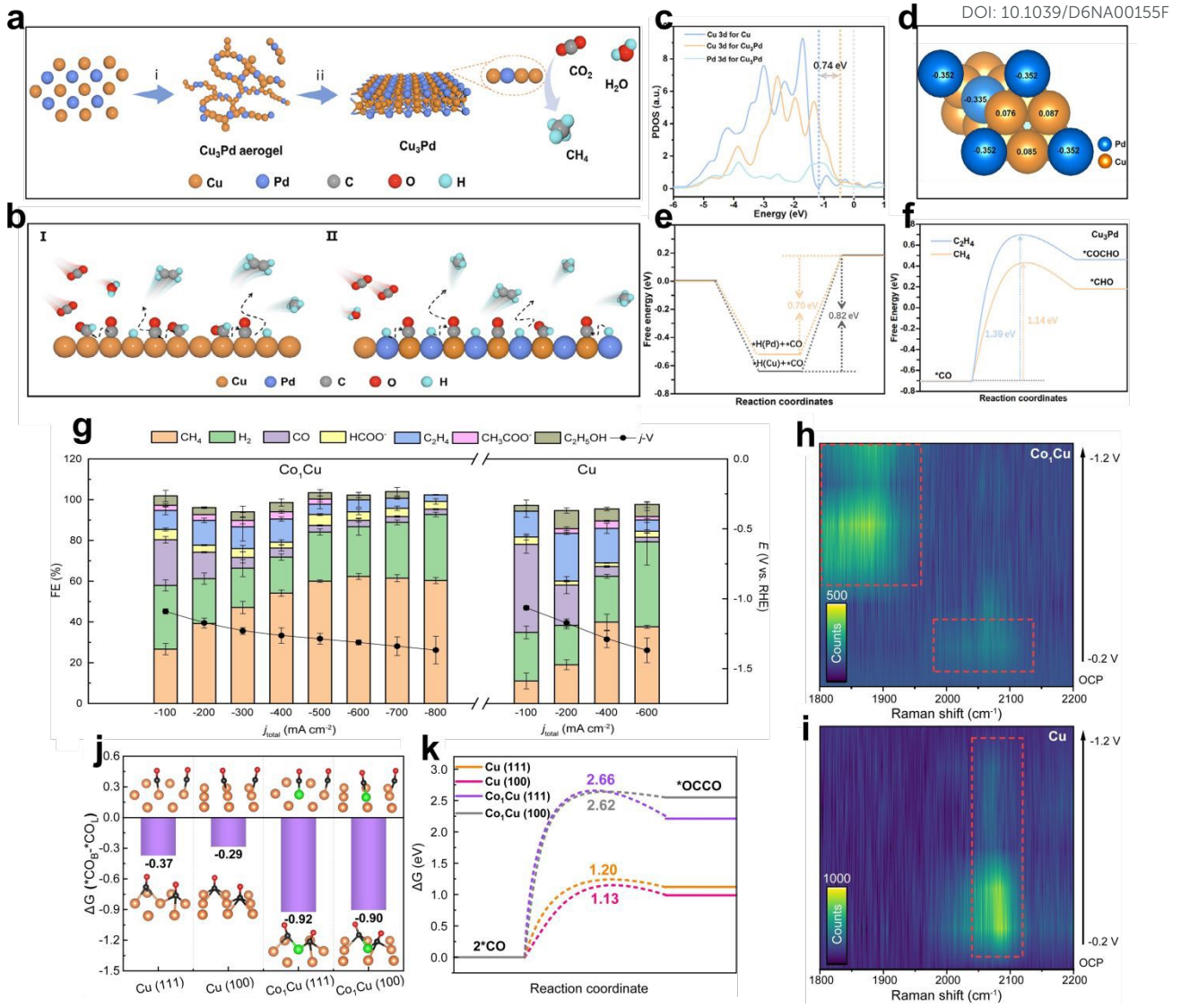

Figure 12. (a) Formation process and structure of Cu–Pd aerogel alloys; (b) reaction schematic comparing CO_2 reduction and hydrogenation pathways on Cu and Cu–Pd surfaces; (c) PDOS showing electronic modulation after Pd incorporation; (d) charge distribution map illustrating electron transfer between Cu and Pd atoms; (e,f) free-energy profiles comparing *CO hydrogenation and *CO–*CHO coupling steps on Cu and Cu_3Pd, reproduced from ref [177] under the Creative Commons CC BY license(g) Product distribution and FE of Co_1Cu and Cu catalysts; (h,i) in situ Raman spectra showing CO adsorption configurations on Co_1Cu and Cu; (j,k) DFT analyses of *CO adsorption modes and reaction energy barriers on Co_1Cu surfaces, reproduced from ref [178] with permission from Wiley-VCH GmbH, copyright 2025.

Among bimetallic systems, Cu–Pd alloys have recently demonstrated remarkable methane selectivity by tuning both geometric and electronic interactions between Cu and Pd sites. Huang et al. reported that introducing Pd into Cu significantly altered the CO_2RR pathway, suppressing C_2H_4 formation while promoting CH_4 evolution.[177] Figure 12a outlines the synthesis and structure of the Cu_3Pd aerogel, where Pd atoms are homogeneously incorporated into a Cu network to form an ordered fcc-type alloy. The underlying mechanism of Pd-induced methane selectivity is systematically illustrated in Figure 12b. Pure Cu typically facilitates C–C coupling between adjacent *CO and *CHO

View Article Online
DOI: 10.1039/D6NA00155F

intermediates, leading to C_2 products such as ethylene. However, in Cu–Pd alloys, Pd atoms act as spatial separators between Cu sites-introducing a blocking effect that hinders *C–C coupling and instead enhances *C–H hydrogenation pathways. Operando ATR-SEIRAS analysis revealed strong vibrational features corresponding to *COOH, *CHO, and *OCH_3 species without detectable *C–C coupling intermediates, confirming that hydrogenation dominates on Cu–Pd surfaces. Electronic-structure analyses support these observations. PDOS calculations in Figure 12c show that alloying with Pd shifts the Cu 3d band center closer to the Fermi level by ≈ 0.74 eV, enhancing electron density and binding strength of adsorbates. Bader charge analysis reveals electron transfer from Cu to Pd, confirming that Pd becomes more electronegative and preferentially adsorbs H^+, forming reactive *H species that mediate proton-coupled *CO hydrogenation (Figure 12d). DFT calculations further demonstrated that *H species adsorbed on Pd atoms lower the reaction barrier for *CO → *CHO hydrogenation from 0.82 to 0.70 eV (Figure 12e), while the energy barrier for *C–C coupling (*CO + *CHO → *COCHO) increased to 1.39 eV compared to 0.78 eV on pure Cu (Figure 12f). These results quantitatively confirm that the presence of Pd not only modifies the d-band center and charge distribution (Bader analysis shows electron transfer from Cu to Pd, rendering Pd electronegative and favorable for H^+ adsorption) but also geometrically inhibits C–C bond formation. Consequently, the Cu_3Pd catalyst achieved a maximum CH_4 FE of 43.2 % at −1.8 V vs. RHE, with a partial current density of −270 mA cm^{-2}. These findings highlight that Pd-assisted hydrogen transfer (*H spillover) and site-isolation effects can synergistically steer the CO_2RR pathway toward deep C_1 reduction.

Recent progress in atomic-level alloying strategies has demonstrated that isolating heteroatoms within a Cu matrix can break the conventional trade-off between selectivity and current density for CO_2-to-CH_4 conversion. Li et al. developed a single-atom cobalt–copper alloy (Co_1Cu), where individual Co atoms are uniformly dispersed within a metallic Cu host.[178] This design achieved a CH_4 FE exceeding 60% at −800 mA cm^{-2}, with a peak partial current density ($j_{methane}$ = −482.7 mA cm^{-2}), outperforming pure Cu (Figure 12g). EXAFS confirmed the formation of Co–Cu bonds (~2.42 Å) and the absence of Co–Co coordination, indicating the atomic dispersion of Co atoms. Mechanistic analyses revealed that single Co atoms act as H_2O activation centers, promoting local proton generation and accelerating CO hydrogenation without relying on H-spillover mechanisms. Concurrently, in situ Raman spectroscopy (Figure 12h,i) identified a shift in the CO adsorption configuration from *linear (CO_L, ~2080 cm^{-1}) on Cu to *bridge (CO_B, ~1860 cm^{-1}) on Co_1Cu, where stronger multi-site binding favors deeper hydrogenation to CH_4 rather than C–C coupling or CO desorption. Complementary DFT calculations corroborated these findings, showing that on the Co_1Cu (111)/(100) surfaces, *CO_B formation is thermodynamically preferred over *CO_L formation (Figure 12j), and the barrier for *CO to *COH hydrogenation decreases. Moreover, the kinetic barrier for *CO–*CO dimerization (C_{2+} formation) increases substantially (Figure 12k), rationalizing the exceptional CH_4 selectivity.

In addition to conventional alloying, mixed-valence modulation on copper surfaces has recently emerged as a powerful means to control CO_2RR product branching. Sun et al.[179] constructed an Ag@Cu_2O@Cu-BDC double-shell tandem catalyst featuring a Cu^{2+}/Cu^+ valence-state fluctuation buffer zone, which dynamically balanced hydrogenation and C–C coupling pathways. The Ag core produced CO intermediates, which migrated to the Cu^{2+}/Cu^+ interface for further reduction. By tuning the Cu^{2+}/Cu^+ ratio (2.46 → 1.28), product selectivity was switched from CH_4 (59.3 %) to C_2H_4 (43.0 %). In situ ATR-SEIRAS and DFT analysis revealed that Cu^{2+} sites facilitate *CO → *CHO

View Article Online
DOI: 10.1039/D6NA00155F

hydrogenation, whereas Cu^+ sites promote *CO–*CHO coupling to OCCHO, confirming their complementary roles in steering reaction pathways. Mechanistically, CO molecules generated on the Ag core diffuse outward to the Cu_2O/Cu-BDC interface, where they undergo selective conversion depending on the Cu oxidation state. Cu^{2+}-rich domains favor methane production, whereas Cu^+-dominated sites stabilize C–C coupling for ethylene formation. The Cu-BDC shell functioned as a "valence-state buffer," preventing Cu^+ reduction and maintaining catalytic stability for >20 h under continuous electrolysis. This study provides a model for alloy-like electronic regulation via oxidation-state engineering, bridging the concepts of bimetallic synergy and dynamic valence tuning in Cu-based CO_2RR systems.

In summary, achieving high CH_4 selectivity in CO_2RR requires promoting deep hydrogenation while suppressing C–C coupling. The strategies highlighted demonstrate several key approaches, ranging from electronic/valence engineering to optimize intermediate binding, to geometric/adsorption control to block dimerization or favor hydrogenation-prone *CO adsorption. Furthermore, proton kinetic enhancement is employed via *H spillover or direct H_2O activation. The most effective systems synergistically lower the hydrogenation barrier while raising the C–C coupling barrier, thereby funneling the *CO intermediate toward CH_4.

4.1.4. Methanol

Methanol is a vital platform chemical and a high-energy-density liquid fuel. The mechanism of methanol electrosynthesis shares its initial pathways with methane production via the key *CO intermediate. Following the reduction of CO_2 to *CO, subsequent hydrogenation yields intermediates such as *CHO or *COH (Figure 7). To selectively drive the pathway toward methanol, the *CHO intermediate must undergo further proton-coupled electron transfers to form $*CH_2O$, followed by $*CH_3O$ or $*CH_2OH$.[70,160,180] The critical determinant in this process is the successful hydrogenation of these intermediates while strictly preserving the C–O bond. Achieving high selectivity for methanol remains exceptionally challenging due to a severe microkinetic hurdle. The fierce competition between CH_3OH and CH_4 originates at the critical branching point of the *CHOH intermediate: while protonation at the carbon atom (which requires surface-adsorbed hydrogen) preserves the C–O bond to yield CH_3OH, the attack by electrolyte protons on the oxygen atom directly cleaves the C–O bond, releasing H_2O and diverting the pathway toward deep reduction to CH_4.[181]

To steer the reaction pathway at this critical juncture, researchers have widely employed nanoalloy catalysts to precisely modulate the local electronic microenvironment. These multimetallic systems leverage synergistic interactions to selectively stabilize oxygenated intermediates, thereby promoting the facile desorption of methanol while effectively suppressing C–O bond cleavage. For instance, phase-separated bimetallic systems have demonstrated remarkable synergistic effects. Lu et al. synthesized three-dimensional Pd-Cu bimetallic aerogels comprising crystallized fcc Pd and amorphous Cu domains.[182] The strong interfacial synergy between these phases, characterized by favorable valence state distributions, effectively stabilized the key $*CO_2^{\bullet-}$ intermediates, enabling the optimal $Pd_{83}Cu_{17}$ aerogel to achieve a methanol FE of 80.0%. Similarly, highly ordered intermetallic nanoalloys show great promise. Payra et al. developed carbon-supported mixed-phase Pt_xZn ($1 < x < 3$) nanoalloys that significantly outperformed their phase-pure counterparts (methanol FE of 81.4%).[183] The heterojunction interfaces facilitated single-electron transfer to activate CO_2, while the specific electronic structure weakened the binding of the $*OCH_3$ intermediate, promoting its prompt

View Article Online
DOI: 10.1039/D6NA00155F

desorption to selectively yield methanol. Furthermore, doping offers a powerful avenue for electronic modulation. By introducing 3% Sn into In_2S_3 microflowers, Bhattacharya et al. induced electron transfer from Sn to In.[184] This created an electron-rich surface that stabilized *CH_2OH intermediates and strongly suppressed HER, representing a significant advance for Indium-based catalysts in alcohol production.

Complementing experimental efforts, integrating DFT with machine learning (ML) has accelerated the rational design of selective nanoalloys across vast compositional spaces. ML frameworks have identified key descriptors, such as Bader charge, metal-ligand bond length, and d-band center, that govern the competition between methanol and methane pathways. For example, data-driven screening revealed that low-concentration Rh-doped Cu alloys induce a 0.18 eV upward shift of the d-band center, strengthening *CHO adsorption and mitigating HER. Extending this approach to highly complex systems, high-throughput screening of 36750 Cu-Co-Ni-Zn-Sn HEA combinations pinpointed 35 highly selective microstructures. In these computationally optimized nanoalloys, synergistic electronic effects favorably route the reaction through the *HCO intermediate rather than *COH, effectively enhancing methanol selectivity while suppressing unwanted C–C coupling and C–O bond cleavage.

4.1.5. Formaldehyde

In the context of CO_2RR, formaldehyde typically emerges as a transient intermediate within the reaction cascades directed toward methanol or methane rather than a terminal product.[160] The predominant mechanistic pathway involves the hydrogenation of *CO to *CHO, followed by the addition of another proton-electron pair to yield *CH_2O.[160,180,181] The primary bottleneck in the selective synthesis of formaldehyde lies in its exceedingly high intrinsic reactivity. HCHO is notoriously difficult to stabilize as a free product; it typically binds strongly to the catalyst surface and undergoes immediate, deep reduction to CH_3OH or CH_4. Consequently, formaldehyde is largely observed only in trace amounts across most CO_2RR systems, making its effective isolation and accurate quantification a formidable challenge.[185] For this reason, steering the reaction to terminate at formaldehyde remains thermodynamically and kinetically disfavored, explaining the current absence of nanoalloys targeting HCHO. Future breakthroughs to rescue formaldehyde from deep reduction may rely on decoupling intermediate adsorption energies via SAAs to disrupt contiguous active sites, tailoring hydrophobic microenvironments to accelerate HCHO desorption, or employing pulsed electrolysis for precise kinetic control.

4.2. C_2 Products

C_{2+} products, encompassing hydrocarbons like ethylene and highly valuable oxygenates such as ethanol and acetic acid, possess significantly higher commercial value and energy density, but their formation pathways are considerably more complex. While the critical rate-limiting step remains the initial C–C coupling, which requires catalysts capable of retaining *CO intermediates to facilitate dimerization without causing surface poisoning, overall selectivity is further governed by the downstream branching of these coupled intermediates. Accordingly, nanoalloy strategies, through electronic effects, ensemble effects, and tandem catalysis, are considered key not only to optimizing the initial C–C coupling but also to dictating the structural evolution of post-coupling intermediates, thereby enabling high selectivity and advancing practical applications.

View Article Online
DOI: 10.1039/D6NA00155F

4.2.1. Ethylene

Among the C_{2+} products of CO_2RR, C_2H_4 is considered the most important owing to its high commercial value and role as an industrial platform chemical. C_2H_4 formation requires a key C–C coupling step, in which *CO acts as the central precursor. However, this pathway directly competes with *CO hydrogenation toward C_1 products such as CH_4. Therefore, maintaining a sufficiently high *CO surface coverage is a prerequisite for enabling C–C coupling, as it increases the probability of two *CO species encountering and reacting. The initial coupling mechanisms are typically proposed as symmetric dimerization (*CO–*CO → *COCO) or asymmetric pathways such as *CO–*COH or *CO–*CHO (yielding *COCOH or *COCHO). Once C_2 intermediates are formed, they undergo successive hydrogenation and dehydration steps, with C–O bond cleavage often steering the pathway toward dehydration and ethylene formation (Figure 7).[70,72,160] Consequently, the ability to control *CO accumulation and reaction branching at this stage is considered decisive for achieving high C_2H_4 selectivity.

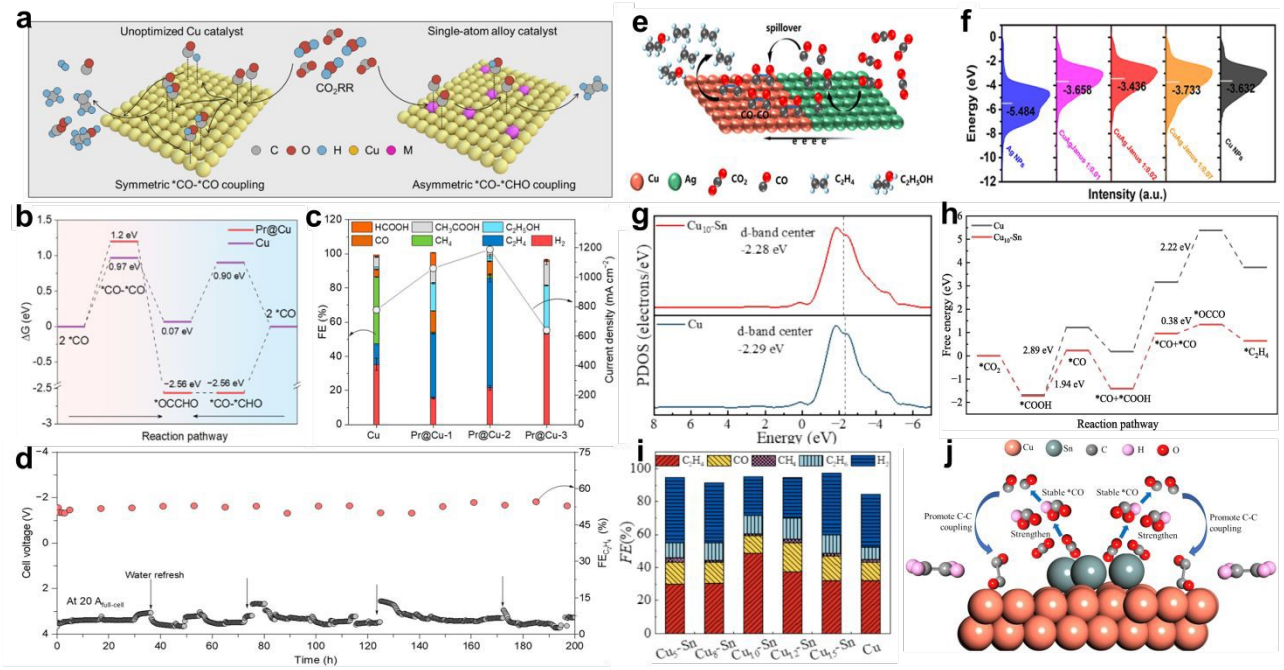

Figure 13. (a) Schematic comparison between Cu catalyst (symmetric CO–CO coupling) and Pr@Cu single-atom alloy (asymmetric CO–CHO coupling); (b) free-energy profiles showing lower activation barrier for CO–CHO coupling on Pr@Cu; (c) product distribution and current density for Cu and Pr@Cu catalysts with different Pr loadings; (d) long-term stability test in MEA, reproduced from ref [186] with permission from American Chemical Society, copyright 2025. (e) Tandem mechanism on Cu–Ag Janus heterostructure; (f) DOS plots of Ag, Cu, and Cu–Ag Janus structures, showing d-band modulation with different Ag/Cu ratios, reproduced from ref [187] with permission from American Chemical Society, copyright 2025. (g) PDOS comparison of Cu and $Cu_{10}Sn$; (h) free-energy diagram illustrating reduced barriers for CO formation and CO–CO coupling on Cu–Sn; (i) FE of Cu–Sn catalysts with different ratios; (j) schematic of cooperative Cu–Sn interface, reproduced from ref [188] with permission from Elsevier Inc, copyright 2024.

One core strategy for enhancing ethylene production is steering the asymmetric *CO–*CHO coupling pathway, which has a lower energy barrier than *CO–*CO dimerization. Xiao et al. realized this

View Article Online
DOI: 10.1039/D6NA00155F

approach by designing a single-atom alloy in which Pr atoms were embedded in a Cu matrix (Pr@Cu).[186] As illustrated in Figure 13a, the unoptimized Cu catalyst typically drives symmetric *CO–*CO coupling, whereas the introduction of isolated Pr atoms on Cu induces an *asymmetric CO–CHO coupling configuration. With their strong oxygen affinity, Pr atoms played a dual role: enhancing CO_2 activation and promoting H_2O dissociation to supply local protons, thereby enriching *CHO intermediates and favoring *CO–*CHO coupling. The corresponding free-energy diagram (Figure 13b) reveals that Pr incorporation substantially lowers the activation barrier for *CO–*CHO coupling, from 1.2 eV on pure Cu to 0.07 eV on Pr@Cu, demonstrating the kinetic advantage of asymmetric coupling over conventional *CO–*CO dimerization. As a result, Pr@Cu achieved FE(C_2H_4) of 64.2% at 1200 mA cm^{-2} in a flow cell (Figure 13c), and when integrated into a 100 cm^2 MEA, the system remained stable for 200 h at 20 A (Figure 13d), demonstrating industrial-scale potential.

Heterostructured catalysts, particularly Janus architectures, have shown remarkable effectiveness in maximizing tandem synergy through precise spatial arrangement. Zhang et al. synthesized Janus Cu–Ag structures that exhibited superior CO_2RR performance toward C_{2+} products.[187] In this system, the Ag phase, with weak *CO affinity, acted as the site for CO_2-to-CO conversion, after which *CO "spilled over" to the adjacent Cu phase for C–C coupling (Figure 13e). Owing to this mechanism, Cu–Ag Janus achieved FE(C_{2+}) up to 69.8%, with FE(C_2H_4) of ~50% and a C_{2+}/C_1 ratio 9.2 times higher than pure Cu. In situ ATR-FTIR confirmed the formation of *CHO and *COCHO intermediates, and the electronic structure analysis in (Figure 13f) further highlights the influence of interfacial coupling on the catalytic properties. The density-of-states distributions show that the d-band center is significantly modulated by the Ag doping. Notably, the optimized CuAg Janus 1:0.02 catalyst possesses the highest (most upshifted) d-band center (–3.436 eV), which is significantly higher than that of pure Cu NPs and the other CuAg Janus ratios. This electronic adjustment optimizes the adsorption of key intermediates, thereby favoring C–C bond formation at the heterointerface. Sharing a similar robust design principle, Zheng et al. constructed well-defined Au-Cu Janus nanostructures via a seeded growth strategy.[189] Analogous to the Ag-Cu system, the Au domains act as efficient CO factories, enabling direct CO spillover to the intimately connected Cu counterparts. Both experimental verifications and theoretical simulations revealed that this spatial configuration substantially enhances the local *CO coverage on the Cu surfaces, thereby lowering the energy barrier for C-C coupling and driving deep reduction to yield a remarkable C_{2+} FE of 67%. Together, these studies powerfully highlight that Janus architectures, whether utilizing Ag or Au as the CO, generating phase-offer a highly versatile and universal platform for optimizing multi-step reaction pathways via tandem catalysis.

Beyond noble metals, alloying Cu with p-block metals has emerged as an effective strategy for tuning C_{2+} selectivity. Although Sn is typically associated with C_1 products, Wang et al. demonstrated that incorporating Sn into Cu significantly promoted ethylene formation.[188] DFT calculations revealed that Sn incorporation induces electron withdrawal from Cu, as evidenced by the PDOS analysis in Figure 13g. The Cu d-band center shifts slightly upward from –2.29 eV to –2.28 eV upon Sn addition, indicating a redistribution of electronic density in which Sn partially extracts electrons from Cu. This electronic adjustment enhances orbital overlap between Cu and the adsorbed CO species, facilitating stronger intermediate stabilization. The resulting increase in stable *CO coverage lowered the C–C coupling barrier (*CO + *CO → *OCCO) from 2.22 eV to only 0.38 eV, while also facilitating C_2H_4

View Article Online
DOI: 10.1039/D6NA00155F

desorption (Figure 13h). Consequently, the Cu–Sn alloy achieved FE(C_2H_4) of 48.74%, representing a 55% improvement over pure Cu (Figure 13i). The reaction mechanism, as depicted in Figure 13j, involves Sn sites acting as electron-withdrawing centers that stabilize CO intermediates, whereas adjacent Cu atoms serve as active sites for CO–CO coupling. This synergistic interaction facilitates C–C bond formation and directs the reaction toward selective C_2H_4 generation.

A compelling demonstration of integrating multiple design strategies is the hollow nanocavity CuPd SAA reported by Zhang et al.[190] This catalyst leveraged both geometric and electronic effects to optimize ethylene production. Geometrically, the nanocavity confinement effect enriched local CO concentration and preferentially stabilized linear *CO (active for C–C coupling) over less active bridge *CO. Electronically, isolated Pd atoms acted as electron sinks, generating $Cu^{\delta+}$ sites that reduced the C–C coupling barrier, as confirmed by DFT. Together, these effects enabled CuPd SAA to reach FE(C_2H_4) = 75.6% and FE(C_{2+} total = 85.7%) at −0.7 V vs. RHE, with a C_{2+}/C_1 ratio 6.5× higher than porous Cu and 12× higher than Cu_2O, while maintaining stability for 20 h of continuous electrolysis.

Advanced surface treatments provide another means of engineering complex active sites. Wang et al. applied H_2 cold plasma treatment to create Cu–Co catalysts with multiple coexisting sites, including Cu^0, Co^0, Cu^{2+}, and Co^{2+}.[191] In this tandem mechanism, metallic Co primarily facilitated CO_2-to-CO conversion, after which *CO spilled over to neighboring Cu^{2+} sites for efficient C–C coupling into C_2H_4. Owing to this synergy, the optimized Cu_2Co_1 catalyst achieved FE(C_2H_4) of 70% and remained stable for 200 h.

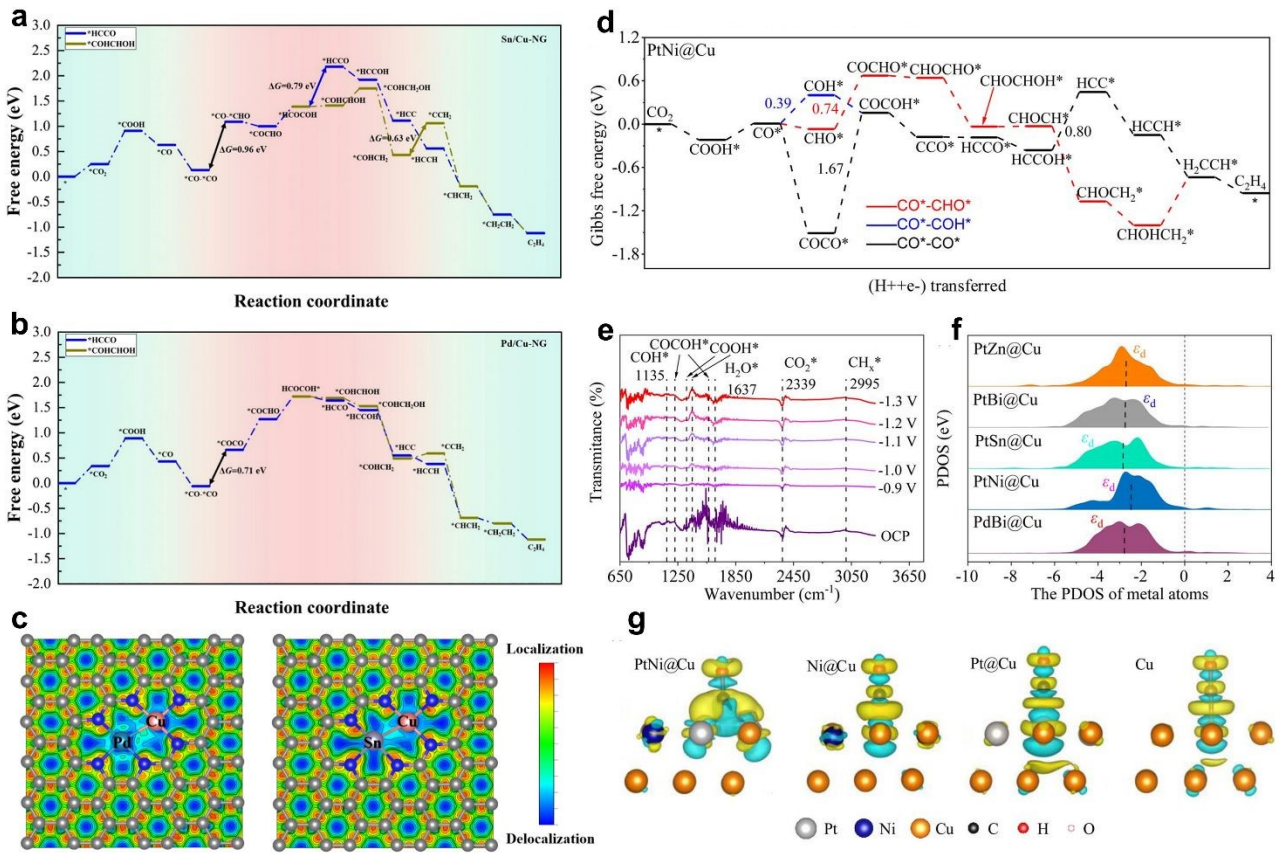

View Article Online
DOI: 10.1039/D6NA00155F

Figure 14. (a) Free-energy diagrams for CO_2 reduction on Sn/Cu–NG and (b) on Pd/Cu–NG. (c) electron localization function maps of Pd/Cu–NG and Sn/Cu–NG, reproduced from ref [192] with permission from American Chemical Society, copyright 2025. (d) Reaction free-energy profile of PtNi@Cu; (e) in situ FTIR spectra of PtNi@Cu; (f) PDOS plots showing d-band modulation among ternary systems; and (g) charge-density difference maps visualizing electron redistribution and cooperative interaction between Pt, Ni, and Cu atoms, reproduced from ref [193] with permission from Royal Society of Chemistry, copyright 2025.

In addition to experimental advances, theoretical approaches play a vital role in catalyst screening. Wang et al. used DFT to investigate diatomic M/Cu-NG systems (M = Zn, Pd, Sn, Ag, Au) for CO_2-to-ethylene conversion.[192] The screening identified Sn/Cu-NG and Pd/Cu-NG as the most promising, with distinct coupling mechanisms. On Sn/Cu–NG, the reduction proceeds primarily through an asymmetric CO–CHO coupling route, ultimately favoring the COHCHOH intermediate pathway. However, this catalyst faces a high potential-determining step with $\Delta G = 0.96$ eV, which corresponds to the hydrogenation of *CO to *CHO (Figure 14a). In contrast, Pd/Cu-NG follows a symmetric CO–CO coupling mechanism, leading to the formation of *COCO intermediates. The potential-determining step is this C–C coupling, which has a significantly lower energy barrier of $\Delta G = 0.71$ eV (Figure 14b). These results suggested Pd/Cu-NG as the more efficient ethylene catalyst, with a lower limiting potential. The electron localization function (ELF) maps in Figure 14c clearly visualize the charge distribution around the active dual-metal sites. The analysis indicates that Pd/Cu-NG exhibits stronger localized electronic states than Sn/Cu-NG. This strong localization facilitates significant d-orbital hybridization between Pd and Cu, which is beneficial for the C–C coupling process. Conversely, the introduction of Sn makes the electron cloud more delocalized, resulting in weaker orbital hybridization and contributing to its higher C–C coupling barrier.

One major challenge in alloy studies is disentangling compositional effects from morphological influences. To address this, Crandall et al. combined systematic theoretical screening with standardized experimental protocols to explore dilute Cu alloys.[194] DFT was first used to evaluate dopants (Al, B, Ga, Sc, Au, Pd) that could lower the *CO dimerization barrier-the key step in C_{2+} formation. Subsequently, dilute alloy films (~5 at.%) were fabricated via physical vapor deposition (PVD), ensuring nearly identical morphologies to isolate composition effects. Experiments validated predictions: CuAl, CuB, CuGa, and especially CuSc alloys all showed significantly higher C_{2+}/C_1 ratios than pure Cu, with CuSc delivering the best performance (C_{2+}/C_1 doubled). This increase stemmed from enhanced production of ethylene, ethanol, and propanol rather than dominance of a single product. Notably, scaling to 5 cm^2 and 100 cm^2 MEAs confirmed stable performance, with FE(C_2H_4) >40% at 200 mA cm^{-2} and only slight decline after 4 h.

Extending beyond binary alloys, ternary alloys offer further opportunities to fine-tune active sites but face challenges due to vast compositional space. To address this, Xiao et al. pioneered a rational design methodology integrating DFT-based screening with three criteria: stability (surface formation energy), activity (CO_2 vs. H_2O adsorption), and selectivity (favoring *COOH over *H).[193] This identified PtNi@Cu as a promising ethylene catalyst. Computational screening revealed that among the investigated systems, PtNi@Cu exhibits the lowest energy barrier for the COOH* formation step. Moreover, the subsequent reaction pathway shown in Figure 14d confirms that PtNi@Cu follows the CO*–CHO* and CO*–COH* coupling pathways rather than the conventional CO*–CO* route.

View Article Online
DOI: 10.1039/D6NA00155F

Experimental validation confirmed these theoretical predictions, demonstratingthat PtNi@Cu achieves FE(C_2H_4) of 30.9% at −1.2 V vs. RHE. The in situ FTIR spectra (Figure 14e) further verify the presence of COH* and COCOH* intermediates during electrolysis, supporting the proposed CO*–COH* coupling mechanism. Electronic structure analyses in Figure 14f shows that PtNi@Cu possesses the highest d-band center compared to the other ternary alloys shown. According to the d-band theory, this higher d-band center allows PtNi@Cu to activate the *CO intermediate more efficiently, thereby reducing the Gibbs free energy of CO_2RR. Finally, the charge-density difference maps in Figure 14g visualize pronounced charge delocalization between Pt, Ni, and Cu atoms, confirming the cooperative interaction among the three metals. The synergy among Pt, Ni, and Cu enhanced electronic redistribution, stabilized *COH intermediates, and promoted C–C coupling. The significance of this work lies not only in the ~31% FE achieved but also in the methodological framework it provides, offering a rational "map" for navigating the vast compositional space of ternary alloys-a task nearly impossible through experiments alone.

4.2.2. Ethanol

The production of C_2H_5OH, a deeply reduced product requiring 12 electrons, is regarded as one of the most challenging targets in CO_2RR. Although its pathway originates from the *CO intermediate and involves a C–C coupling step similar to ethylene, the selectivity between the two diverges at subsequent stages. Specifically, after the formation of oxygen-containing C_2 intermediates (e.g., *CH_2CHO), the catalyst may follow two competing routes: (i) deoxygenation via C–O bond cleavage, leading to C_2H_4, or (ii) hydrogenation, preserving the C–O bond to yield ethanol.[70,72,160] An inherent challenge is that the strong stabilization of C_2 intermediates, while necessary for coupling, simultaneously lowers the barrier for deoxygenation. Thus, an effective ethanol-selective catalyst must not only promote C–C coupling but also finely tune proton transfer kinetics in later steps to favor hydrogenation while suppressing deoxygenation.[195]

View Article Online
DOI: 10.1039/D6NA00155F

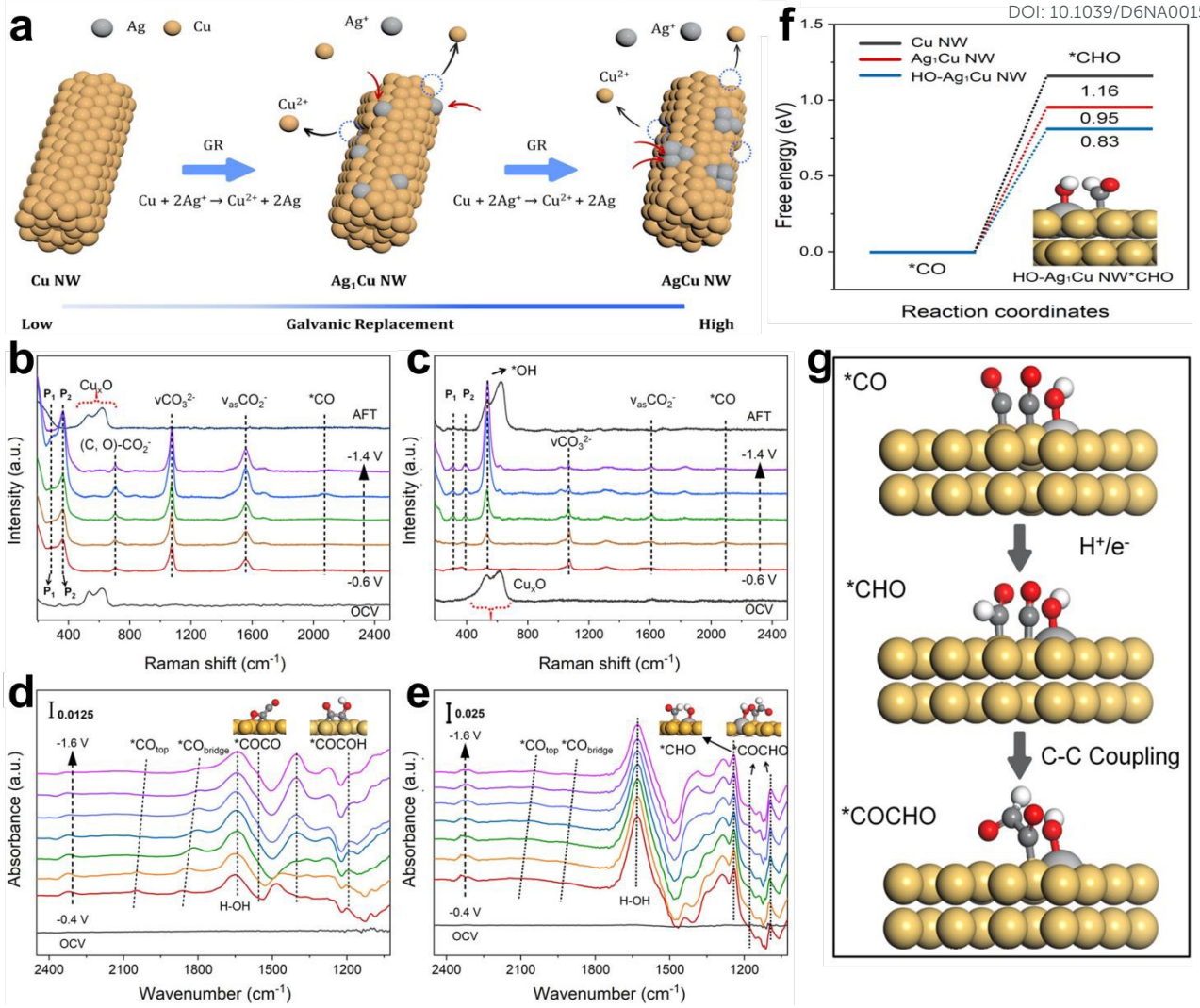

Figure 15. (a) Schematic of catalyst synthesis via galvanic replacement; (b) operando Raman spectra for AgCu NW and (c) Ag_1Cu NW; (d) operando ATR-SEIRAS spectra identifying the *COCO intermediate on AgCu NW and (e) the *CHO and *COCHO intermediates on Ag_1Cu NW; (f) DFT free energy diagram for the *CO to *CHO hydrogenation step, showing a reduced barrier on the HO-Ag_1Cu NW site; and (g) schematics of the proposed asymmetric *CO-*CHO coupling pathway to ethanol, reproduced from ref [196] under CC-BY-NC-ND.

Modern design strategies often focus on creating oxophilic active sites or tailoring the local reaction environment to achieve this.[197] A representative study by Wang et al. demonstrated how atomic-level catalyst engineering can direct C–C coupling pathways in CO_2RR.[196] Using galvanic replacement, they synthesized two model systems: AgCu NW (Ag nanoparticles on Cu nanowires) and Ag_1Cu NW (isolated Ag atoms dispersed on Cu) (Figure 15a). Structural characterization by TEM and HAADF-STEM confirmed their distinct configurations. The two catalysts exhibited markedly different product selectivity: AgCu NW favored C_2H_4 with a maximum FE of 54.9% at 156.0 mA cm^{-2}, while Ag_1Cu NW displayed superior selectivity for ethanol, achieving 56.3% FE at 172.8 mA cm^{-2}. At the core of this study is the elucidation of the mechanism governing product branching, achieved by integrating advanced operando spectroscopic analyses with theoretical calculations. In particular, operando Raman and ATR-SEIRAS measurements (Figure 15b-e) offer direct evidence of the distinct C–C

View Article Online
DOI: 10.1039/D6NA00155F

coupling pathways occurring on two catalyst systems. For AgCu NW, strong *CO-related vibrations at 282, 362, and 1950-2150 cm^{-1} indicate a high *CO coverage that favors *CO–*CO coupling toward ethylene (Figure 15b). Complementary ATR-SEIRAS spectra (Figure 15d) reveal a dominant *COCO band at 1561 cm^{-1}, together with direct detection of the *COCO intermediate, clear evidence that C_2H_4 forms via the symmetric *CO–*CO coupling route. In contrast, Ag_1Cu NW exhibits distinct operando Raman signals of *OH species (~537 cm^{-1}), implying that isolated Ag sites promote H_2O dissociation and generate a proton-rich microenvironment that facilitates *CO hydrogenation to *CHO (Figure 15c). Corresponding ATR-SEIRAS spectra display *CHO (1244 cm^{-1}) and *COCHO (1083 cm^{-1}) bands, confirming the *CO–*CHO coupling pathway responsible for ethanol formation (Figure 15e). The potential-dependent evolution of these bands further supports their mechanistic assignment. DFT calculations (Figure 15f) reveal that the hydrogen-assisted *CO→*CHO step on HO–Ag_1Cu sites possesses the lowest energy barrier (0.83 eV). Consistent with these energetic profiles, the corresponding schematic (Figure 15g) visualizes the asymmetric *CO–*CHO coupling sequence, where *CO and *CHO intermediates couple asymmetrically at paired Cu atoms adjacent to single Ag sites, producing *COCHO and subsequently ethanol. Collectively, these operando and theoretical findings demonstrate how atomic-level catalyst engineering-specifically the introduction of isolated Ag sites-modulates the local reaction environment, lowers the *CO hydrogenation barrier, and steers the C–C coupling pathway from symmetric (*CO–*CO → C_2H_4) to asymmetric (*CO–*CHO → CH_3CH_2OH) routes.

Another breakthrough strategy was introduced by Kim et al., addressing the thermodynamic immiscibility barrier in alloying.[198] Instead of conventional alloying prone to phase segregation, they applied a metallurgical approach by incorporating sacrificial Al into Cu–Ag–Al ternary alloys to form metastable intermetallics, followed by selective leaching of Al. This yielded a supersaturated Ag–Cu solid solution, with Cu clusters uniformly dispersed in ordered Ag lattices-a structure unattainable by standard methods. Operando Raman spectroscopy and DFT calculations revealed that this solid solution generated a high density of step/edge defects, altering *CO adsorption from terrace-preferred LFB atop sites (favoring C_2H_4) to defect-preferred HFB atop sites, increasing *CO binding strength. Consequently, production shifted from ethylene on pure Cu (69.6 ± 1.3% FE) toward ethanol (40.4 ± 2.4% FE) on the supersaturated alloy. The combined effects of Cu–Ag interfacial synergy and defect stabilization lowered the dimerization barrier and stabilized intermediates along the ethanol pathway.

One of the remarkable recent advances in ethanol synthesis at industrially relevant current densities comes from combining intermetallic compounds with facet engineering strategies. In a notable study, Peng et al. successfully synthesized intermetallic Cu_2Mg with preferential exposure of the (111) facet.[199] Ordered Cu_3–Mg sites on this facet were identified as key to ethanol selectivity. Electron transfer from Mg to Cu created electron-rich Cu centers capable of strongly stabilizing the crucial *CHCHOH intermediate, the direct precursor to ethanol, while the competing *CCH intermediate (toward C_2H_4) was energetically unfavorable. As a result, $Cu_2Mg(111)$ achieved a remarkable 76.2% FE for ethanol at 600 mA cm^{-2}, with a partial current density of 720 mA cm^{-2}-among the highest reported.

Beyond metal-metal interactions, advanced catalyst designs integrate additional factors. Guo et al.[200] proposed a dual-modification strategy on Cu–Zn alloys: (1) alloying with Zn to tune Cu's electronic structure, and (2) introducing the organic stabilizer 3,5-diamino-1,2,4-triazole (DAT). Zn

View Article Online
DOI: 10.1039/D6NA00155F

incorporation enhanced FE and partial current density for ethanol by 325% and 600%, respectively, compared to pure Cu. Further addition of DAT boosted them by 194% and 292%, yielding CuZn-DAT with ethanol selectivity up to 87% among C_2 products. Mechanistic studies showed that Zn stabilized *CO and lowered the barrier for C–C coupling while suppressing HER, whereas DAT coordinated with CuZn sites to modulate adsorption of *CO and *CHO, synergistically steering the reaction toward ethanol.

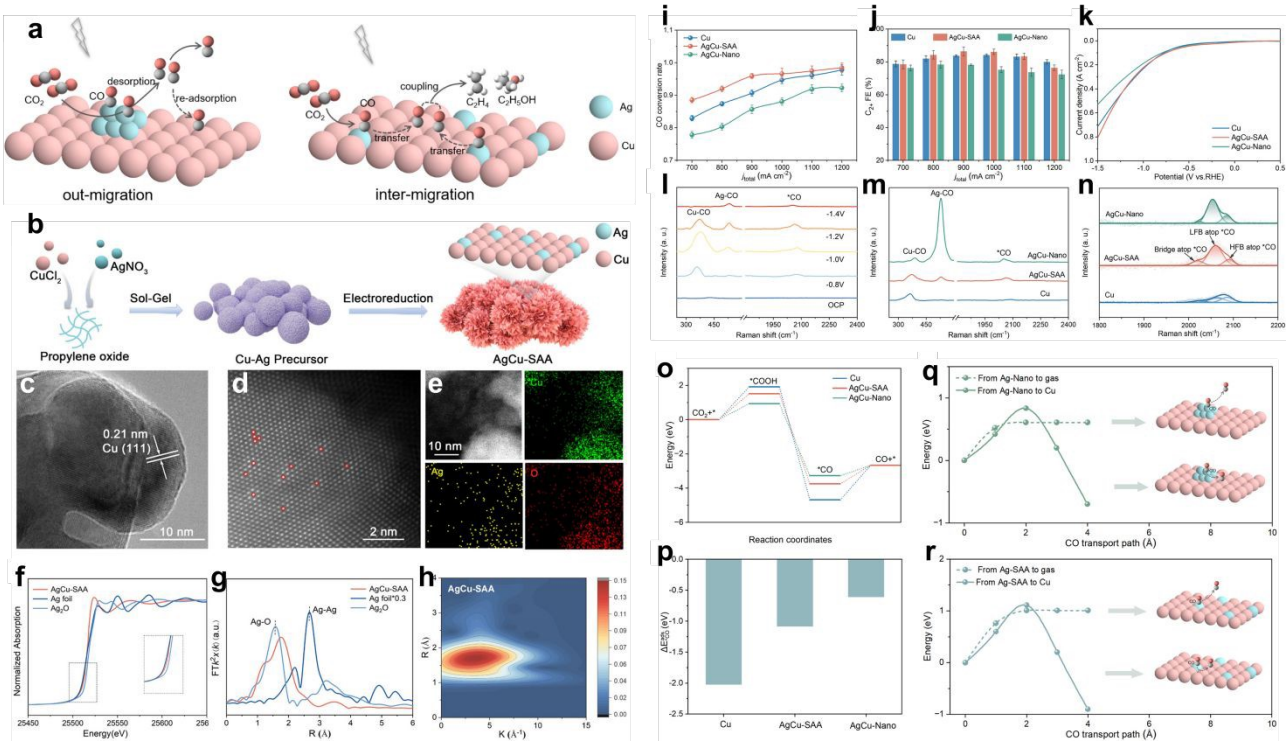

Figure 16. (a) Schematic comparison of out-migration vs. inter-migration modes of CO transfer between Ag and Cu; (b) synthesis route of AgCu-SAA; (c–e) HR-TEM, AC-HAADF-STEM, and EDS mappings confirming atomic dispersion of Ag; (f–h) Ag K-edge XANES spectra, Ag K-edge FT-EXAFS spectra, and Wavelet transform image of the AgCu-SAA; (i–k) CO conversion rate, C_{2+} FE, and LSV curves over Cu, AgCu-SAA, and AgCu-Nano; (l–n) in situ Raman spectra revealing strong bridge and low-frequency atop CO adsorption on AgCu-SAA; (o–p) DFT-computed free-energy diagrams and CO adsorption energies over Cu, AgCu-Nano, and AgCu-SAA; (q–r) calculated energy barriers and pathways for CO transfer from Ag to Cu, reproduced from ref [201] with permission from American Chemical Society, copyright 2025.

The transport of the *CO intermediate has also been revealed as a key factor. Wang et al.[201] conceptually distinguished two migration modes in tandem catalysts (Figure 16a). In conventional "out-migration," CO desorbs from Ag sites into the electrolyte and then re-adsorbs onto Cu, resulting in poor utilization efficiency. In contrast, in "inter-migration," CO transfers directly between adjacent Ag and Cu atoms without leaving the surface. This eliminates interfacial barriers and maintains high CO surface coverage, thereby facilitating efficient C–C coupling. To favor the latter, they designed an AgCu-SAA, where Ag atoms were atomically dispersed in Cu (Figure 16b). This eliminated physical phase boundaries, enabling direct *CO transfer. HR-TEM image, AC-HAADF-STEM image, and EDS element mapping images (Figure 16c-e) confirm the atomic dispersion of Ag on Cu, with no detectable Ag–Ag coordination, while XANES/EXAFS analyses (Figure 16f-h) reveal strong

View Article Online
DOI: 10.1039/D6NA00155F

Ag–Cu interactions and the absence of Ag clusters, supporting the single-atom alloy configuration. The catalytic implications are shown in Figure 16i-k. AgCu-SAA exhibits the highest CO conversion rate and C_{2+} FE among Cu and AgCu-Nano catalysts, achieving 83.4% FE(C_{2+}) at 900 mA cm^{-2}. This superior performance arises from the enhanced CO retention and migration efficiency at atomic Ag–Cu interfaces. Operando Raman spectra (Figure 16l-n) further confirm distinct adsorption modes. Compared with Cu and AgCu-Nano, AgCu-SAA shows stronger bands for bridge and low-frequency atop CO adsorption, indicating greater surface CO coverage and stronger CO–Cu interaction. Calculations reveal that the CO adsorption energy on AgCu-SAA lies between that of Cu and AgCu-Nano, achieving an optimal balance between retention and mobility (Figure 16o,p). Energy-barrier profiles demonstrate that for AgCu-Nano, CO desorption into the electrolyte (out-migration) is thermodynamically preferred, whereas for AgCu-SAA, the barrier for CO transfer from Ag to adjacent Cu sites is comparably low, validating the inter-migration mechanism. The corresponding energy profiles (Figure 16q,r) visualize the facile CO transport along the metal–metal interface, emphasizing that atomic Ag sites act as "relay stations" for CO delivery toward C–C coupling centers. Collectively, these combined operando and computational results reveal that atomic-level Ag–Cu coordination enables direct CO inter-migration, boosting local CO concentration and stabilizing key intermediates for C–C bond formation.

While tandem catalysis remains pivotal, emerging evidence suggests that classical tandem models cannot fully explain selectivity differences between ethylene and ethanol on alloys of similar composition. A deeper mechanism involves dynamic restructuring of Cu under the influence of secondary metals.[202] For example, Au not only provides CO but also acts as a structural modulator, driving Cu into amorphous surface layers enriched in undercoordinated sites during reaction. These dynamic sites, rather than static tandem effects, govern the branching toward more complex products. This paradigm shift-from phase-separated tandem models to dynamic atomic-scale restructuring-offers new directions for tailoring product selectivity. Direct evidence comes from Rollier et al.[203], who investigated Cu–Ag catalysts for CO reduction. They identified $Cu_{0.9}Ag_{0.1}$ as optimal, with C_{2+} selectivity up to 63%, outperforming pure Cu. Operando and in-situ characterization showed that the oxide precursors reconstructed into Ag-core Cu-shell nanoparticles, with WAXS confirming a Cu–Ag alloy phase at the interface. These interfacial sites, featuring strong electronic effects, were pinpointed as the active centers driving enhanced C–C coupling and suppressing HER.

4.2.3. Acetic acid / Acetate

Acetic acid (or acetate) is a high-value C_2 oxygenate, serving as a vital precursor for various polymers and industrial solvents. Its formation is complex and faces intense competition from ethylene and ethanol production, as these products share common initial C_2 C–C coupling intermediates. While acetate can form through specific pathways like the nucleophilic attack of $*CH_3$ species on $*CO_2^{\bullet-}$ [204], it is frequently proposed to originate directly from the ethylene/ethanol pathways. This occurs either via the isomerization of the $*OCH_2COH$ intermediate into a three-membered ring compound followed by further reduction[205], or through the dehydration of (OH)CCOH to form a ketene intermediate (*C=C=O) that converts to acetate at a high local pH[206]. Alternatively, acetate can also be formed via a Cannizzaro-type disproportionation of acetaldehyde under highly alkaline conditions.[204,205] Because acetate synthesis fiercely competes with ethylene and ethanol, achieving high FE on monometallic catalysts remains elusive. Breaking these inherent selectivity trade-offs

View Article Online
DOI: 10.1039/D6NA00155F

requires maintaining a strongly alkaline local environment and high *CO surface coverage. To navigate these complex requirements, researchers have effectively employed spatial decoupling strategies such as tandem catalysis.

A prominent example is the distinct architecture developed by Hu et al., comprising copper nanoparticles encapsulated by single-nickel-atom-modified carbon frameworks (Ni SACs-Cu NPs).[207] In this system, atomically dispersed Ni sites efficiently reduce CO_2 to *CO, generating a localized, high-concentration *CO environment. These intermediates readily migrate to the adjacent Cu(111) facets, thermodynamically circumventing the formate pathway and favoring specific C–C coupling toward acetate. This synergistic tandem strategy achieved an impressive acetate selectivity of over 60% among liquid products at high current densities (50 - 200 mA cm^{-2}). Beyond macro-spatial decoupling, precise atomic engineering within sub-nanometer bimetallic systems has proven highly effective in driving the crucial C–C coupling steps. For instance, an entropy-derived CuPd sub-1nm alloy engineered on CuO/phosphomolybdic acid subnanosheets leverages subnanometer confinement to create fully exposed Cu-Pd pairs.[208] These unique bimetallic sites synergistically enhance *CO surface coverage. Furthermore, in situ Raman spectroscopy and ab initio molecular dynamics revealed that high vibrational entropy induces energetic oscillations within the Cu-Pd pairs, dynamically facilitating the close proximity and subsequent asymmetric C–C coupling of adsorbed *CO and *COH to form the crucial COH–C=O species. This unique subnanoalloy achieved a peak FE of 46.5% for acetate and maintained robust stability over 20 hours.

The importance of tailoring the local electronic environment to lower the energy barriers for such asymmetric coupling is a universal principle that extends to valence-engineered composite systems. Zhang et al. demonstrated that precisely tuning the Cu(II)/Cu(I) ratio optimizes the synergistic interplay between mixed-valence copper sites.[209] This electronic modulation effectively steers the reaction toward asymmetric *CO−COH coupling while suppressing HER, yielding an acetate FE of 35.78%, a mechanistic advantage that strongly parallels the synergistic effects harnessed in bimetallic nanoalloys. Furthermore, isolating secondary metals at the atomic level offers a powerful avenue to steer selectivity. Sun et al. demonstrated the potential of precise bimetallic interface engineering with an atomically dispersed Cu-Au alloy ($CuAu_{1\%}$).[210] The incorporation of isolated Au atoms onto a Cu nanoparticle host creates abundant atomic Cu–Au interfaces that fundamentally alter the geometric and electronic structure. DFT calculations revealed that this atomic dispersion effectively weakens the binding strength of *CO+*CO intermediates, thereby facilitating direct C–C coupling and favorably routing the pathway toward acetate. In an alkaline flow cell, this $CuAu_{1\%}$ nanoalloy achieved a maximum acetate FE of 39% and an outstanding partial current density of 217 mA cm^{-2}, underscoring the efficacy of single-atom alloying for targeted C_{2+} oxygenate synthesis.

In summary, the successful conversion of CO_2 into specific C_2 products highlights the transformative power of nanoalloy engineering in breaking inherent monometallic scaling limitations. By synergistically integrating tandem catalysis, precise electronic modulation, and atomic-level confinement, these advanced multimetallic architectures enable unprecedented control over both the critical C–C coupling step and the subsequent branching pathways toward targeted hydrocarbons and oxygenates.

4.3. Toward C_{3+} Products

View Article Online
DOI: 10.1039/D6NA00155F

The electrochemical production of C_{3+} compounds such as n-propanol is an ambitious goal due to their higher energy density and economic value, and remains the most formidable challenge in CO_2RR, requiring multiple complex coupling steps. Although the precise mechanism is still under debates, recent studies have begun to provide deeper insights.[211] While symmetric *CO–*CO dimerization has long been considered the canonical pathway for C–C bond formation, Zheng et al.[212] reported, through DFT simulations on Pd_3Au alloys, that chain propagation is instead dominated by sequential asymmetric couplings. In this route, C_2 intermediates (*CCH_2, *CCH_3) couple further with C_1 fragments (*CH_x) to yield C_3 products. In particular, the *CCH_2 + *CH_3 step exhibits a relatively low barrier, favoring the formation of propylene and propane. Stable C_3 intermediates can even engage in further coupling with C_1 units to extend into C_4 hydrocarbons. By contrast, oxygenated intermediates such as CO or COH present significantly higher barriers, explaining why Pd_3Au tends to produce hydrocarbons rather than oxygenates.

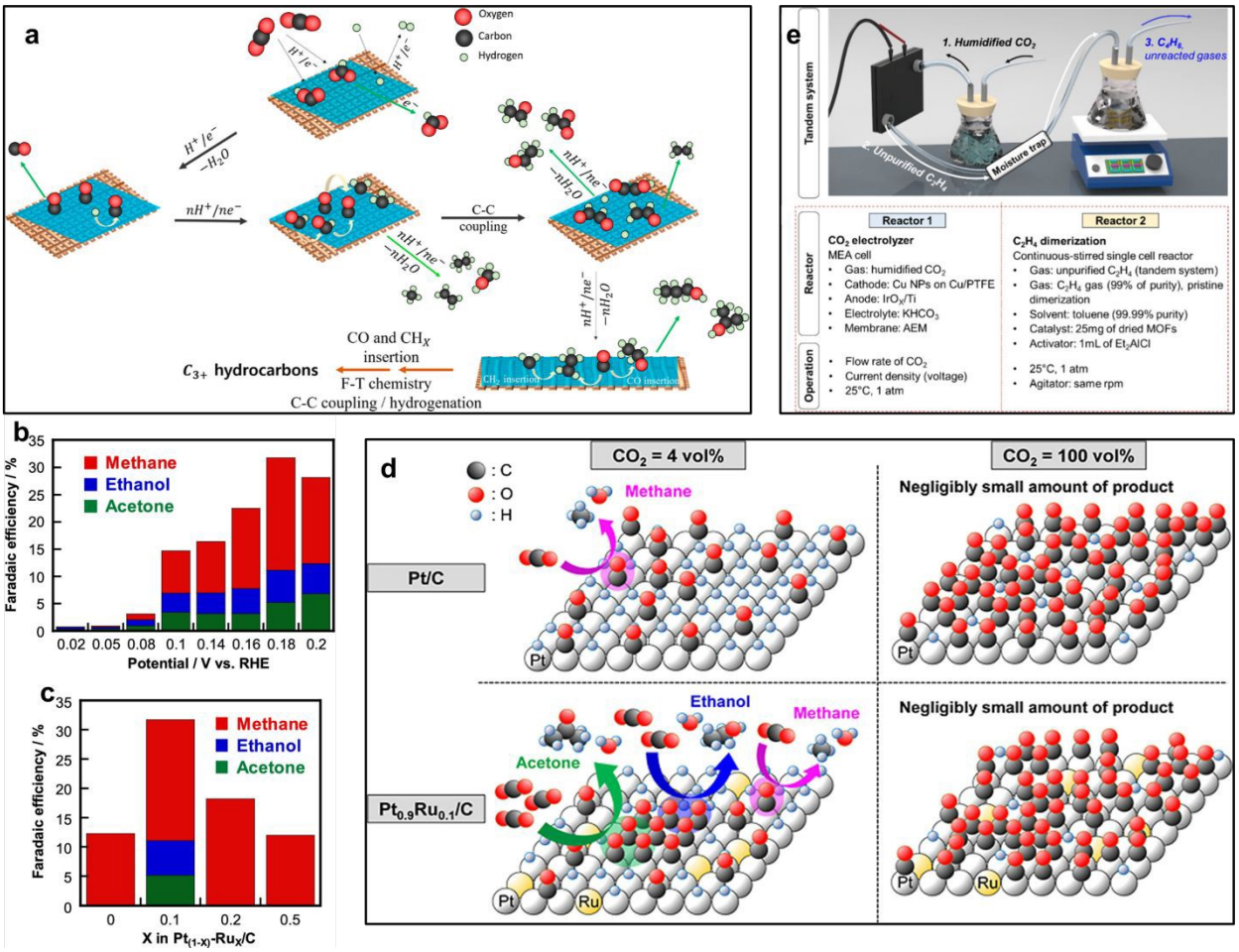

Figure 17. Strategies for CO_2RR toward C_{3+} products. (a) Fischer–Tropsch-like chain growth on Cu–Zn alloys, reproduced from ref [213] with permission from American Chemical Society, copyright 2024. (b,c) Product selectivity and Ru composition effects on $Pt_{1-x}Ru_x/C$; (d) reaction schemes on Pt/C and $Pt_{0.9}Ru_{0.1}/C$, reproduced from ref [214] under the Creative Commons CC-BY 4.0 license. (e) Tandem $CO_2 \rightarrow C_2H_4 \rightarrow C_4H_8$ cascade integrating electrochemical and thermochemical steps, reproduced from ref [215] with permission from American Chemical Society, copyright 2024.

A comprehensive study by Bae et al.[213] on Cu–Zn alloy electrodes demonstrated the formation of a broad spectrum of products, including propanol, isopropanol, and hydrocarbons up to C_4. A key

finding was the resemblance of CO_2RR to the classical Fischer–Tropsch (F–T) synthesis. Using Anderson–Schulz–Flory distribution analysis, the authors found that the production of C_{2+} alkanes and C_{3+} alkenes followed a linear trend, indicating stepwise chain-growth akin to *CO or *CH_x insertion in F–T synthesis. As illustrated in Figure 17a, the process begins with CO_2 adsorption and reduction to *CO intermediates on Cu–Zn alloy surfaces, followed by sequential proton-electron transfers that generate *CH_x species. The coupling between *CO and *CH_x intermediates enables C–C bond formation, leading to the formation of C_2 products. Subsequent chain propagation occurs through repetitive *CH_2 or *CO insertion steps, yielding C_{3+} hydrocarbons such as propanol, isopropanol, and butenes. Interestingly, ethylene deviated from this linearity, suggesting it is produced through a parallel pathway, most likely the well-established *CO–*CO dimerization mechanism. This provides a new perspective in which catalyst design must not only enable initial C–C coupling but also promote Fischer–Tropsch-like chain propagation.

A landmark work by Matsuda et al.[214] demonstrated the production of not only CH_4 and ethanol but also acetone on $Pt_{0.9}Ru_{0.1}$ catalysts. Beyond overcoming Pt's conventional limitation of producing mainly H_2 and suffering from CO poisoning, $Pt_{0.9}Ru_{0.1}$/C in MEA delivered simultaneous C_1-C_3 products with a total FE of 31.7% at an ultralow overpotential of just 0.18 V (Figure 17b). This was the first report of ethanol and acetone generation on Pt–Ru systems. Figure 17c further compares product distributions as a function of Ru content, showing that the composition $Pt_{0.9}Ru_{0.1}$ provides the optimal balance between CO adsorption and hydrogenation activity, leading to the highest overall multicarbon yield. Figure 17d schematically depicts the mechanistic difference between Pt/C and $Pt_{0.9}Ru_{0.1}$/C surfaces under varying CO_2 concentrations. On pure Pt, strong CO binding blocks active sites and limits reduction to methane under low CO_2 availability, while under high CO_2 concentrations the surface becomes poisoned. In contrast, the incorporation of Ru weakens Pt–CO interaction, allowing CO intermediates to accumulate and migrate, facilitating Langmuir–Hinshelwood-type coupling between adjacent CO species. This coupling leads to the formation of C–C bonds and subsequent hydrogenation into ethanol and acetone, marking a distinct pathway beyond methane formation.

A promising approach is tandem cascade systems integrating electrochemical and thermochemical steps. Lee et al.[215] achieved this by producing 1-butene from CO_2. Their setup consisted of two sequential reactors: (i) a high-performance electrolyzer reducing CO_2 to C_2H_4, and (ii) a thermochemical reactor for C_2H_4 dimerization (Figure 17e). The C_2H_4 stream from the first reactor was fed directly, after dehydration, into the second reactor, where a Ru–Ni metal-organic framework catalyzed its conversion to 1-butene with 97% selectivity at 25 °C and 1 atm. Overall, the integrated $CO_2 \rightarrow C_2H_4 \rightarrow C_4H_8$ cascade achieved ~47% selectivity at 156 mA cm^{-2}. Although the second step exhibited near-perfect efficiency, overall performance depended on the cumulative yield of both reactors and transfer losses, underscoring both the promise and the challenge of cascade strategies for accessing C_{3+} products.

Recent advances toward C_{3+} products highlight three complementary strategies: (i) Fischer–Tropsch-like chain growth enabling stepwise *CO/*CH_x insertion, (ii) surface electronic tuning in nanoalloy systems that promotes CO accumulation and C–C coupling, and (iii) tandem cascade systems combining electrochemical and thermochemical stages for selective C_4 formation. Despite these advances, the direct electrochemical synthesis of higher-order products remains fundamentally

View Article Online
DOI: 10.1039/D6NA00155F

constrained by competing pathways, limited intermediate coverage, and the delicate balance between hydrogenation and coupling kinetics. Future progress will depend on multi-site catalyst design that enables both localized intermediate confinement and sequential C–C insertion, possibly through hybrid systems coupling electrocatalysis with chemical upgrading. Achieving such integrated control will be crucial for transforming CO_2RR from C_2-level selectivity to scalable C_{3+} fuel and chemical production.

Finally, to quantitatively benchmark recent progress, Table 5 compares the key electrochemical metrics (FE, current density, applied potential, and durability) of representative nanoalloy systems. This side-by-side comparison reveals that while current designs excel in product selectivity, achieving concurrent high current densities and long-term stability remains the primary challenge for practical CO_2RR deployment.

Table 5. Comparison of CO_2 electroreduction performance across various alloy catalyst systems.

No.	Alloy catalyst system	Main product	FE	Current density	Applied potential	Stability	Ref
1	Cu_3Sb (Intermetallic alloy)	CO	97.9%	41.9 mA cm^{-2}	–0.6 V vs. RHE	> 12 hours	161
2	Cu_1Fe_2/NC (Cu-Fe alloy on N-Carbon)	CO	98.91%		–0.7 V vs. RHE	24 hours	163
3	NP-$Ag_5Cu_5Au_5$ (Nanoporous alloy)	CO	~96%	147 mA cm^{-2} (partial j)	–1.173 V vs. RHE	8 hours	162
4	AgCu nanoalloy	CO	83.2%	7.52 mA cm^{-2} (partial j)	–0.5 V vs. RHE	> 3 hours	90
5	$Cu_{0.07}Zn$ (Nanosheets alloy)	Syngas (CO/H_2)	~100%	20 mA cm^{-2}	–0.95 V vs. RHE	42.2 hours	165
6	Cu-Zn-675 (Bimetallic Cu-Zn)	Syngas (CO/H_2)	~90%	5.98 mA cm^{-2}	–0.81 V vs. RHE	7.5 hours	164
7	InSn@SnY ($In_{0.2}Sn_{0.8}$ alloy on zeolite)	$HCOO^-$/ HCOOH	98.2%	322 mA cm^{-2} (partial j)	–1.33 V vs. RHE	102 hours	171

8	Cu_6Sn_5@SnO_x core-shell	$HCOO^-$/ HCOOH	88.4%	707.2 mA cm^{-2} (partial j)	–1.53 V vs. RHE	>90 hours	169
9	Op-Ag_1In (SAA)	$HCOO^-$/ HCOOH	93.54%	70 mA cm^{-2}	–0.9 V vs. RHE	24 hours	174
10	Pd_1Cu_1 (Nanodendrites alloy)	$HCOO^-$/ HCOOH	>90%	~31.7 mA cm^{-2}	–0.2 V vs. RHE	15 hours	173
11	$Ga_{0.75}In_{0.25}$ LMP (Liquid metal alloy)	$HCOO^-$/ HCOOH	77.1%	150 mA cm^{-2}	–1.05 V vs. RHE	> 12 hours	172
12	$Cu_{41}Sn_{11}$	$HCOO^-$/ HCOOH	74%	~20 mA cm^{-2}	–1.3 V vs. RHE	> 10 hours	92
13	Cu_6Sn_5/CNFs (Sn-rich phase)	$HCOO^-$/ HCOOH	58.6%		–2.31 V vs. RHE		176
14	Ni_1Cu_1-NCNT (Alloy on N-Carbon)	CH_4	99.7%	11.54 mA cm^{-2} (partial j)	–1.2 V vs. RHE	High stability at –1.2 V	22
15	Co_1Cu (Co-Cu SAA)	CH_4	62.3%	482.7 mA cm^{-2} (partial j)	~ –0.85 V vs. RHE	10 hours	178
16	Cu_3Pd (Bimetallic alloy)	CH_4	43.23%	269.68 mA cm^{-2} (partial j)	–1.8 V vs. RHE		177
17	$Cu_{41}Sn_{11}$/CNFs (Cu-Sn phase)	CH_4	39.1%		–1.36 V vs. RHE		176
18	Cu_3Sn/CNFs (Cu-rich phase)	CH_4	34.7%		–1.50 V vs. RHE		176
19	Pt_xZn/C (Intermetallic alloy)	CH_3OH	81.4%		–0.90 V vs. RHE	16 hours	183
20	Sn_2/In_2S_3 (3% Sn)	CH_3OH	31%	7.97 mA cm^{-2} (partial j)	–1.331 V vs. RHE	50 hours	184
21	Pr@Cu-2 (Pr-Cu SAA)	C_2H_4	64.2%	1200 mA cm^{-2}	–1.6 V vs. RHE	> 200 hours	186

22	CuPd SAA (Nanocavity enriched)	C_2H_4	75.6% (C_{2+} 85.7%)		–0.7 V vs. RHE	20 hours	190
23	Cu_2Co_1	C_2H_4	70%	10.2 to 11.7 mA cm^{-2}	–1.0 V vs. RHE	200 hours	191
24	AgCu NW (Bimetallic nanowires)	C_2H_4	54.9%	156.0 mA cm^{-2}	–1.1 V vs. RHE	5 hours	196
25	CuAg Janus 1:0.02	C_2H_4	50% (C_{2+} ~70%)	67.6 mA cm^{-2}	–1.2 V vs. RHE	~ 4 hours	187
26	Cu_{10}-Sn (Cu-Sn nanosheets)	C_2H_4	48.74%	11.99 mA cm^{-2} (partial j)	–1.29 V vs. RHE	> 8 hours	188
27	Au-Cu Janus Nanostructures	C_2H_4 & C_2H_5OH	67%	290 mA cm^{-2} (partial j)	–0.75 V vs. RHE	12 hours	189
28	PtNi@Cu (Ternary alloy)	C_2H_4	30.9%	24.2 mA cm^{-2}	–1.2 V vs. RHE	14 hours	193
29	$Cu_2Mg(111)$	C_2H_5OH	76.2 ± 4.8%	600 mA cm^{-2}	–0.6 V vs. RHE	15 hours	199
30	Ag_1Cu NW (Ag-SAA on Cu nanowire)	C_2H_5OH	56.3%	172.8 mA cm^{-2}	–1.0 V vs. RHE	5 hours at ~ 250 mA cm^{-2}	196
31	CuZn-DAT	C_2H_5OH	19.9%	13.45 mA cm^{-2} (partial j)	–1.15 V vs. RHE	8 hours	200
32	CuPd-1.5-alloy (Sub-1nm alloy)	$CH3COO^-$	46.5 ± 2.1%	~25-36 mA cm^{-2}	–0.7 V vs. RHE	~ 20 hours	208
33	CuAu1% (Atomically dispersed alloy)	$CH3COO^-$	39%	217 mA cm^{-2} (partial j)		~ 140 mins at 200 mA cm^{-2}	210

5. Conclusions

In this review, we have presented a comprehensive product-centered classification for CO_2 electroreduction, demonstrating how specific nanoalloy architectures can be tailored to overcome the

intrinsic limitations of monometallic catalysts. Our analysis highlights that catalytic performance is governed by a synergistic interplay between thermodynamic optimization and geometric control. On one hand, electronic and strain effects act as thermodynamic levers, tuning the d-band center of the active metal to optimize the binding strength of key intermediates, thereby enhancing intrinsic turnover frequency and suppressing the competing hydrogen evolution reaction. On the other hand, ensemble and tandem effects serve as geometric levers, where the spatial arrangement of atoms dictates the reaction pathway. Isolated sites spatially restrict C–C coupling to favor C_1 products, whereas contiguous multi-atom ensembles or proximal tandem interfaces facilitate the dimerization of *CO intermediates, effectively steering the pathway toward C_{2+} hydrocarbons and oxygenates.

As CO_2RR research progresses toward practical applications, it is crucial to critically evaluate the inherent strengths and outstanding unresolved issues of current nanoalloy design strategies (summarized in Table 6). While single-atom/dilute alloying and strain engineering are highly effective in breaking LSRs and modulating d-band centers, they intrinsically suffer from thermodynamic metastability. Specifically, the aggregation of single atoms and the relaxation of lattice strain under highly negative cathodic potentials remain significant barriers to industrial lifespans. Conversely, intermetallic phase control offers a robust solution to these stability issues by preventing atomic reconstruction and phase segregation via high mixing enthalpies, albeit being limited to specific thermodynamically favorable metal pairs. Meanwhile, tandem/Janus and nanocavity structuring excellent geometrical levers to enhance local *CO coverage and C–C coupling; however, translating their complex syntheses into scalable mass-production remains a formidable technical challenge. Future catalyst development must aim to bridge these gaps by combining the atomic precision of these strategies with scalable and robust fabrication techniques.

Table 6. Systematic evaluation of nanoalloy design strategies for CO_2RR.

Nanoalloy design strategy	**Advantages**	**Limitations**	**Applicable scenarios**	**Examples**
Single-atom/ dilute alloying	- Maximizes atom utilization. - Effectively breaks inherent LSRs of intermediates. - For example, Pr single-atom on Cu facilitates unique asymmetric CO–CHO coupling[186], and dilute alloys can modulate CO binding without blocking active sites[194].	- Single-atom sites and dilute components are highly susceptible to reconstruction and aggregation under dynamic, highly negative cathodic potentials. - Precise synthesis control at bulk scale remains challenging.	- Tuning specific reaction pathways for target products. - Suppressing the competing HER.	- Pr single-atom on Cu[186] - Single Co atom on Cu[178] - Cu-based dilute alloys[194]

Intermetallic and phase control	- Highly ordered atomic arrangements provide uniform active ensembles, separating geometric effects from electronic ones. - High mixing enthalpy suppresses the phase segregation and catalyst restructuring during reaction, leading to exceptional long-term stability.	- Restricted to specific metal pairs that can thermodynamically form stable intermetallic phases. - Synthesis often requires strict processing windows (e.g., precise temperature or oxygen partial pressure control).	- Continuous, long-term stable electrolysis operations in flow-cells or MEAs where catalyst degradation is a severe issue.	- (111) facet-oriented Cu_2Mg[199] - Ordered Pd_3Bi vs. solid solution[149] - Intermetallic CuAu[156]
Tandem/ Janus structuring	- Couples distinct active sites in close proximity to facilitate intermediate spillover. - This increases local *CO coverage and significantly promotes C–C coupling toward C_{2+} products.	- Synthesis requires complex, multi-step procedures (such as seeded growth strategies). - Precisely controlling the interface boundary and domain size at a mass-production scale is extremely difficult.	- Cascade CO_2 electroreduction aiming for complex multi-carbon.	- Au-Cu Janus nanostructures[189] - Cu-Ag tandem catalysis[93,203]
Strain engineering	- Introduces lattice mismatch to modulate the d-band center of the active metal. - This precisely optimizes the adsorption energy of key intermediates without altering the bulk composition.	- Lattice strain is thermodynamically metastable. - Strain relaxation during long-term electrochemical cycling inevitably leads to irreversible performance degradation and structural collapse.	- Boosting intrinsic activity and fine-tuning the binding strength of specific intermediates.	- Sn-doped strained CuAg film[128] - Strain-engineered AuPd[129] - Tensile-strained Cu-Bi[127]
Nanocavity and hierarchical	- Generates a strong confinement effect that enriches the local concentration of intermediates	- Highly porous or dendritic morphologies are prone to collapse or severe surface	- Designing high-surface-area electrodes for deep reduction to	- Nanocavity enriched CuPd[190]

porous structuring	(increasing *CO coverage), effectively promoting C–C coupling. - Enhances mass transport of reactants/products.	reconstruction under strong cathodic potentials over time. - Synthesis may involve complex dealloying or templating steps.	C_{2+} products in aqueous or flow-cell systems.	- Channel-rich Pd-Cu nanodendrites[173]

6. Future Perspectives

Looking forward, bridging the gap between laboratory-scale discovery and industrial deployment requires a paradigm shift focused on deepening the fundamental understanding of dynamic interfaces. While static models are well-established, the behavior of the alloy-electrolyte interface under reaction conditions remains a critical missing mechanism. Since nanoalloys are particularly prone to potential-driven atomic segregation, elemental leaching, and structural reconstruction under harsh cathodic conditions, future research must decouple the dynamic restructuring of metastable active phases from the bulk structure. To unravel these complex mechanisms during CO_2RR, the extensive deployment of advanced in situ and operando characterization techniques is indispensable. A robust analytical framework for this can be drawn from a recent systematic review of in situ methodologies used to investigate interfacial failure mechanisms in zinc anodes.[216] By analogously applying these in situ/operando spectroscopies and microscopies, researchers can track transient chemical valences, intermediate adsorption, and morphological evolution in real-time. Ultimately, this shift from post-mortem static observations to dynamic mechanistic tracking will be the key to stabilizing active metastable phases and designing "self-healing" alloys.

Beyond advanced experimental characterization, the rational design of complex nanoalloys increasingly relies on theoretical computations. While traditional DFT provides fundamental insights, exploring the vast compositional space of multimetallic nanoalloys requires high-throughput approaches. To transcend these computational limits, ML has emerged as a powerful tool. Fast-forward prediction frameworks, integrating comprehensive material databases, structural descriptors, and deep learning algorithms, have successfully accelerated the discovery of advanced energy materials.[217] Adapting these robust ML methodologies provides critical methodological references for the theoretical design and rapid performance prediction of CO_2RR nanoalloys. Such frameworks can rapidly screen multimetallic combinations, effectively guiding targeted experimental synthesis and significantly reducing empirical iterations.

Furthermore, regarding technological development, the focus must shift from half-cell activity to full-cell system performance to realize practical deployment. Actual industrialization demands the simultaneous achievement of stringent benchmarks: current densities of at least 1 A cm^{-2}, FEs exceeding 80%, operational stability beyond 1000 hours, and high single-pass CO_2 conversion.[218] As research transitions to MEAs and porous solid electrolyte reactors, overcoming mass transport limitations at the triple-phase boundary becomes paramount. Consequently, future nanoalloy designs must incorporate hydrophobicity engineering to prevent electrode wetting and flooding under high-throughput conditions.[218,219] Scaling up from laboratory electrodes (< 5 cm^2) to industrial stacks (> 1 m^2) introduces complex engineering hurdles. Addressing nonuniform fluid distribution and edge

View Article Online
DOI: 10.1039/D6NA00155F

effects requires sophisticated flow field architectures combined with advanced ion-exchange membranes to regulate local pH, suppress hydrogen evolution, and mitigate CO_2 crossover.[220] Finally, enhancing economic feasibility is a critical prerequisite. Adapting CO_2RR systems to operate efficiently with low-concentration CO_2 streams, such as industrial flue gas (~13% CO_2), will drastically reduce operational expenses for high-value C_{2+} production.

As CO_2RR technologies advance toward commercialization, their direct integration with intermittent renewable energy sources, such as photovoltaics and wind power, presents a critical frontier. However, the variable nature of these power supplies introduces multifaceted challenges. Primarily, frequent start-stop cycles severely compromise both catalyst and electrolyzer durability. In zero-gap architectures, discontinuous operation degrades the hydrophobicity of the gas diffusion electrode, triggering flooding that restricts CO_2 mass transport and exacerbates parasitic hydrogen evolution.[221] At the atomic level, these transient potentials induce extreme structural stress; power lapses to open-circuit voltages can trigger rapid catalyst dissolution and restructuring, whereas sudden power surges promote carbonate precipitation that blocks active sites.[222] Bridging this electrical gap necessitates robust power electronics or hybrid energy storage buffers, both of which substantially inflate the capital expenditures of the integrated plant. Finally, the diurnal nature of renewable sources introduces ambient temperature swings that destabilize the local reaction environment. Such temperature variations directly perturb CO_2 solubility, interfacial pH, and activation energies, while also accelerating the physical deformation of ion-exchange membranes. Consequently, deploying thermo-mechanically resilient components and adaptive regulation systems is indispensable to mitigate these environmental swings and ensure practical viability.

View Article Online
DOI: 10.1039/D6NA00155F

DATA AVAILABILITY STATEMENT

No primary research results, software or code have been included and no new data were generated or analysed as part of this review.

REFERENCE

1 United Nations Framework Convention on Climate Change (UNFCCC), *Report of the Conference of the Parties on its twenty-first session, held in Paris from 30 November to 13 December 2015. Addendum. Part two: Action taken by the Conference of the Parties at its twenty-first session*, United Nations, 2016.

2 The Intergovernmental Panel on Climate Change (IPCC), *Global Warming of 1.5°C: IPCC Special Report on Impacts of Global Warming of 1.5°C above Pre-industrial Levels in Context of Strengthening Response to Climate Change, Sustainable Development, and Efforts to Eradicate Poverty*, Cambridge University Press, 1st edn., 2022.

3 Felipe de Carvalho, *UN News*, 2025.

4 United Nations Framework Convention on Climate Change (UNFCCC), *The Baku to Belém Roadmap to 1.3T*, United Nations, 2025.

5 N. Höhne, M. J. Gidden, M. Den Elzen, F. Hans, C. Fyson, A. Geiges, M. L. Jeffery, S. Gonzales-Zuñiga, S. Mooldijk, W. Hare and J. Rogelj, *Nat. Clim. Chang.*, 2021, **11**, 820–822.

6 H. L. Van Soest, M. G. J. Den Elzen and D. P. Van Vuuren, *Nat Commun*, 2021, **12**, 2140.

7 P. Guo, K. Liu, X. Liu, R. Liu and Z. Yin, *Energy Fuels*, 2024, **38**, 5659–5675.

8 M. Aresta, A. Dibenedetto and A. Angelini, *Chem. Rev.*, 2014, **114**, 1709–1742.

9 K. Li, X. An, K. H. Park, M. Khraisheh and J. Tang, *Catalysis Today*, 2014, **224**, 3–12.

10 C. Hepburn, E. Adlen, J. Beddington, E. A. Carter, S. Fuss, N. Mac Dowell, J. C. Minx, P. Smith and C. K. Williams, *Nature*, 2019, **575**, 87–97.

11 M. Hubert, A. M. Esposito, D. Peterson, E. Miller and J. Stanford, in *Energy earth shots*, US Department of Energy, 2024.

12 S. Hughes, S. Henry, M. Turner, A. Zoelle, N. Kuehn, M. Adams, A. J. Eggleston, M. Woods and G. A. Hackett, *Quality Guidelines for Energy System Studies: Performing a Techno-Economic Analysis for Carbon Conversion Technologies*, National Energy Technology Laboratory (NETL), Pittsburgh, PA, Morgantown, WV, and Albany, OR (United States), 2023.

13 W. Zhang, Y. Hu, L. Ma, G. Zhu, Y. Wang, X. Xue, R. Chen, S. Yang and Z. Jin, *Advanced Science*, 2018, **5**, 1700275.

14 S. Zhao, R. Jin and R. Jin, *ACS Energy Lett.*, 2018, **3**, 452–462.

15 M. S. Yesupatham, B. Honnappa, N. Agamendran, S. Y. Kumar, G. Chellasamy, S. Govindaraju, K. Yun, N. C. S. Selvam, A. Maruthapillai, W. Li and K. Sekar, *Advanced Sustainable Systems*, 2024, **8**, 2300549.

16 S. Cao, H. Chen, Y. Hu, J. Li, C. Yang, Z. Chen, S. Wei, S. Liu, Z. Wang, D. Sun and X. Lu, *Chemical Engineering Journal*, 2023, **461**, 141936.

17 L. Liu, F. Wang, X. Chu, L. Zhang, S. Zhang, X. Wang, G. Che, S. Song and H. Zhang, *Advanced Energy Materials*, 2024, **14**, 2301575.

View Article Online
DOI: 10.1039/D6NA00155F

18 Q. Wang, T. Luo, X. Cao, Y. Gong, Y. Liu, Y. Xiao, H. Li, F. Gröbmeyer, Y.-R. Lu, T.-S. Chan, C. Ma, K. Liu, J. Fu, S. Zhang, C. Liu, Z. Lin, L. Chai, E. Cortes and M. Liu, *Nat Commun*, 2025, **16**, 2985.

19 R. Nankya, Y. Xu, A. Elgazzar, P. Zhu, T. Wi, C. Qiu, Y. Feng, F. Che and H. Wang, *Angew Chem Int Ed*, 2024, **63**, e202403671.

20 X. Long, Y. Peng, Z. Yu, Y. Zhang, X. Jiang and H. Yang, *Applied Catalysis A: General*, 2025, **701**, 120330.

21 A. Elgazzar, P. Zhu, F.-Y. Chen, S. Hao, T.-U. Wi, C. Qiu, V. Okatenko and H. Wang, *ACS Energy Lett.*, 2025, **10**, 450–458.

22 J. Li, C. Jing and J. Wang, *Nano Res.*, 2024, **17**, 6922–6930.

23 H. Wu, B. Tian, W. Xu, K. K. Abdalla, Y. Kuang, J. Li and X. Sun, *J. Am. Chem. Soc.*, 2024, **146**, 22266–22275.

24 S.-C. Wang, X. Ji, R. Hou, L. Qi, P. Jing, X. Xu, B. Liu and J. Zhang, *ACS Materials Lett.*, 2024, **6**, 4728–4737.

25 G.-R. Zhu, Z.-L. Wang, H.-C. Hu, X.-H. Guan and H.-B. Zhu, *Journal of Alloys and Compounds*, 2025, **1026**, 180410.

26 Z. Lv, C. Wang, W. Liu, R. Liu, Y. Liu, X. Feng, W. Yang and B. Wang, *Advanced Energy Materials*, 2024, **14**, 2402551.

27 C. Zhan, F. Dattila, C. Rettenmaier, A. Herzog, M. Herran, T. Wagner, F. Scholten, A. Bergmann, N. López and B. Roldan Cuenya, *Nat Energy*, 2024, **9**, 1485–1496.

28 X. Zhao, G. Hao, Q. Fang, X. Lang, D. Li, D. Zhong, J. Li and Q. Zhao, *Applied Surface Science*, 2024, **664**, 160202.

29 J. Zhou, B. He, P. Huang, D. Wang, Z. Zhuang, J. Xu, C. Pan, Y. Dong, D. Wang, Y. Wang, H. Huang, J. Zhang and Y. Zhu, *Angewandte Chemie*, 2025, **137**, e202418459.

30 Q. Li, J. Wu, C. Yang, S. Li, C. Long, Z. Zhuang, Q. Li, Z. Guo, X. Huang, Z. Tang, H. Li, D. Wang and Y. Li, *J. Am. Chem. Soc.*, 2025, **147**, 6688–6697.

31 C. Chen, M. Wang, Y. Zhang, X. Yang, K. Zou, W. Lin, M. He, H. Wu and B. Han, *Green Chem.*, 2025, **27**, 5449–5454.

32 Y. Yan, K. Liu, C. Yang, Y. Chen, X. Lv, C. Hu, L. Zhang and G. Zheng, *Small*, 2024, **20**, 2406345.

33 Y.-J. Zhang, V. Sethuraman, R. Michalsky and A. A. Peterson, *ACS Catal.*, 2014, **4**, 3742–3748.

34 A. Goyal, G. Marcandalli, V. A. Mints and M. T. M. Koper, *J. Am. Chem. Soc.*, 2020, **142**, 4154–4161.

35 S. Back, J. Lim, N.-Y. Kim, Y.-H. Kim and Y. Jung, *Chem. Sci.*, 2017, **8**, 1090–1096.

36 Z. Zhao and G. Lu, *Chem. Sci.*, 2022, **13**, 3880–3887.

37 Y. Wang, L. Cao, N. J. Libretto, X. Li, C. Li, Y. Wan, C. He, J. Lee, J. Gregg, H. Zong, D. Su, J. T. Miller, T. Mueller and C. Wang, *J. Am. Chem. Soc.*, 2019, **141**, 16635–16642.

38 F. Liu, C. Wu and S. Yang, *J. Phys. Chem. C*, 2017, **121**, 22139–22146.

39 L. Liu, H. Akhoundzadeh, M. Li and H. Huang, *Small Methods*, 2023, **7**, 2300482.

40 O. G. Njoku, P. Fronczak, K. Smeltz and I. T. McCrum, *npj Comput Mater*, 2025, **11**, 113.

41 X. Ma, Y. Shen, S. Yao, C. An, W. Zhang, J. Zhu, R. Si, C. Guo and C. An, *J. Mater. Chem. A*, 2020, **8**, 3344–3350.

42 Q. Shao, X. Han, K. Li, W. Guan, Y. Ling and Z. Lv, *Journal of Colloid and Interface Science*, 2025, **693**, 137564.

43 R. Wang and J. Lee, *Small*, 2024, 2401546.

44 X. Wu, Q. Yan, H. Wang, D. Wu, H. Zhou, H. Li, S. Yang, T. Ma and H. Zhang, *Adv Funct Materials*, 2024, **34**, 2404535.

45 Y. Zheng, H. Liu and Y. Zhang, *ChemSusChem*, 2020, **13**, 6090–6123.

46 H. S. Moon, S. A. Jaffer, R. K. Miao, E. H. Sargent and D. Sinton, *Nat Rev Mater*, DOI:10.1038/s41578-025-00875-2.

47 S. Kim, H. I. Lee, S. Kwon, J. Lee, I. Jeon, H.-S. Oh, M. Grätzel, W. A. Goddard and C. Choi, *ACS Nano*, 2026, **20**, 3205–3227.

48 H. B. Yang, S.-F. Hung, S. Liu, K. Yuan, S. Miao, L. Zhang, X. Huang, H.-Y. Wang, W. Cai, R. Chen, J. Gao, X. Yang, W. Chen, Y. Huang, H. M. Chen, C. M. Li, T. Zhang and B. Liu, *Nat Energy*, 2018, **3**, 140–147.

49 A. R. Woldu, Z. Huang, P. Zhao, L. Hu and D. Astruc, *Coordination Chemistry Reviews*, 2022, **454**, 214340.

50 P.-F. Sui, M.-R. Gao, Y.-C. Wang and J.-L. Luo, *Acc. Mater. Res.*, 2024, **5**, 699–711.

51 J. Han, X. Bai, X. Xu, X. Bai, A. Husile, S. Zhang, L. Qi and J. Guan, *Chem. Sci.*, 2024, **15**, 7870–7907.

52 H. Jiang, R. Luo, Y. Li and W. Chen, *EcoMat*, 2022, **4**, e12199.

53 C.-C. Weng, X.-W. Lv, J.-T. Ren, T.-Y. Ma and Z.-Y. Yuan, *Electrochem. Energy Rev.*, 2022, **5**, 19.

54 W. Zhang, A. Yu, H. Mao, G. Feng, C. Li, G. Wang, J. Chang, D. Halat, Z. Li, W. Yu, Y. Shi, S. Liu, D. W. Fox, H. Zhuang, A. Cai, B. Wu, F. Joshua, J. R. Martinez, L. Zhai, M. D. Gu, X. Shan, J. A. Reimer, Y. Cui and Y. Yang, *J. Am. Chem. Soc.*, 2024, **146**, 21335–21347.

55 T. Ahmad, S. Liu, M. Sajid, K. Li, M. Ali, L. Liu and W. Chen, *Nano Research Energy*, 2022, **1**, e9120021.

56 L. Zaza, K. Rossi and R. Buonsanti, *ACS Energy Lett.*, 2022, **7**, 1284–1291.

57 P. A. Kempler and A. C. Nielander, *Nat Commun*, 2023, **14**, 1158.

58 J. Qiao, Y. Liu, F. Hong and J. Zhang, *Chem. Soc. Rev.*, 2014, **43**, 631–675.

59 O. S. Bushuyev, P. De Luna, C. T. Dinh, L. Tao, G. Saur, J. Van De Lagemaat, S. O. Kelley and E. H. Sargent, *Joule*, 2018, **2**, 825–832.

60 Y. Zang, P. Wei, H. Li, D. Gao and G. Wang, *Electrochem. Energy Rev.*, 2022, **5**, 29.

61 Y. Hori, K. Kikuchi and S. Suzuki, *Chemistry Letters*, 1985, **14**, 1695–1698.

62 M. Ma, H. A. Hansen, M. Valenti, Z. Wang, A. Cao, M. Dong and W. A. Smith, *Nano Energy*, 2017, **42**, 51–57.

63 T.-H. Wang, C.-Y. Lin, Y.-C. Huang and C.-Y. Li, *Electrochimica Acta*, 2023, **437**, 141500.

64 Y. Wang, C. Li, Z. Fan, Y. Chen, X. Li, L. Cao, C. Wang, L. Wang, D. Su, H. Zhang, T. Mueller and C. Wang, *Nano Lett.*, 2020, **20**, 8074–8080.

View Article Online
DOI: 10.1039/D6NA00155F

65 S. Liu, H. Tao, L. Zeng, Q. Liu, Z. Xu, Q. Liu and J.-L. Luo, *J. Am. Chem. Soc.*, 2017, **139**, 2160–2163.

66 R. Daiyan, X. Lu, Y. H. Ng and R. Amal, *ChemistrySelect*, 2017, **2**, 879–884.

67 S. Liu, X.-Z. Wang, H. Tao, T. Li, Q. Liu, Z. Xu, X.-Z. Fu and J.-L. Luo, *Nano Energy*, 2018, **45**, 456–462.

68 J. T. Feaster, C. Shi, E. R. Cave, T. Hatsukade, D. N. Abram, K. P. Kuhl, C. Hahn, J. K. Nørskov and T. F. Jaramillo, *ACS Catal.*, 2017, **7**, 4822–4827.

69 C. W. Lee, K. D. Yang, D. Nam, J. H. Jang, N. H. Cho, S. W. Im and K. T. Nam, *Advanced Materials*, 2018, **30**, 1704717.

70 J. Zhang, J. Ding, Y. Liu, C. Su, H. Yang, Y. Huang and B. Liu, *Joule*, 2023, **7**, 1700–1744.

71 Y. Zhang, Y. Xiong, Y. Wang, Q. Wang and J. Fan, *Nanoscale Horiz.*, 2025, 10.1039.D5NH00216H.

72 T. K. Todorova, M. W. Schreiber and M. Fontecave, *ACS Catal.*, 2020, **10**, 1754–1768.

73 L. Li, X. Li, Y. Sun and Y. Xie, *Chem. Soc. Rev.*, 2022, **51**, 1234–1252.

74 A. Rendón-Calle, S. Builes and F. Calle-Vallejo, *Current Opinion in Electrochemistry*, 2018, **9**, 158–165.

75 G. M. Tomboc, S. Choi, T. Kwon, Y. J. Hwang and K. Lee, *Advanced Materials*, 2020, **32**, 1908398.

76 D. Ma, C. Zhi, Y. Zhang, J. Chen, Y. Zhang and J.-W. Shi, *ACS Nano*, 2024, **18**, 21714–21746.

77 L. Li, K. Yuan and Y. Chen, *Acc. Mater. Res.*, 2022, **3**, 584–596.

78 T. N. Nguyen, M. Salehi, Q. V. Le, A. Seifitokaldani and C. T. Dinh, *ACS Catal.*, 2020, **10**, 10068–10095.

79 S. Lu, M. Mazur, K. Guo, D. C. Stoian, M. Gu, W. M. Tucho and Z. Yu, *Small*, 2024, **20**, 2309251.

80 Y. Ouyang, L. Shi, X. Bai, Q. Li and J. Wang, *Chem. Sci.*, 2020, **11**, 1807–1813.

81 J. Greeley, *Annu. Rev. Chem. Biomol. Eng.*, 2016, **7**, 605–635.

82 M. M. Montemore and J. W. Medlin, *Catal. Sci. Technol.*, 2014, **4**, 3748–3761.

83 J. Pérez-Ramírez and N. López, *Nat Catal*, 2019, **2**, 971–976.

84 C. T. Campbell, *Acc. Chem. Res.*, 2019, **52**, 984–993.

85 X. Guan, C. Zhao, X. Liu, S. Liu, W. Gao and Q. Jiang, *J. Phys. Chem. C*, 2020, **124**, 25898–25906.

86 S. V. Parmar, D. Kaur and V. Avasare, *J. Mater. Chem. A*, 2024, **12**, 18774–18814.

87 L. Wang, Z. Liu, R. Li, H. Gao, P. Yang, W. Wang, X. Xue, S. Feng, L. Yu and G. Wang, *J. Mater. Chem. A*, 2023, **11**, 24836–24853.

88 V. R. Manikam, K. Y. Cheong and K. A. Razak, *Materials Science and Engineering: B*, 2011, **176**, 187–203.

89 P. Lu, J. Zhou, Y. Hu, J. Yin, Y. Wang, J. Yu, Y. Ma, Z. Zhu, Z. Zeng and Z. Fan, *J. Mater. Chem. A*, 2021, **9**, 19025–19053.

90 M. Śliwa, H. Zhang, J. Gao, B. O. Stephens, A. J. Patera, D. Raciti, P. D. Hanrahan, Z. A. Warecki, D. L. Foley, K. J. Livi, T. H. Brintlinger, M. L. Taheri, A. S. Hall and T. J. Kempa, *Nano Lett.*, 2024, **24**, 13911–13918.

91 R. Ferrando, J. Jellinek and R. L. Johnston, *Chem. Rev.*, 2008, **108**, 845–910.

92 X. Shan, H. Zhang, Q. Liu, J. Yu, J. Zhu, R. Li and J. Wang, *Applied Surface Science*, 2025, **686**, 162200.

93 M. Van Der Veer, N. Daems, P. Cool and T. Breugelmans, *Green Chem.*, 2025, **27**, 6039–6055.

94 Y. Zhang, F. Chen, X. Yang, Y. Guo, X. Zhang, H. Dong, W. Wang, F. Lu, Z. Lu, H. Liu, H. Liu and Y. Cheng, *Small*, 2025, e06942.

95 A. S. Nugraha, V. Malgras, J. Kim, J. Bo, C. Li, M. Iqbal, Y. Yamauchi and T. Asahi, *Small Methods*, 2018, **2**, 1800283.

96 L. Mattarozzi, S. Cattarin, N. Comisso, A. Gambirasi, P. Guerriero, M. Musiani, L. Vázquez-Gómez and E. Verlato, *Electrochimica Acta*, 2014, **140**, 337–344.

97 L. Mattarozzi, S. Cattarin, N. Comisso, R. Gerbasi, P. Guerriero, M. Musiani and E. Verlato, *Electrochimica Acta*, 2017, **230**, 365–372.

98 A. Kloke, C. Köhler, R. Gerwig, R. Zengerle and S. Kerzenmacher, *Advanced Materials*, 2012, **24**, 2916–2921.

99 S. Thota, S. Chen and J. Zhao, *Chem. Commun.*, 2016, **52**, 5593–5596.

100 L. Castilla-Amorós, P. Schouwink, E. Oveisi, V. Okatenko and R. Buonsanti, *J. Am. Chem. Soc.*, 2022, **144**, 18286–18295.

101 H. Yun, W. Choi, D. Shin, H.-S. Oh and Y. J. Hwang, *ACS Catal.*, 2023, **13**, 9302–9312.

102 J. Mo, D. Lou, J. Li, X. Tao, Z. Zheng and W. Liu, *Journal of Colloid and Interface Science*, 2025, **697**, 137934.

103 C. Chen, D. Wu, Z. Li, R. Zhang, C. Kuai, X. Zhao, C. Dong, S. Qiao, H. Liu and X. Du, *Advanced Energy Materials*, 2019, **9**, 1803913.

104 Z. Lin, J. Yue, L. Liang, B. Tang, B. Liu, L. Ren, Y. Li and L. Jiang, *Applied Surface Science*, 2020, **504**, 144461.

105 V. Amendola, S. Scaramuzza, F. Carraro and E. Cattaruzza, *Journal of Colloid and Interface Science*, 2017, **489**, 18–27.

106 Y. Yao, Z. Huang, P. Xie, S. D. Lacey, R. J. Jacob, H. Xie, F. Chen, A. Nie, T. Pu, M. Rehwoldt, D. Yu, M. R. Zachariah, C. Wang, R. Shahbazian-Yassar, J. Li and L. Hu, *Science*, 2018, **359**, 1489–1494.

107 M. Geng, Y. Zhu, J. Guan, R. Zhang, Q. Zou, L. Wang, B. Guo and M. Zhang, *Journal of Alloys and Compounds*, 2024, **1005**, 176180.

108 H. Lee, J.-S. Lee, G.-W. Kwak, J. Kim, K.-M. Kim, D. G. Kang, G.-N. Yun, H.-T. Kim, S.-J. Choi and S.-J. Kim, *ACS Nano*, 2025, **19**, 18095–18107.

109 S. Zhang, Y. Jiang, J. Zhao and Y. Du, *Chem. Soc. Rev.*, 2026, **55**, 1494–1513.

110 F.-M. Li, X.-Q. Gao, S.-N. Li, Y. Chen and J.-M. Lee, *NPG Asia Mater*, 2015, **7**, e219–e219.

111 D. G. Shchukin, D. Radziuk and H. Möhwald, *Annu. Rev. Mater. Res.*, 2010, **40**, 345–362.

112 X. Xu and J. Guan, *Adv Funct Materials*, 2025, 2505823.

113 C. Yang, Y. Gao, T. Ma, M. Bai, C. He, X. Ren, X. Luo, C. Wu, S. Li and C. Cheng, *Advanced Materials*, 2023, **35**, 2301836.

114 B. Hammer and J. K. Norskov, *Nature*, 1995, **376**, 238–240.

115 D. Wei, Y. Wang, C. Dong, Z. Zhang, X. Wang, Y. Huang, Y. Shi, X. Zhao, J. Wang, R. Long, Y. Xiong, F. Dong, M. Li and S. Shen, *Angewandte Chemie*, 2023, **135**, e202217369.

116 K. Liu, M. Ma, L. Wu, M. Valenti, D. Cardenas-Morcoso, J. P. Hofmann, J. Bisquert, S. Gimenez and W. A. Smith, *ACS Appl. Mater. Interfaces*, 2019, **11**, 16546–16555.

117 J. Wang, F. Zhu, B. Chen, S. Deng, B. Hu, H. Liu, M. Wu, J. Hao, L. Li and W. Shi, *Chinese Journal of Catalysis*, 2023, **49**, 132–140.

118 X. Sun, R. B. Araujo, E. C. Dos Santos, Y. Sang, H. Liu and X. Yu, *Chem. Soc. Rev.*, 2024, **53**, 7392–7425.

119 C. Yang, B. H. Ko, S. Hwang, Z. Liu, Y. Yao, W. Luc, M. Cui, A. S. Malkani, T. Li, X. Wang, J. Dai, B. Xu, G. Wang, D. Su, F. Jiao and L. Hu, *Sci. Adv.*, 2020, **6**, eaaz6844.

120 W. Zhang, J. Zeng, H. Liu, Z. Shi, Y. Tang and Q. Gao, *Journal of Catalysis*, 2019, **372**, 277–286.

121 J. Zeng, W. Zhang, Y. Yang, D. Li, X. Yu and Q. Gao, *ACS Appl. Mater. Interfaces*, 2019, **11**, 33074–33081.

122 X. Wang, N. Fu, J.-C. Liu, K. Yu, Z. Li, Z. Xu, X. Liang, P. Zhu, C. Ye, A. Zhou, A. Li, L. Zheng, L.-M. Liu, C. Chen, D. Wang, Q. Peng and Y. Li, *J. Am. Chem. Soc.*, 2022, **144**, 23223–23229.

123 S. Zhang, W. Ruan and J. Guan, *Advanced Energy Materials*, 2025, **15**, 2404057.

124 Z. Sun, C. Li, J. Lin, T. Guo, S. Song, Y. Hu, Z. Zhang, W. Yan, Y. Wang, Z. Wei, F. Zhang, K. Zheng, D. Wang, Z. Li, S. Wang and W. Chen, *ACS Nano*, 2024, **18**, 13286–13297.

125 N. Guo, H. Xue, A. Bao, Z. Wang, J. Sun, T. Song, X. Ge, W. Zhang, K. Huang, F. He and Q. Wang, *Angewandte Chemie*, 2020, **132**, 13882–13888.

126 M. Luo and S. Guo, *Nat Rev Mater*, 2017, **2**, 17059.

127 Y. Wei, X. Xu, D. Shi, Y. Jiang, C. Zheng, L. Tan, Z. Liu, S. Zhong and Y. Yu, *Small*, 2024, **20**, 2401017.

128 X. Du, Y. Qin, B. Gao, J. H. Jang, C. Xiao, Y. Li, S. Ding, Z. Song, Y. Su and K. T. Nam, *J. Mater. Chem. A*, 2022, **10**, 7082–7089.

129 S. Ji, Q. Wang, J. Huang, R. Guo, Y. Li, Y. Zheng, R. Li, Y. Zhao, C. Wu and M. Jin, *Chemical Engineering Journal*, 2025, **520**, 166114.

130 J. Hao, Z. Zhuang, J. Hao, K. Cao, Y. Hu, W. Wu, S. Lu, C. Wang, N. Zhang, D. Wang, M. Du and H. Zhu, *ACS Nano*, 2022, **16**, 3251–3263.

131 M. Mavrikakis, B. Hammer and J. K. Nørskov, *Phys. Rev. Lett.*, 1998, **81**, 2819–2822.

132 X. Chen, R. Lu, C. Li, W. Luo, R. Yu, J. Zhu, L. Lv, Y. Dai, S. Gong, Y. Zhou, W. Xiong, J. Wu, H. Cai, X. Wu, Z. Deng, B. Xing, L. Su, F. Wang, F. Chao, W. Chen, C. Xia, Z. Wang and L. Mai, *Nat Commun*, 2025, **16**, 1927.

133 L. Guo, J. Zhou, F. Liu, X. Meng, Y. Ma, F. Hao, Y. Xiong and Z. Fan, *ACS Nano*, 2024, **18**, 9823–9851.

134 X.-D. Liang, N. Tian, S.-N. Hu, Z.-Y. Zhou and S.-G. Sun, *Materials Reports: Energy*, 2023, **3**, 100191.

135 Y. Xing, X. Kong, X. Guo, Y. Liu, Q. Li, Y. Zhang, Y. Sheng, X. Yang, Z. Geng and J. Zeng, *Advanced Science*, 2020, **7**, 1902989.

136 J. Feng, L. Wu, S. Liu, L. Xu, X. Song, L. Zhang, Q. Zhu, X. Kang, X. Sun and B. Han, *J. Am. Chem. Soc.*, 2023, **145**, 9857–9866.

137 P. Liu and J. K. Nørskov, *Phys. Chem. Chem. Phys.*, 2001, **3**, 3814–3818.

138 F. Maroun, F. Ozanam, O. M. Magnussen and R. J. Behm, *Science*, 2001, **293**, 1811–1814.

139 L. Bian, Y. Bai, J.-Y. Chen, H.-K. Guo, S. Liu, H. Tian, N. Tian and Z.-L. Wang, *ACS Nano*, 2025, **19**, 9304–9316.

140 Y. Yan, H. Zhou, T. Li, D. Wang, P. Schaaf, G. Guo and X. Wang, *Small*, 2025, 2501125.

141 Q. Zeng, S. Tian, H. Liu, L. Xu, P. Cui, D. Chen, J. Wang and J. Yang, *Adv Funct Materials*, 2023, **33**, 2307444.

142 C. Chen, Y. Li, S. Yu, S. Louisia, J. Jin, M. Li, M. B. Ross and P. Yang, *Joule*, 2020, **4**, 1688–1699.

143 D. Meng, M. Zhang, D. Si, M. Mao, Y. Hou, Y. Huang and R. Cao, *Angew Chem Int Ed*, 2021, **60**, 25485–25492.

144 X. Kang, Z. He, F. Wang, Y. Liu and L. Guo, *Adv Funct Materials*, 2025, **35**, 2419802.

145 W. Xu, H. Shang, J. Guan, X. Yang, X. Jin, L. Tao and Z. Shao, *Adv Funct Materials*, 2025, **35**, 2412812.

146 Q. Qin, H. Suo, L. Chen, Y. Wang, J. Wang, H. Liu, S. Dou, M. Lao and W. Lai, *Adv Materials Inter*, 2024, **11**, 2301049.

147 B. Chen, L. Gong, N. Li, H. Pan, Y. Liu, K. Wang and J. Jiang, *Adv Funct Materials*, 2024, **34**, 2310029.

148 R. Yang, L. Xia, W. Jiang, Y. Cheng, K. Wang, T. Chen, F. Li, X. Zhao, B. Wang, Y. Zhou, F. P. G. De Arquer and M. Huang, *Advanced Energy Materials*, 2025, **15**, 2405964.

149 T. Gong, G. Qiu, M.-R. He, O. V. Safonova, W.-C. Yang, D. Raciti, C. Oses and A. S. Hall, *J. Am. Chem. Soc.*, 2025, **147**, 510–518.

150 P. An, L. Wei, H. Li, B. Yang, K. Liu, J. Fu, H. Li, H. Liu, J. Hu, Y.-R. Lu, H. Pan, T.-S. Chan, N. Zhang and M. Liu, *J. Mater. Chem. A*, 2020, **8**, 15936–15941.

151 B. Sheng, D. Cao, Z. Qi, H. Shou, Y. Xia, X. Su, S. Chen, C. Wu, H. Liu, P. J. Chimtali, Y. Chu, C. Liu, X. Wu and L. Song, *Materials Today*, 2025, **83**, 54–63.

152 T. Liu, H. Luo, T. Ouyang and Z. Liu, *Adv Funct Materials*, 2025, **35**, 2415367.

153 Z. Zhang, L. Wang, X. Yang, M. Chu, L. Huang, J. Fan, W. Xie, D. Liu, W. Yuan and Y. Situ, *ACS Sustainable Chem. Eng.*, 2024, **12**, 18566–18576.

154 W. Lai, Y. Qiao, Y. Wang and H. Huang, *Advanced Materials*, 2023, **35**, 2306288.

155 H. Wu, H. Yu, Y. Chow, P. A. Webley and J. Zhang, *Advanced Materials*, 2024, **36**, 2403217.

156 S. Kuang, M. Li, X. Chen, H. Chi, J. Lin, Z. Hu, S. Hu, S. Zhang and X. Ma, *Chinese Chemical Letters*, 2023, **34**, 108013.

157 Y. Jia, Y. Ma, W.-E. Yang, Y. Zhu, X. Zhang, S. Xie, T.-W. Kuo, S. Dai and K.-W. Wang, *Chemical Engineering Journal*, 2024, **488**, 150946.

158 G. Mei, Z. Sun, Z. Fang, Y. Dan, X. Lu, J. Tang, W. Guo, Y. Zhai and Z. Zhu, *Small*, 2025, **21**, 2504086.

159 S. Liang, L. Huang, Y. Gao, Q. Wang and B. Liu, *Advanced Science*, 2021, **8**, 2102886.

160 S. Nitopi, E. Bertheussen, S. B. Scott, X. Liu, A. K. Engstfeld, S. Horch, B. Seger, I. E. L. Stephens, K. Chan, C. Hahn, J. K. Nørskov, T. F. Jaramillo and I. Chorkendorff, *Chem. Rev.*, 2019, **119**, 7610–7672.

161 H. Huang, K. Yue, K. Lei, B. Y. Xia and Y. Yan, *J. Phys. Chem. C*, 2024, **128**, 12067–12074.

162 Y. Wang, R. Xie, N. Ci, Z. Zhu, C. Li, G. Chai, H.-J. Qiu and Y. Zhang, *Journal of Energy Chemistry*, 2024, **99**, 450–457.

163 Y. Song, Y. Hua, X. Liu and Z. Gao, *Journal of Alloys and Compounds*, 2025, **1022**, 179927.

164 Y. Guo, Y. Luo, H. Wang, X. Chen, X. Liu, B. Guo, J. Sun, R. Wang, W. Li and C. Zhao, *Fuel*, 2025, **392**, 134821.

165 R. Zou, R. Luo, F. Liu, Y. Wang, M. S. Riaz, S. Shen, G. Yang, Z. Tang, H. Huang, G. Li and Q. Bi, *Small*, 2025, **21**, 2501030.

166 X. Linghu, J. Chen, L. Jiang and T. Wang, *Nano Materials Science*, 2024, S258996512400179X.

167 Y. Kuang, H. Rabiee, L. Ge, T. E. Rufford, Z. Yuan, J. Bell and H. Wang, *Energy & Environ Materials*, 2023, **6**, e12596.

168 W. Wu, J. Zhu, Y. Tong, S. Xiang and P. Chen, *Nano Res.*, 2024, **17**, 3684–3692.

169 T. Fan, J. Zhang, X. Zhang, M. Wang, X. Yi, Y. Lum and Z. Chen, *Nano Energy*, 2024, **130**, 110135.

170 B. Li, J. Chen, L. Wang, D. Xia, S. Mao, L. Xi, S. Ying, H. Zhang and Y. Wang, *Applied Catalysis B: Environment and Energy*, 2025, **363**, 124784.

171 Z. Zhang, M. Li, S. Yang, Q. Ma, J. Dang, R. Feng, Z. Bai, D. Liu, M. Feng and Z. Chen, *Advanced Materials*, 2024, 2407266.

172 H. Huang, X. Ding, X. Mao, Y. Yan, F. Lv, B. Pan, W. Huang, L. Wang, N. Han and Y. Li, *Adv Funct Materials*, 2024, **34**, 2408966.

173 X. Huang, X. Yu, H. Liu, S. Xia, Y. Jia, Z. Chen, J. Xu and Y. Xia, *Adv Funct Materials*, 2025, e13814.

174 C. Fang, L. Huang, W. Gao, X. Jiang, H. Liu, R. Hu, X. Li, J. Yu and W. Zhou, *Advanced Energy Materials*, 2024, **14**, 2400813.

175 A. Huang, T. Zhou, J. Zhang, Y. Zhang, Y. Wu, Y. Wang and W. Luo, *ChemCatChem*, 2024, **16**, e202400504.

176 S. Go, W. Kwon, D. Hong, T. Lee, S.-H. Oh, D. Bae, J.-H. Kim, S. Lim, Y.-C. Joo and D.-H. Nam, *Nanoscale Horiz.*, 2024, **9**, 2295–2305.

177 J. Huang, Y. Yang, X. Liang, B. Chen, Y. Shen, Y. Chen, J. Yang, Y. Yu, F. Huang, H. He, P. Chen, L. Zhou and A. Guan, *Advanced Science*, 2025, **12**, 2417247.

178 J. Li, M. Wei, B. Ji, S. Hu, J. Xue, D. Zhao, H. Wang, C. Liu, Y. Ye, J. Xu, J. Zeng, R. Ye, Y. Zheng, T. Zheng and C. Xia, *Angewandte Chemie*, 2025, **137**, e202417008.

179 H. Sun, Y. Wen, Y. Li, R. Fan, Y. Lu, C. Feng, H. Liu, Y. Wang, Z. Ma, Y. Zhang, R. Amal and Z. Yan, *Applied Catalysis B: Environment and Energy*, 2026, **381**, 125891.

180 A. Husile, Z. Wang and J. Guan, *Chem. Sci.*, 2025, **16**, 5413–5446.

181 X. Zhang, S.-X. Guo, K. A. Gandionco, A. M. Bond and J. Zhang, *Materials Today Advances*, 2020, **7**, 100074.

182 L. Lu, X. Sun, J. Ma, D. Yang, H. Wu, B. Zhang, J. Zhang and B. Han, *Angewandte Chemie*, 2018, **130**, 14345–14349.

183 S. Payra, S. Shenoy, C. Chakraborty, K. Tarafder and S. Roy, *ACS Appl. Mater. Interfaces*, 2020, **12**, 19402–19414.

184 G. Bhattacharya, R. Manna, P. Sardar, S. Rahut, S. Kumar and A. N. Samanta, *Journal of Environmental Chemical Engineering*, 2025, **13**, 117451.

185 S. Desmons, J. Bonin, M. Robert and S. Bontemps, *Chem. Sci.*, 2024, **15**, 15023–15086.

186 Y. Xiao, F. Yu, C. Xia, D. Zhu, J. Chen, N. Liu, Y. Zhao, R. Qi, W. Guo, B. You, T. Yao, Y. Pang, Z. Wang, H. Wang, F. Song and B. Y. Xia, *J. Am. Chem. Soc.*, 2025, **147**, 15654–15665.

187 S. Zhang, B. Zhang, S. Yang, T. Shao, X. Li, R. Cao and M. Cao, *ACS Appl. Nano Mater.*, 2025, **8**, 1893–1902.

188 H. Wang, F. Zhang, Y. Li, Y. Pang, X. Zhao, Z. Song, W. Wang, J. Sun and Y. Mao, *Journal of Colloid and Interface Science*, 2025, **678**, 506–514.

189 Y. Zheng, J. Zhang, Z. Ma, G. Zhang, H. Zhang, X. Fu, Y. Ma, F. Liu, M. Liu and H. Huang, *Small*, 2022, **18**, 2201695.

190 Z.-Y. Zhang, H.-B. Wang, F.-F. Zhang, J.-W. Li, X.-Z. Hu, S.-W. Yan, Y.-M. Bai, X. Zhang, G.-R. Shen, P.-F. Yin, J. Yang, C.-K. Dong, J. Mao, H. Liu and X.-W. Du, *Rare Met.*, 2024, **43**, 1513–1523.

191 J. Wang, W. Li, J. Peng, S. Shang, X. Fu, G. He and Q. Zhang, *Vacuum*, 2024, **222**, 113017.

192 N. Wang, J. Li, S. Gan, X. Chen, G. Wang, Q. Chen, T. Zhou and B. Li, *Langmuir*, 2025, **41**, 19821–19833.

193 Y. Xiao, Y. Yang, W. Liu and J. Liu, *J. Mater. Chem. A*, 2025, **13**, 26812–26822.

194 B. S. Crandall, Z. Qi, A. C. Foucher, S. E. Weitzner, S. A. Akhade, X. Liu, A. R. Kashi, A. K. Buckley, S. Ma, E. A. Stach, J. B. Varley, F. Jiao and J. Biener, *Small*, 2024, **20**, 2401656.

195 J. Du, J. Liu, Z. Liu, N. Tian, Y. Zhang and X. Gu, *Chem. Commun.*, 2025, 10.1039.D5CC03737A.

196 S. Wang, F. Li, J. Zhao, Y. Zeng, Y. Li, Z.-Y. Lin, T.-J. Lee, S. Liu, X. Ren, W. Wang, Y. Chen, S.-F. Hung, Y.-R. Lu, Y. Cui, X. Yang, X. Li, Y. Huang and B. Liu, *Nat Commun*, 2024, **15**, 10247.

197 Z. Wang, Y. Li, Z. Ma, D. Wang and X. Ren, *iScience*, 2024, **27**, 110437.

198 J.-Y. Kim, H. S. Ahn, I. Kim, D. Hong, T. Lee, J. Jo, H. Kim, M. K. Kwak, H. G. Kim, G. Kang, S. Go, W. H. Ryu, G.-D. Lee, M. Kim, D.-H. Nam, E. S. Park and Y.-C. Joo, *Nat. Synth*, 2023, **3**, 452–465.

199 C. Peng, J. Ma, G. Luo, S. Yan, J. Zhang, Y. Chen, N. Chen, Z. Wang, W. Wei, T. Sham, Y. Zheng, M. Kuang and G. Zheng, *Angew Chem Int Ed*, 2024, **63**, e202316907.

200 T. Guo, C. Ma, X. Wang, Z. Men, B. Liu and A. H. Bedane, *Energy Fuels*, 2025, **39**, 9532–9545.

201 M. Wang, M. Fang, Y. Liu, C. Chen, Y. Zhang, S. Jia, H. Wu, M. He and B. Han, *J. Am. Chem. Soc.*, 2025, **147**, 16450–16458.

202 D. Luo, W. Dai, K. Wu, S. Liu, C. Tang, Y. Sun, F. Dong and C. Long, *Nanoscale*, 2025, **17**, 9057–9071.

203 F. A. Rollier, V. Muravev, N. Kosinov, T. Wissink, D. Anastasiadou, B. Ligt, L. Barthe, M. Costa Figueiredo and E. J. M. Hensen, *J. Mater. Chem. A*, 2025, **13**, 2285–2300.

204 E. Ruiz-López, J. Gandara-Loe, F. Baena-Moreno, T. R. Reina and J. A. Odriozola, *Renewable and Sustainable Energy Reviews*, 2022, **161**, 112329.

205 A. J. Garza, A. T. Bell and M. Head-Gordon, *ACS Catal.*, 2018, **8**, 1490–1499.

206 A. Shekhawat, M. A. A. Mahbub and W. Schuhmann, *ChemElectroChem*, 2026, **13**, e202500413.

207 X. Hu, J. Li, Z. Zhou and L. Wen, *ACS Materials Lett.*, 2023, **5**, 85–94.

208 S. Nie, L. Wu, Q. Liu and X. Wang, *J. Am. Chem. Soc.*, 2024, **146**, 29364–29372.

209 K. Zhang, S. Chen, Y. Ge, X. Zhang, Z. Zhang, C. Ye, G. Pan and L. Hu, *ACS Appl. Nano Mater.*, 2025, **8**, 22285–22294.

210 Q. Sun, Y. Zhao, X. Tan, C. Jia, Z. Su, Q. Meyer, M. I. Ahmed and C. Zhao, *ACS Catal.*, 2023, **13**, 5689–5696.

211 X. Zhong, H.-J. Peng, C. Xia and X. Liu, *J. Mater. Chem. A*, 2024, **12**, 19663–19684.

212 M. Zheng, C. Lv and X. Zhou, *Chemistry A European J*, 2025, **31**, e202404354.

213 S. Bae, S. Y. Hwang, G. Yun, Y. Gwon, S. Y. Kim, C. K. Rhee and Y. Sohn, *Energy Fuels*, 2024, **38**, 15497–15514.

214 S. Matsuda, R. Ishibashi and M. Umeda, *ACS Omega*, 2025, **10**, 9630–9638.

215 M. G. Lee, S. Kandambeth, X.-Y. Li, O. Shekhah, A. Ozden, J. Wicks, P. Ou, S. Wang, R. Dorakhan, S. Park, P. M. Bhatt, V. S. Kale, D. Sinton, M. Eddaoudi and E. H. Sargent, *J. Am. Chem. Soc.*, 2024, **146**, 14267–14277.

216 D. Zhang, H. Lu, C. Duan, X. Yuan, Z. Zhu, Y. Qin, Y. Song and Y. Jin, *Energy Mater Adv*, 2025, **6**, 0141.

217 X. Liu, K. Yang, L. Zhang, W. Wang, S. Zhou, B. Wu, M. Xiong, S. Yang and R. Tan, *Energy Mater Adv*, 2024, **5**, 0131.

218 H. Zheng, K. Shi, H. Dong, Y. Yang, P. Yin, B. Shen and J. Wang, *Energy Fuels*, 2025, **39**, 9316–9344.

219 J. Peng, L. Sun, Y. Li, Q. Zhang, X. Ren, X. Li, J. Zhang, X. Sun, Z. Song and L. Zhang, *Electrochem. Energy Rev.*, 2025, **8**, 16.

220 L. Xue, Y. Qi, Z. Li, H. Yang, R. Liu and B. Zhang, *Journal of Energy Chemistry*, 2025, **110**, 88–108.

221 J. Chen, D. Du, Q. Huang and J. Luo, *ACS Energy Lett.*, 2025, **10**, 4027–4034.

222 E. R. Cofell, Z. Park, U. O. Nwabara, L. C. Harris, S. S. Bhargava, A. A. Gewirth and P. J. A. Kenis, *ACS Appl. Energy Mater.*, 2022, **5**, 12013–12021.

View Article Online
DOI: 10.1039/D6NA00155F

DATA AVAILABILITY STATEMENT

No primary research results, software or code have been included and no new data were generated or analysed as part of this review.